IDŐJÁRÁS

QUARTERLY JOURNAL
OF THE HUNGARIAN METEOROLOGICAL SERVICE

CONTENTS

VOL. 124 ∗ NO. 1 ∗ JANUARY – MARCH 2020

IDŐJÁRÁS

Quarterly Journal of the Hungarian Meteorological Service

Editorial Office: Kitaibel P.u. 1, H-1024 Budapest, Hungary
P.O. Box 38, H-1525 Budapest, Hungary
E-mail: journal.idojaras@met.hu
Fax: (36-1) 346-4669

Indexed and abstracted in Science Citation Index Expanded™ and Journal Citation Reports/Science Edition
Covered in the abstract and citation database SCOPUS®
Included in EBSCO's databases

Subscription by mail:
IDŐJÁRÁS, P.O. Box 38, H-1525 Budapest, Hungary
E-mail: journal.idojaras@met.hu

DOI:10.28974/idojaras.2020.1.1

IDŐJÁRÁS

Quarterly Journal of the Hungarian Meteorological Service
Vol. 124, No. 1, January – March, 2020, pp. 1–23

Impact of the stratosphere on the sea surface temperature and ENSO based on HadGEM control runs comparing high top and low top model configurations

Shaomin Cai[1,2], **Weijia Zhang***[,1,3], and **Yizhou Zhao**[4]

[1] *Department of Math&Physics, Shaoxing University*
No.508, Huancheng West Road, Shaoxing 312000, China

[2]*Department of AOP Physics, University of Oxford*
Wellington Square, Oxford OX1 2JD, United Kingdom

[3] *Visiting Scholar, Department of AOP Physics, University of Oxford*
Wellington Square, Oxford OX1 2JD, United Kingdom

[4] *Department of Astronautics, Nanjing University of Aeronautics and Astronautics*
No. 169, Sheng Tai West Road, Nanjing 211106, China

Corresponding Author e-mail: zhangw@physics.ox.ac.uk

(Manuscript received in final form April 16, 2019)

Abstract— Numerous studies on the effects of the El Niño-Southern Oscillation (ENSO) on the stratosphere have been conducted in recent years. However, few of these have examined whether the use of an adequate representation of the stratosphere might affect simulations of the ENSO. In the present work, sea surface temperature data from two numerical model configurations, namely one with a well-resolved stratosphere, the "high top configuration" (Hadley Centre Global Environmental Model, HadGEM2-CCS), and the other without a well-resolved stratosphere, the "low top configuration" (HadGEM2-CC), are employed to study the impact of the stratosphere on the surface climate, especially on the ENSO. A pre-industrial control run is performed to eliminate interference from other factors, such as greenhouse gas warming and volcanic eruptions. Based on the present research, both model configurations function reasonably well and have shown little difference from each other when analyzng the global annual and seasonal mean sea surface temperatures, except for the Northern Atlantic Ocean region. A statistical analysis performed using the t-test method shows that the significant differences in the annual and seasonal mean sea surface temperatures in the Northern Atlantic region result from real signals rather than random noises. Furthermore, the configuration with a better representation of the stratosphere simulates the quasi-period of the ENSO and the seasonal phase-locking characteristics of El Niño more precisely. Therefore, it is probably advantageous to adopt climate models that resolved stratosphere for a more realistic representation of ENSO climatology and its possible variations under certain conditions.

Key-words: stratosphere, sea surface temperature, ENSO, HadGEM, high top configuration, low top configuration

1. Introduction

The present work aims to determine the effects of the stratosphere on global climate as well as on the El Niño-Southern Oscillation (ENSO) by examining and comparing numerical simulations both with and without a well-resolved stratosphere.

1.1. The ENSO phenomenon

The ENSO is a quasi-periodic climate phenomenon that occurs in the tropical Pacific and is attributed to a coupled ocean-atmosphere interaction.

The atmospheric aspect, called the Southern Oscillation, was first identified by *Walker* (1923, 1924) as a seesaw of surface pressure between the central tropical Pacific and the Indonesian Archipelago. The three-dimensional circulation pattern explaining Southern Oscillation was described by *Bjerknes* (1969) and designated as the 'Walker Circulation' (*Fig. 1*). The quasi-periodic warming of the waters off the coast of Peru and Ecuador is called El Niño. El Niño has long been understood to be part of an oceanic oscillation that extends westward along the equator. *Bjerknes* (1966, 1969) was among the first to recognize its connection to the Southern Oscillation.

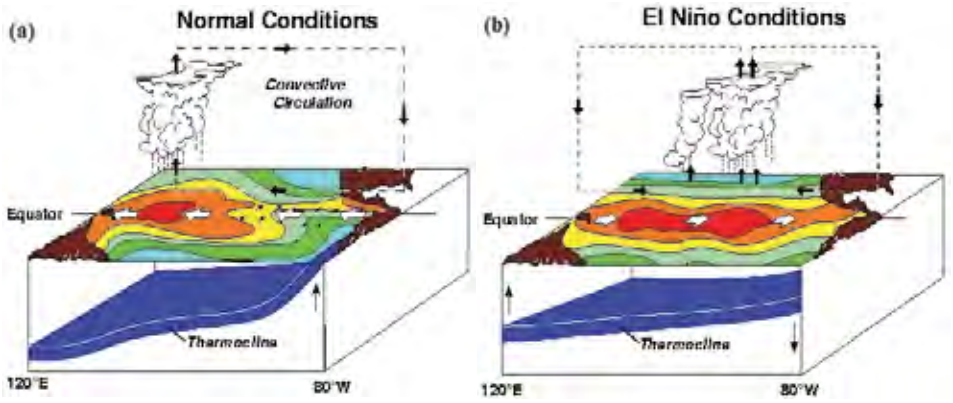

Fig. 1. Schematic diagrams of (a) normal conditions and (b) El Niño conditions in the Pacific Ocean. From www.pmel.noaa.gov/tao/elnino/ninonormal.html

During normal years, as shown in *Fig. 1(a)*, a particularly strong cooling in the eastern Pacific is called La Niña. Under El Niño conditions, as shown in *Fig. 1(b)*, the Walker circulation reverses, resulting in El Niño events. El Niño events are not always followed by La Niña, and vice versa, as they sometimes are

followed by neutral conditions. However, El Niño events have a typical life cycle that tends to be phase-locked with the seasonal cycle, with warm SST anomalies tending to appear in January, strengthening during the year, and eventually peaking in the northern winter one year after their onset (*Wang*, 1995). This seasonal phase locking is also observed in the climate model results examined here (see Section 3.2). Although ENSO events are irregular, in the historical record, the length of this interval has varied from 2 to 7 years (NOAA Climate Prediction Centre (2005-12-19)).

The ENSO is widely accepted to be the largest source of internal variability in the global climate system (*Trenberth et al.*, 1998). The eastward displacement of the atmospheric heat source overlying the warmest water results in significant changes in the global atmospheric circulation, which forces weather changes in regions remote from the tropical Pacific. These remote influences are known as teleconnections.

1.2. ENSO and the stratosphere

El Niño events are associated with maximum warm anomalies occurring in the tropical Pacific. Thus, it is useful to study these events by simulating aspects of surface climate. Observational and modeling studies over the past two decades have fundamentally changed our understanding of the role of the stratosphere in surface weather and climate. Interactions between the stratosphere and other components of the earth's system, from the troposphere to the deep ocean and possibly even the ice sheets of Greenland and Antarctica, reveal coupling across a wide range of spatial and temporal scales. In response to these discoveries, operational forecasts, seasonal predictions, and coupled climate models are raising their lids by adding model layers, incorporating additional stratospheric processes and assimilating data higher into the stratosphere than ever before (*Gerber et al*., 2012).

Van Loon and *Labitzke* (1987) studied the statistical relationship between ENSO and the Arctic stratosphere. They found that strong El Niño events are associated with a strong Aleutian High and weak polar vortex in the stratosphere. Furthermore, the stratosphere appears to play an important role in transmitting the tropical ENSO signals to the mid-latitudes (e.g., *Bell et al.*, 2009). Extra tropical upward wave propagation intensified during warm ENSO events in the boreal winter, modulating the meridional overturning circulation of the stratosphere and the stratospheric polar vortex (*Garcia-Herrera et al.*, 2006). The vortex anomalies, ultimately, then propagated downward, affecting the mid-latitudes in the troposphere (*Cagnazzo* and *Manzini*, 2009).

Several modeling studies have shown that including a well-resolved stratosphere could produce more reliable tropospheric climate change projections. For example, *Hardiman et al*. (2012) suggested that simulations should be performed using stratosphere-resolving general circulation models to capture the

influence of teleconnections and stratospheric processes on surface climate. This finding also indicates that little distinction is found between the model simulations with and without a well-resolved stratosphere, unless the effects of teleconnections on the surface fields during specific years are considered (e.g., the ENSO on the northern extra tropical mean sea level pressure (MSLP)). However, most of the studies included the influences of various possible factors interfering with the interconnectedness of the ENSO and the stratosphere, such as seasonality and nonlinearity (*Van Loon* and *Labitzke*, 1987; *Manzini et al.*, 2006), volcanic eruptions (*Labitzke* and *Van Loon*, 1989) and ozone depletion (*Kiehl* and *Boville*, 1988). However, these observational analyses may benefit from further comparisons with control run simulations. Control run simulations allow for the systematic study of the possible influences by excluding external factors, and they only differ in the stratosphere representations.

Therefore, to study the dynamical impact of the stratosphere alone on the surface climate, and the ENSO in particular, the present work used numerical simulations from model configurations with and without a well-resolved stratosphere. These model configurations are the two configurations of the Hadley Centre Global Environmental Model (HadGEM) run at the Met Office Unified Model for CMIP5. (Refer to Section 2 for more details.) Pre-industrial control runs were used to investigate the effects of the vertical height and resolution of the stratosphere alone on surface climate, and again, the ENSO in particular. (Details of the control run are described in the Section 2.)

In the present work, the first aspect under review is the annual and seasonal mean SSTs in both model configurations, which are compared with observations. The effects of random variability on the annual mean SSTs are also examined. The second aspect under review focuses on the equatorial tropical region in both model configurations to investigate the quasi-period of ENSO events through a power spectrum. The third aspect is the study of the evolution of the ENSO in both model configurations through Hovmoller diagrams. (Details are shown in Section 3.4.) A detailed analysis of the possible factors that may give rise to the differences in the ENSO characteristics between the configurations, as described in Section 3, will be the subject of a later and more extensive study, but these are discussed in general terms at the end of this report.

2. Models and methods

Two configurations of the HadGEM run at the Met Office Unified Model for CMIP5 are used in the present work. These two configurations are the HadGEM2-CCS (high top configuration) and HadGEM2-CC (low top configuration) (*Martin et al*., 2011), which differ only in their vertical extent and vertical resolution. The high top configuration includes a well-resolved stratosphere, incorporating 60 vertical levels (L60) and an upper boundary at 85 km (mesopause). The low top configuration has

38 vertical levels (L38) and an upper boundary at 40 km (mid stratosphere). As shown in Appendix 1, the vertical resolutions show the details of how these levels are defined. The high top configuration is better by more than a factor of two in the vertical resolution within the stratosphere (*Collins et al.,* 2008).

To obtain a clear view of the dynamic impact of the vertical height and resolution of the stratosphere alone on the ENSO, the 'control runs' of both the high top and the low top configurations were used instead of the historical runs, as performed in *Hardiman et al.* (2012). The control run is a simulation using pre-industrial levels of CO_2 and ozone that are held constant with time (*Taylor et al.*, 2009). In other words, the influence of volcanic eruptions and increasing CO_2 concentrations is eliminated. The pre-industrial control run also serves as the baseline for the analysis of historical and future scenarios, because it runs with non-evolving, pre-industrial conditions. The pre-industrial control run is used in addition to estimate the unforced variability of the model (*Taylor et al.*, 2009).

Therefore, the two sets of SST data in this work result from the pre-industrial control runs of the high top and low top configurations, which are publicly available from CMIP5 data centers and were downloaded by a DPhil student. The present research is based on these two sets of SST data. The SSTs used in the present work are determined by four variables: time, longitude, latitude, and depth. The depth is set to one meter below the ocean surface, which is sufficient to represent surface temperature variability. The time (t) unit is one month, which means the SST is a monthly average temperature. Both configurations were run over the same period of time, spanning 240 years (t=2880) in total. However, because some of the data are missing in the SST data sets of both configurations (details in the Appendix 2), only 150 years of data were used for the analysis, which is still sufficiently long to study quasi-periodic events such as the ENSO. Hence, adequate realizations for examining its statistics are available.

There are different ways of measuring the strength of the ENSO (Trenberth 1997). For the oceanic component, the most common method is to average the SST anomalies over certain regions termed Niño 1+2, Niño 3, Niño 4, and Niño 3.4 (*Fig. 2*). These SST-based indices are statistically positive for El Niño and negative for La Niña. In addition, there are various procedures to evaluate the SST anomalies. This study adopted two of these: one as SST anomalies with the seasonal cycle and the other without. The SST anomalies evaluated with the seasonal cycle computed by subtracting the annual mean SST from each SST, while those without the seasonal cycle are determined by subtracting the monthly average of the corresponding month (relevant Matlab codes are listed in Appendix 5).

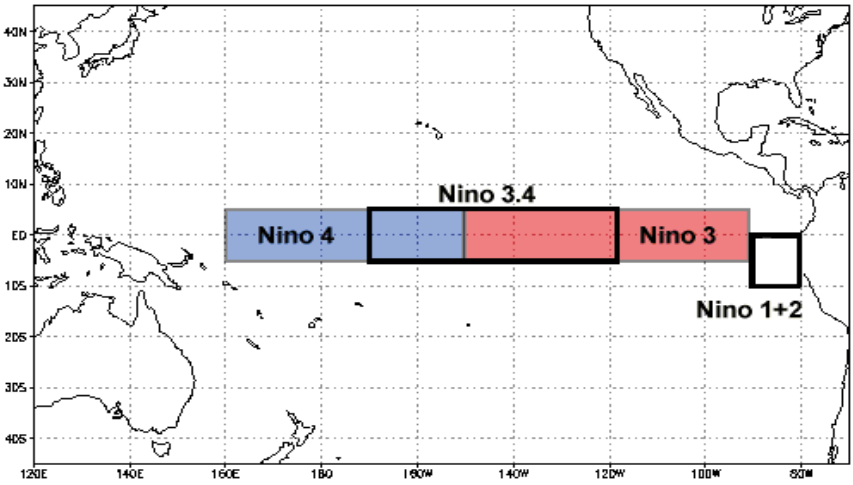

Fig. 2. Niño regions (www1.ncdc.noaa. gov/pub/data/cmb/teleconnections/nino-regions.gif)

El Niño events are then defined based on the conditions of certain thresholds being exceeded. The present work utilized the official National Oceanic and Atmospheric Administration (NOAA) definition stating that El Niño (La Niña) is a phenomenon in the equatorial Pacific Ocean characterized by five consecutive, three-month running-means of SST anomalies in the Niño 3.4 region above (below) the threshold of +0.5 ^{0}C (-0.5 ^{0}C). This standard measurement is known as the Oceanic Niño Index (ONI) (refer to NOAA ONI in the references for details).

In this work, the eastern and central equatorial Pacific Ocean regions, Niño3 (5S–5N, 90W–150W) and Niño 3.4 (5S5N, 120W–170W), were used to measure the strength of ENSO and ONI of Niño3.4. Moreover, to determine how well the SST was simulated in both model configurations, corresponding plots from NOAA were used for comparison.

3. Results and analysis

Using the high top simulations run with the Met Office Unified Model for CMIP5, and equivalent low top simulations, the present work studies the effects of the inclusion of a well-resolved stratosphere through general circulation model climate simulations of oceanic surface climate.

3.1. Global annual climatology

Figs. 3(a) and *(b)* show the climatology plots of global SST averaged over 150 years of control data for the high top and low top configurations, respectively, and (c) shows the observed annual mean sea surface temperature climatology from the National Oceanic and Atmospheric Administration (NOAA, http://www.cpc.ncep.noaa.gov/ products/precip/CWlink/climatology/). Both high top and low top configurations generally captured the warmest mean temperature, which occurs near 120° E in the tropics and the coldest around the North and South Poles. The findings agree well with plot (c), which also shows a cold tongue in the east Pacific Ocean along the coastline of South America.

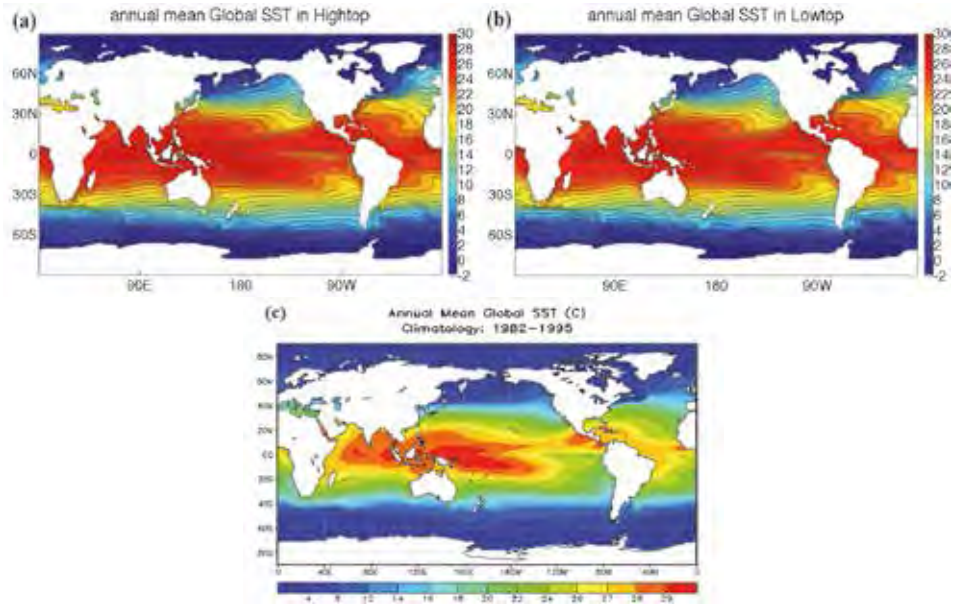

Fig. 3. Global sea surface temperature averaged over 150 years; (a) the high top model configuration, (b) the low top model configuration, and (c) the annual mean of global SST from 1982 to 1995, plot from the NOAA National Weather Service.

Fig. 4 shows the annual mean global SSTs of the high top run minus the low top run, i.e., the difference between *Figs. 3(a)* and *(b)*. The differences in temperature are less than 1 ^{0}C between the high top and low top model configurations, except in the northern extra-tropical region. The significant differences in the northern Atlantic region may be attributed to various causes, including the ocean circulation or different surface winds. All these possible

reasons result from the differences between the high top and low top configurations' parameters, which are different in the vertical extension and vertical resolution of the stratosphere.

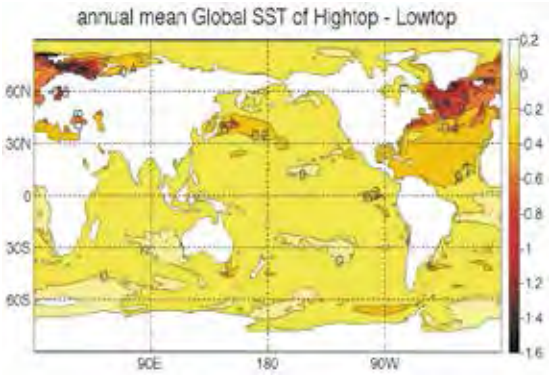

Fig. 4. Differences in the annual mean global SSTs between the high top and low top model configurations.

The present work then further examined whether the differences are attributable to noise or real signal differences between the high top and low top configurations. Thus, it is necessary to consider a steady state configuration. The first 20 (out of 240 available) years of data were disregarded to cut off the spinning up processes. However, noise still remains because of the random variability. To test whether the high top and low top annual SSTs are significantly different, a standard 2-sample t-test is introduced.

The t-test is the most commonly used method to evaluate the differences in the means between two samples with normal distributions (http://www.statsoft.com/ textbook/basic-statistics/). The *t*-value is determined as:

$$t = \frac{\overline{X1} - \overline{X2}}{S_{X1X2} \times \sqrt{\frac{2}{n}}}, \qquad (1)$$

$$S_{X1X2} = \sqrt{\frac{1}{2}(S_{X1}^2 + S_{X2}^2)}, \quad (2)$$

where $\overline{X_1}$ and $\overline{X_2}$ are the means of data sets 1 and 2, respectively. S×1×2 is the standard deviation of the combined data, defined by Eq.(2). n is the number of data points in each data set, which refers to the number of time points here (81885 points). In Matlab, the function h = ttest2(x,y) was used in this study.

The data were also tested for normality 1 similar variance to ensure the t-test was valid. In *Fig. 5*, the green area indicates that h=1 and blue indicates that h=0. This means that differences between the annual mean SSTs of the high top and low top model configurations in the green area result from real signal differences between the high top and low top runs at a 99% confidence level. In contrast, the possibility that the differences in the blue area are generated by noise cannot be disregarded. In the northern Atlantic Ocean region, the differences in annual mean temperature between the high top and low top model configurations are mainly statistically significant with 99% confidence. The SSTs in the high top configuration in this region are expected to have more variability as SST is more influenced by the stratosphere (*Baldwin* and *Dunkerton*, 2001).

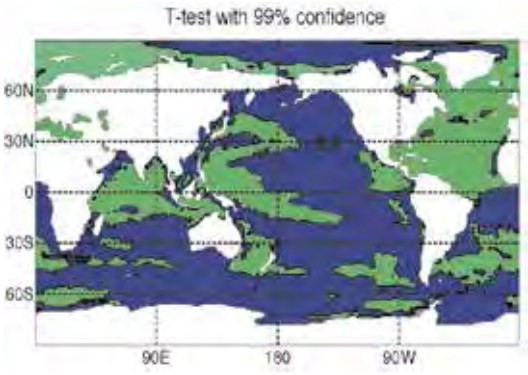

Fig. 5. t-test of the high top and low top annual mean global SSTs.

3.2. Global seasonal climatology

The seasonal mean climatology plots (*Fig. 6*) from high top and low top configurations and those from the NOAA National Centres for Environment and Predictions (NCEP) reanalysis are reported. The NOAA NCEP reanalysis data set is a continually updated grided data set representing the state of the Earth's atmosphere, incorporating observations and numerical weather prediction (NWP) model outputs dating back to 1948. It could serve as observational data or data close to observations. The data set was adopted to create seasonal SST climatology plots for comparison. (The plots are available at www.esrl.noaa.gov/psd/cgibin/data/composites/printpage.pl)

In this research, spring is considered to begin on the first day of March, and each season lasts 3 months, which is generally the definition used in meteorology for the northern hemisphere. Therefore, spring begins on March 1, summer on June 1, autumn on September 1, and winter on December 1.

The corresponding seasonal climatology plots from both the high top and low top configurations were initially compared with those from the NCEP reanalysis (plots in column 3 of *Fig. 6*). Both the high top and low top configurations generally agree well with the observations. *Fig. 7* shows the seasonal mean global SSTs for the high top minus the low top runs. The differences in temperature are less than 1 ^{0}C between the high top and low top configurations, except in the northern extra-tropical region, which is similar to the annual mean in *Fig. 4.* The t-test for these seasonal means was also computed, and the results show a pattern similar to the one in *Fig. 5*. The seasonal climatology is in reasonable agreement with the theory suggested in *Baldwin* and *Dunkerton* (2001).

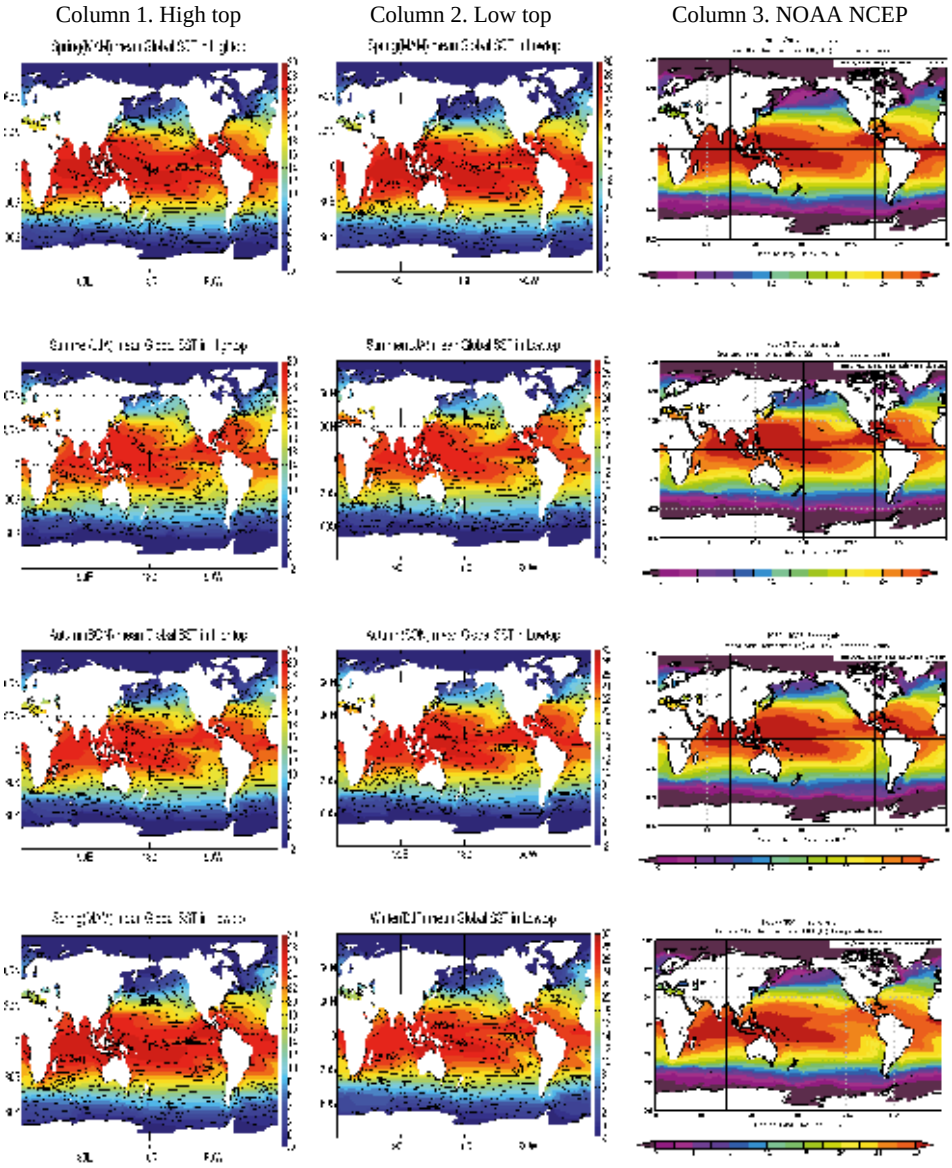

Fig. 6. Seasonal mean global sea surface temperature climatology plots from the high top configuration (column 1), the low top configuration (column 2), and the NOAA National Centres for Environment and Predictions (NCEP) reanalysis (column 3, available at http://www.esrl.noaa.gov/psd/cgi-bin/data/composites/printpage.pl). The first row represents spring (MAM), the second represents summer (JJA), the third row represents autumn (SON), and the last row represents winter (DJF).

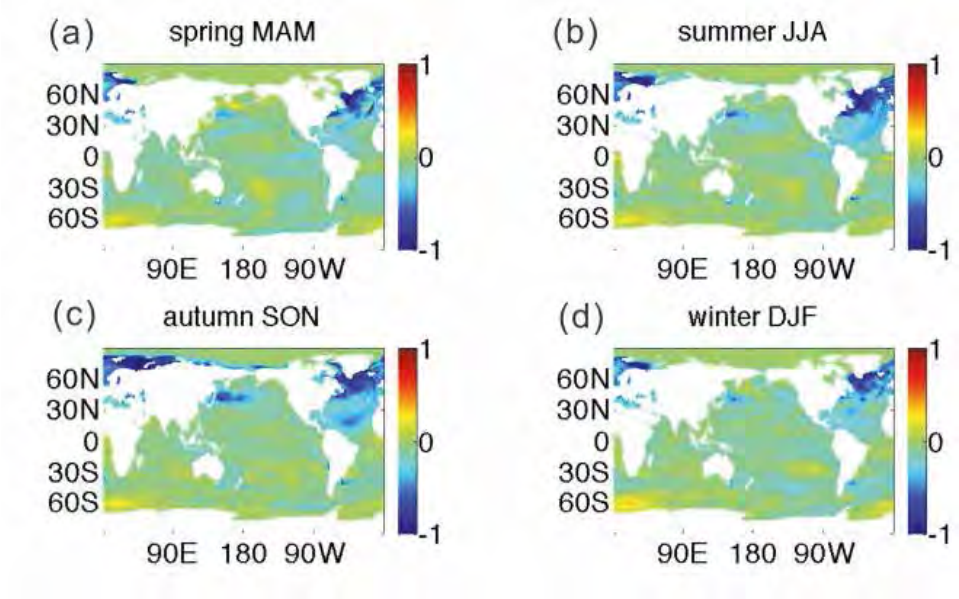

Fig. 7. Differences in the seasonal mean global SSTs between the high top and low top configurations during (a) spring (MAM), (b) summer (JJA), (c) autumn (SON), and (d) winter (DJF).

3.3. ENSO power spectrum

After studying the global behavior, the focus now is exclusively on the behavior of El Niño as described by the SST variability in the equatorial central and eastern Pacific region, i.e., the Niño 3 and Niño 3.4 regions of both the high top and low top configurations. The normalized power spectra of the corresponding monthly SST anomalies are computed by taking the fast Fourier transform of a time series as the output in its frequency spectrum (based on the code from http://blinkdagger.com/matlab/matlab-introductory-fft-tutorial/). Detailed Matlab codes are shown in Appendix 5.

First, the Niño indices were computed by averaging the SST anomalies over the corresponding Niño regions. For example, low Niño 3 indices without the seasonal cycle are computed by averaging the low top SST anomalies without the seasonal cycle over the Niño 3 region. The time series can then be plotted (*Fig. 8*), and the corresponding power spectra can then be computed (*Fig. 9*).

The power spectra of the low top Niño 3 indices with the seasonal cycle and those without the seasonal cycle are identical, except near the 1 year per cycle strong peak observed in that with the seasonal cycle. This finding indicates that the method adopted to remove the seasonal cycle is reasonable for investigating

the stratospheric impacts on ENSO quasi-periods. In addition, studying the differences without the representation of the seasonal cycle may be easier, because the effect of the seasonal cycle in power spectrum study can be eliminated. The horizontal axis represents the number of years per cycle over a total of 150 years, and a frequency band of 10 years per cycle is statistically more reliable than the rest. For example, a frequency of 10 years per cycle has 15 cycles as a sampling ensemble. Therefore, the focus was directed towards a range of 0 to 10 years per cycle on the Niño indices without the seasonal cycle.

The time series of the Niño 3 and Niño3.4 indices without the seasonal cycle for the both high top and low top configurations were produced (not shown here) as well as the corresponding power spectra (*Figs. 10* and *11*).

Both the high top Niño3 and Niño3.4 power spectra show peak bands over approximately 3 to 8 years per cycle, especially in the band of 7 to 8 years per cycle. The major ENSO events simulated in the low top configuration have quasi-periods of 7 to 8 years. Some of the ENSO events are located in a period band of 5 to 7 years, as well as a period of approximately 3 years. The low top power spectra also capture the peak band of 3 to 8 years per cycle. However, a stronger peak is observed in the region of 8 to 9 years per cycle. The major ENSO events simulated in the low top configuration have quasi-periods of 8 to 10 years. Only a few events have a quasi-period of approximately 6.5 years or 5.6 years.

By just considering the power spectra in *Figs. 10* and *11*, the high top configuration matches better with the general quasi-periods of the ENSO, which vary from 2 to 7 years. Most of the power is found within the band of 2 to 8 years for the high top configuration, whereas most of the power is found within the band of 9 to 10 years for the low top configuration. However, this conclusion is imprecise, thus requiring further study.

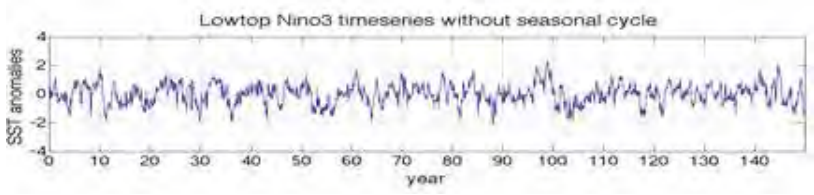

Fig. 8. The time series of the low top Niño 3 index: the SST anomalies without the seasonal cycle.

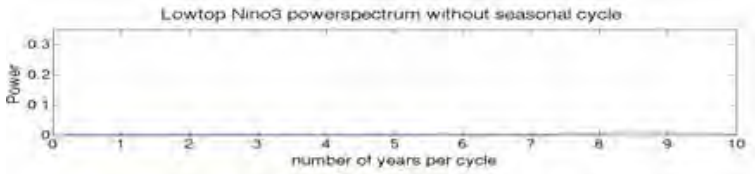

Fig. 9. Corresponding power spectra of time series in *Fig. 8*: the power spectrum without the seasonal cycle. The x-axis represents the number of years per cycle and the y-axis is the power.

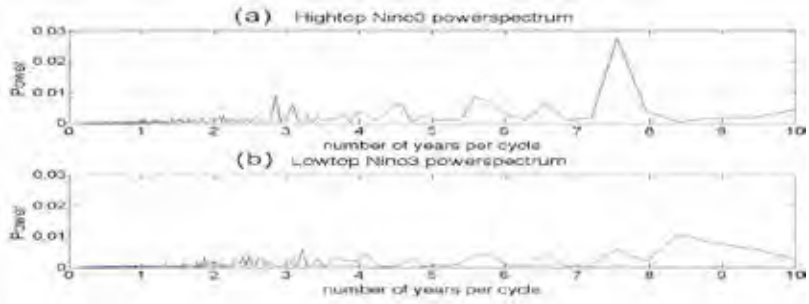

Fig. 10. Power spectra of the Niño3 SST anomalies without the seasonal cycle for (a) the high top configuration and (b) the low top configuration.

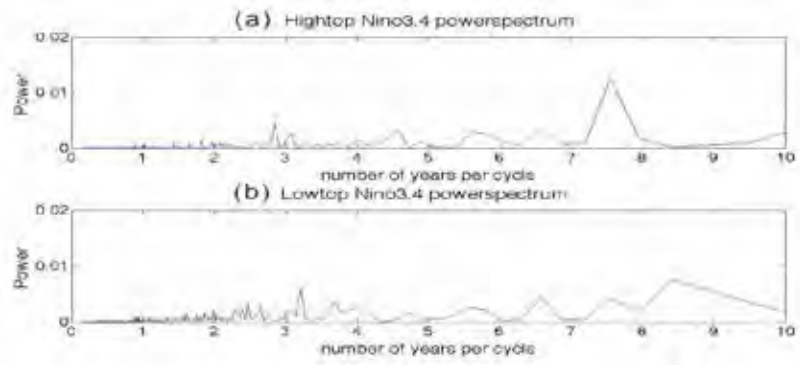

Fig. 11. Power spectra of the Niño 3.4 SST anomalies without the seasonal cycle for (a) the high top configuration and (b) the low top configuration.

Using the NOAA definition described in Section 2 to classify the El Niño events, Appendix 3 shows the time series of both the high top and low top Niño 3.4 ONI with a threshold of 0.5 ^{0}C. The power spectra (not shown) corresponding to the time series are similar to those shown in *Fig. 11*. The time series are then used to classify El Niño episodes. The criterion, which is often used to classify El Niño episodes, is that five consecutive 3-month running mean SST anomalies exceed the threshold. A list of El Niño episodes from the high top configuration can then be produced (Matlab code is in Appendix 5). With this list, several examples of the evolutions of El Niño episodes can then be plotted.

3.4. ENSO evolutions

Changes in the SST anomalies shown above during the ENSO cycle are accompanied by wind anomalies that cause the mean easterlies to weaken during El Niño events and strengthen during La Niña events. To illustrate the structure of the evolution over time during ENSO events, both high top and low top equatorial SSTs are considered as a function of longitude and time (*Figs. 12* and *13*), and SST anomalies along the Equatorial Pacific are represented as a Hovmoller diagram for the high top and low top configurations, respectively. A Hovmoller diagram created from the NOAA Tropical Atmosphere and Ocean (TAO) project of the equatorial SST and SST anomalies from 1990 to 2000 is available in Appendix 4 for reference.

Fig. 12 shows the high top SST anomalies in the equatorial Pacific region averaged over the latitude band 5S to 5N, and *Fig. 13* shows the low top configuration anomalies. A red color indicates a strong El Niño signal, and dark blue represents La Niña signals. A total of 15 diagrams were produced, covering 150 years each for the both high top and low top configurations. Each diagram covers a 10-year time scale (e.g., *Fig. 12*, years 30 to 39). Based on the high top configuration Hovmoller diagrams, the majority of El Niño events tend to reach their peak towards the end of the calendar year, such as the one shown in *Fig. 12*, in which the El Niño event reaches its maximum between December of year 36 and January of year 37. However, in the low top configuration diagrams, El Niño events do not show this seasonal phase-locking property. For example, the El Niño event between year 78 and year 79 shown in *Fig. 13* peaks around summer.

The Hovmoller diagrams shown in this work for both high top and low top configurations contain relatively active ENSO phenomena, with El Niño events followed by La Niña events. Several other diagrams show neutral conditions (normal years) following El Niño or La Niña events. This finding is consistent with the general characteristics of the ENSO presented in the introduction.

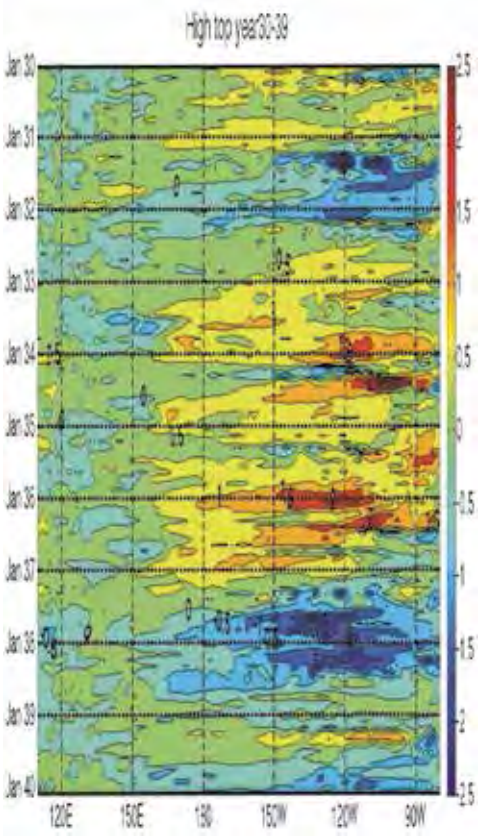

Fig. 12. Hovmoller diagram from January in year 30 to January in year 40 of the high top configuration simulation. The horizontal axis is the longitude from 110E to 80W; the vertical axis is the time stating with January in year 40 and ending with January in year 30. The SST anomalies plotted here are the high top SST anomalies in the equatorial region averaged over latitude 5S to 5N.

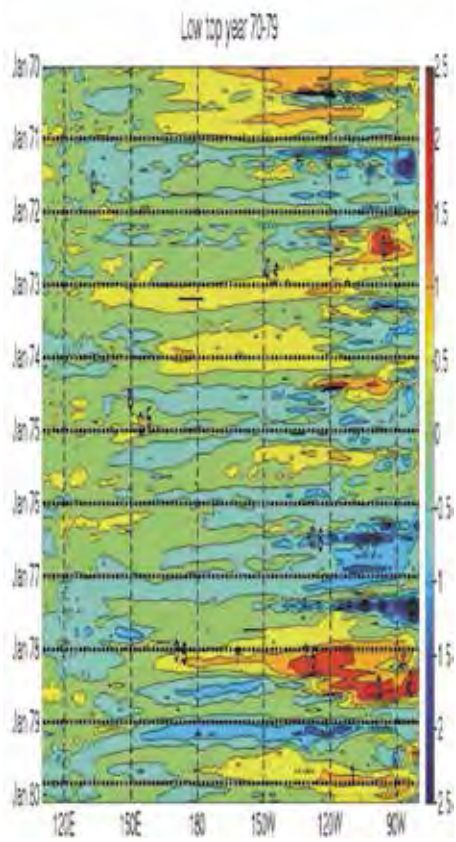

Fig. 13. Hovmoller diagram from January in year 70 to January in year 80 of the high top configuration simulation. The horizontal axis is the longitude from 110E to 80W; the vertical axis is the time stating with January in year 80 and ending with January in year 70. The SST anomalies plotted here are the low top SST anomalies in the Equatorial region averaged over latitude 5S to 5N.

4. Summary

This work uses pre-industrial control runs for the high top and low top configurations of HadGEM to investigate the effects of a well-resolved stratosphere on SSTs.

Annual mean and seasonal mean SSTs are well simulated in both configurations (*Figs. 4* and *6*). The annual and seasonal mean SSTs in the northern Atlantic Ocean are cooler with a well-resolved stratosphere (high top configuration) than without one (low top configuration) (*Figs. 4* and *7*). The differences between these SSTs could reach as high as 1.5 ^{0}C. This work further examined whether the temperature differences are statistically significant using a statistical method called the 't-test' (*Fig. 5*). The annual mean SST differences that occur in the northern Atlantic Ocean are statistically significant and are not due to random variability in these two configurations.

For Niño indices without the effects of the seasonal cycle, studying the ENSO quasi-periods in a power spectrum is easier, because the influence of the seasonal cycle is eliminated (*Fig. 9*). The configuration with a well-resolved stratosphere has a slight advantage in terms of simulating the ENSO quasi-period properly. The ENSO quasi-period is shown primarily to be a band of 2 to 8 years, close to observed periods of 2 to 7 years. The configuration without a well-resolved stratosphere shows an ENSO quasi-period primarily in the longer period band of 9 to 10 years (*Figs. 10* and *11*).

The Hovmoller diagrams (*Figs. 12* and *13*) for both high top and low top configurations show the irregularity of ENSO events, which is consistent with the general characteristics of ENSO descripted in introduction. Hence, both configurations show that El Niño events are not always followed by La Niña, and vice versa. Neutral conditions sometimes follow El Niño and La Niña events in an ENSO phenomenon. The Hovmoller diagrams also show that the configuration with a well-resolved stratosphere, El Niño events tend to reach their peaks towards the end of the calendar years, which is the seasonal phase locking phenomenon (*Fig. 13*).

5. Discussion and future work

This work suggests that an accurate representation of the stratosphere may be necessary to improve simulations of surface climate, especially during ENSO events. Both configurations appropriately simulated the long-term mean sea surface temperature. However, the configuration with a well-resolved stratosphere has an advantage in simulating the ENSO quasi-period and the El Niño phase-locking phenomenon. Thus, it is possible to conclude from this work that a model with a well-resolved stratosphere is better than one without in terms of simulating the ENSO. However, other properties of the ENSO need to be further examined.

Future work is needed to resolve the aforementioned problems. The following aspects need to be improved:

Surface wind stress data and thermocline data for both model configurations in the pre-industrial control run are needed to more explicitly investigate the

impact of the stratosphere on the ENSO (*Fig. 1*). As mentioned in Section 1, the ENSO is a phenomenon that results from a complex interaction between the atmosphere and the ocean. Based on a more accurate representation of surface wind stress, the atmosphere and ocean coupling strength can be studied further.

Further analysis of systematic errors is required. The model resolution subgrid processer must be parameterized, which introducing errors. In other words, anything influencing the Earth system that acts on scales less than the model grid size must just be put into the model as a best guess estimate. Clouds, for instance, play a large role on air temperatures but are often too small to be resolved in a model. Furthermore, *Guilyardi et al.* (2004) and *Bellenger et al.* (2014) suggested that multi-model analyses show that serious systematic errors persist in the simulated background climate as well as in the natural variability.

It is necessary to compare the outcomes of both configurations with observations. Since the present work makes use of a pre-industrial (1860) control run, it is less meaningful to compare the time series with observational data for it does not simulate a historical period. However, the power spectra can be compared with the observations. Comparing the outcome with other global climate models may also be useful.

Acknowledgments: We would like to take this chance to express our gratitude to those who assisted us in many ways during the writing of this study. Our deepest thank goes to Professor *Roy Gordon Grainger* from University of Oxford, for his explicit advice on sharpening our ideas and improving the accuracy of this paper.

References

Baldwin, M.P. and *Dunkerton, T.J.*, 2001: Stratospheric Harbingers of Anomalous weather regimes. *Science 294*, 581. https://doi.org/10.1126/science.1063315

Bell, C.J., Gray, L.J. , Charlton-Perez, A. J., Joshi, M. M., Scaife, A. A., 2009: Stratospheric Communication of El Nino Teleconnections to European Winter. *J. Climate 22*, 4083–4096. https://doi.org/10.1175/2009JCLI2717.1

Bellenger, H., Guilyardi, É., Leloup, J., Lengaigne, M., and Vialard, J., 2014: ENSO representation in climate models: from CMIP3 to CMIP5. *Climate Dynam. 42*, 1999–2018. https://doi.org/10.1007/s00382-013-1783-z

Bjerknes, J., 1966: A possible response of the atmospheric Hadley circulation to anomalies of ocean temperature. *Tellus 18*, 820–829. https://doi.org/10.3402/tellusa.v18i4.9712

Bjerknes, J., 1969: Atmospheric teleconnections from the equatorial Pacific. *Mon. Weather. Rev. 97*, 163–172. https://doi.org/10.1175/1520-0493(1969)097<0163:ATFTEP>2.3.CO;2

Cagnazzo, C. and *Manzini, E.*, 2009: Impact of the Stratosphere on the Winter Tropospheric Teleconnections between ENSO and the North Atlantic and European Region. *J. Climate 22*, 1223–1238. https://doi.org/10.1175/2008JCLI2549.1

Collins, W.J., Bellouin, N., Doutriaux-Boucher, M., Gedney, N., Hinton, T., Jones, C.D., Liddicoat, S., Martin, G., O'Connor, F., Rae, J., Senior, C., Totterdell, I., Woodward., S., Reichler, T., and Kim, J., 2008: Evaluation of the HadGEM2 model. Hadley Centre Technical Note HCTN 74, Met Office Hadley Centre, Exeter, UK. http://www.metoffice.gov.uk/learning/library/publications/science/climate-science

Garcia-Herrera, R., Calvo, N., Garcia, R. R., and Giorgetta, M. A., 2006: Propagation of the ENSO temperature signals into the middle atmosphere: A comparison of two general circulation models and ERA-40 reanalysis data. *J Geophys. Res. 111*, D06101. https://doi.org/10.1029/2005JD006061

Gerber, E.P.,Butler,A., Calvo, N., Charlton-Perez, A., Giorgetta, M., Manzini, E., Perlwitz, J., Polvani,L.M., Sassi, F., Scaife, A.A., Shaw, T.A., Son,S., and Watanabe, S., 2012: Assessing and Understanding the Impact of Stratospheric Dynamics and Variability on the Earth System. *Bull. Amer. Meteorol. Soc.*, online. https://doi.org/10.1175/BAMS-D-11-00145.1

Guilyardi, E., Gualdi, S., Slingo, J., Navarra, A., Delecluse, P., Cole, J., Madec, G., Roberts, M., Latif, M., and Terray, L., 2004: Representing El Nnio in Coupled Ocean Atmosphere GCMs: The Dominant Role of the Atmospheric Component. *J. Climate 17*, 4623–4629. https://doi.org/10.1175/JCLI-3260.1

Hardiman, S. C., Butchart, N., Hinton, T. J., Osprey, S. M., and Gray,L. J., 2012: The effect of a well resolved stratosphere on surface climate: differences between CMIP5 simulations with high and low top versions of the Met Office climate model. *J. Climate in 25*, 7083–7099 https://doi.org/10.1175/JCLI-D-11-00579.1

Kiehl, J.T. and *Boville, B.A.*, 1988: The radiative-dynamical response of a stratospheric-tropospheric general circulation model to changes in ozone. *J. Atmos. Sci. 45*, 1798–1817. https://doi.org/10.1175/1520-0469(1988)045<1798:TRDROA>2.0.CO;2

Labitzke, K. and *Van Loon, H.* 1989: The Southern Oscillation. part IX: The influence of volcanic eruptions on the Southern Oscillation in the stratosphere. *J Climate 2*,1223–1226. https://doi.org/10.1175/1520-0442(1989)002<1223:TSOPIT>2.0.CO;2

Manzini, E., Giorgetta, M.A., Esch, M., Kornblueh, L., and Roeckner, E., 2006: The influence of sea surface temperatures on the northern winter stratosphere: Ensemble simulations with the MAECHAM5 model. *J. Climate 19*, 3863–3881. https://doi.org/10.1175/JCLI3826.1

Martin, G.M., Esch, E., Kornblueh, L., and Roeckner, E., 2011: The HadGEM2 family of Met Office Unified Model climate configurations. *Geosci. Model Dev. 4*,723–757.

NOAA Climate Prediction Center (2005-12-19) 'How often do El Niño and La Niño typically occur?'. NOAA Oceanic Niño Index (ONI). http://www.ncdc.noaa.gov/teleconnections/enso/indicators/sst.php?num_months=5#nummonths_form

Taylor, K.E., Stouffer, R.J., and A. M., Gerald, 2009: A Summary of the CMIP5 Experiment Design. Lawrence Livermore National Laboratory Rep, pp 32.

Trenberth, K.E., 1997: The definition of El Nino. *Bull. Amer. Meteorol. Soc. 78*, 2771–2777. https://doi.org/10.1175/1520-0477(1997)078<2771:TDOENO>2.0.CO;2

Trenberth, K.E., Branstator, Grant W., Karoly, D., Kumar, A., Lau, N., Ropelewski, C., 1998: Progress during TOGA in under- standing and modeling global teleconnections associated with tropical sea surface temperatures. *J. Geophys. Res. 103*,14291–14324. https://doi.org/10.1029/97JC01444

Van Loon, H. and *Labitzke, K.*, 1987: The Southern Oscillation. Part V. *Mon. Weather Rev. 115*,357–369. https://doi.org/10.1175/1520-0493(1987)115<0357:TSOPVT>2.0.CO;2

Walker, G.T., 1923: Correlation in seasonal variation of weather VIII: A preliminary study of world weather. *Mem. Indian Meteorol. Dep. 24*, 75–131.

Walker, G.T., 1924: Correlation in seasonal variation of weather IX: A further study of world weather. *Mem. Indian Meteorol. Dep. 24*, 225–232.

Wang, B., 1995: Interdecadal changes in El Nino onset in the last four decades. *J. Climate 8*,267. https://doi.org/10.1175/1520-0442(1995)008<0267:ICIENO>2.0.CO;2

Appendix

Appendix 1. Currently available vertical resolutions

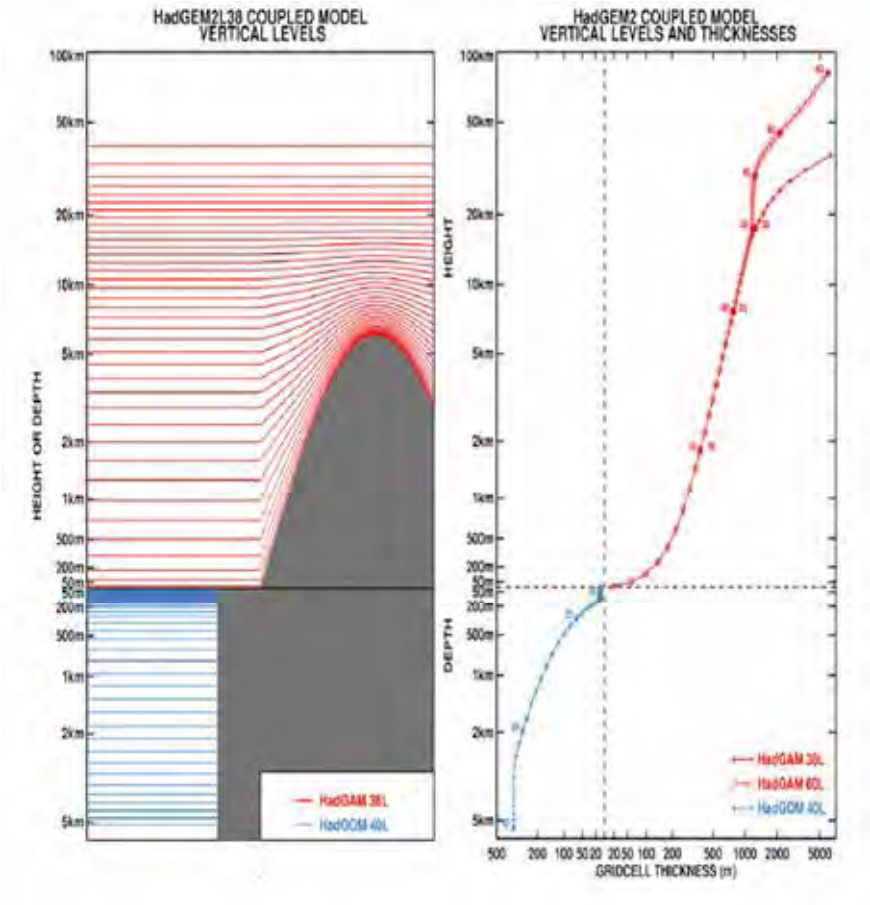

Fig. 14 .The vertical coordinate system in the atmosphere is height-based and terrain following near the bottom boundary. Left: Schematic picture, showing impact of orography on atmosphere model levels. Right: Model level height (or depth) vs. thickness plotted for the 40 L ocean model configuration and the 38 L and 60 L atmosphere model configurations at a point with zero orography (Martin *et al.*, 2011)

Appendix 2. Investigation of the original data

Note: Since the control run SST data of both high top and low top configurations have been produced only recently and have not been investigated, the present work has encountered difficulties due to the incompleteness of these original data, to which proper attention has not been previously given. In order to investigate these issues with the original results based on the incomplete data, different codes were used to reproduce the process, which was highly time-consuming. However, the present work was based on data that had been verified and shown to be reliable. Further investigations with the original incomplete data will still be helpful.

(1) Both data sets are in NetCDF form, which require to download a NetCDF toolbox from Unidata website (available at http://www.unidata.ucar.edu/downloads/netcdf/index.jsp), as the student version of Matlab does not contain this necessary toolbox.

(2) Use 'ncdump' comment to read the information on the data set, take the high top data file for example.

```
>> ncdump('p_temp_akgieo_pm_control.nc')
NetCDF-3 Classic p_temp_akgieo_pm_control.nc {

dimensions:
        depth = 1 ;
        latitude = 216 ;
        longitude = 360 ;
        t = UNLIMITED ; (2870 currently)

variables:
        // Preference 'PRESERVE_FVD':  false,
        // dimensions consistent with ncBrowse, not with native MATLAB netcdf package.
        single depth(depth), shape = [1]
                depth:units = "m"
                depth:positive = "down"
        single latitude(latitude), shape = [216]
                latitude:units = "degrees_north"
        single longitude(longitude), shape = [360]
                longitude:units = "degrees_east"
                longitude:point_spacing = "even"
                longitude:modulo = " "
        single t(t), shape = [2870]
                t:units = "days since 1859-12-01 00:00:00"
                t:calendar = "360_day"
                t:time_origin = "01-DEC-1859:00:00:00"
        single temp(t,depth,latitude,longitude), shape = [2870 1 216 360]
                temp:source = "Unified Model Output (Vn 6.6)."
                temp:name = "temp"
                temp:title = "POTENTIAL TEMPERATURE (OCEAN)  DEG.C"
                temp:date = "01/12/59"
                temp:time = "00:00"
                temp:long_name = "POTENTIAL TEMPERATURE (OCEAN)  DEG.C"
                temp:units = "degC"
                temp:missing_value = 2000000040081754685440.000000 f
                temp:_FillValue = 2000000040081754685440.000000 f
                temp:valid_min = -1.800000 f
                temp:valid_max = 119.068375 f
```

The time size was 2870, which is not 2880 for 240 years as expected, which implies that some data may be missing inside or at the end of the data set (as the model is still running).

For low top configurations, all the data were correctly obtained, except from the 1050 to 1100 months region. Thus, the exact month should be identified and the integer number of the data to the corresponding year should be cut-off to fix the problem above. This method will not affect the analysis as long as the high top and low top configurations have the same time scale, and the statistical study has enough realization.

Missing data of high top configurations occurred in several places around 2240 months and 2380 months. In the current study, the high top data set was not fixed because of time constrains. The latter portions of both models were disregarded since they do not affect the reliability of the outcome. Only data that cover 150 years were considered.

Appendix 3. Niño 3.4 ONI time series

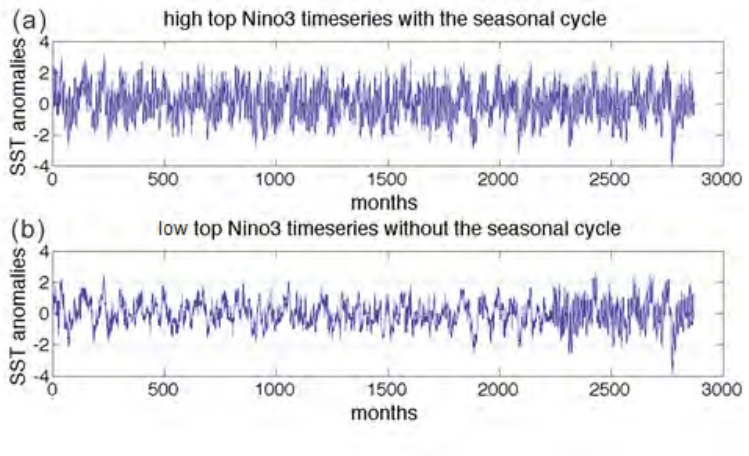

Fig. 15. Time series of the Niño 3.4 Oceanic El Niño Index for (a) the high top configuration and (b) the low top configuration produced from this work

Appendix 4. Hovmoller diagrams from NOAA

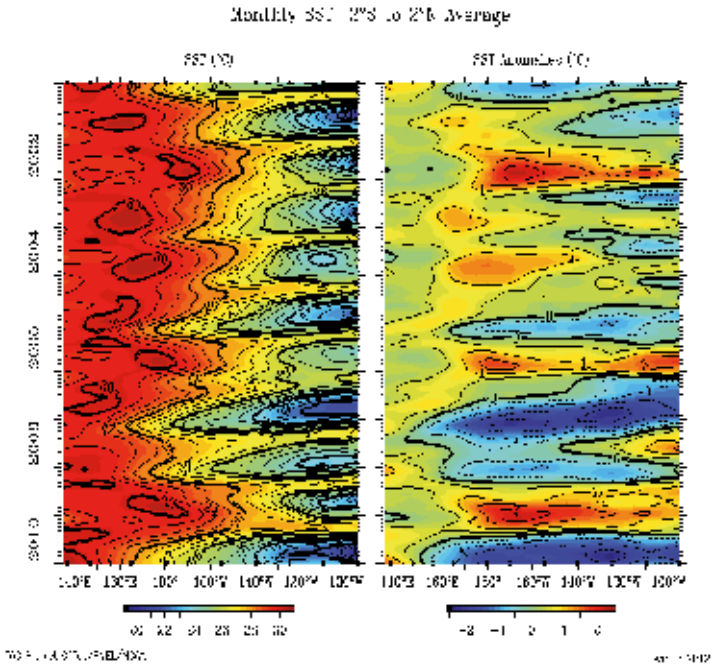

Fig. 16. Hovmoller diagrams from January 2000 to January 2010 of the NOAA Tropical Atmosphere Ocean project (TAO). The horizontal axis is the longitude from 310E to 90W; the vertical axis is the time stating with Jan 2010 and ending with Jan 2000

The first plot panel are mean SSTs in Equatorial region averaging over latitude 2S - 2N; the second plot panel is the SST anomalies in Equatorial region averaging over latitude 2S - 2N.
(Figures are available from http://www.pmel.noaa.gov/tao/jsdisplay/)

Appendix 5. Matlab code

1. Nino indices with and without the seasonal cycle
2. Power spectrum
   (1) Matlab script based on
   http://blinkdagger.com/matlab/matlab-introductory-fft-tutorial/
   (2) Adopted the script above for the power spectrum in this project, taken power spectrum of Nino 3 indices without seasonal cycle for example.
3. El Nino episodes (High top for example)

DOI:10.28974/idojaras.2020.1.2

IDŐJÁRÁS

Quarterly Journal of the Hungarian Meteorological Service
Vol. 124, No. 1, January – March, 2020, pp. 25–46

Evaluation of EURO-CORDEX and Med-CORDEX precipitation simulations for the Carpathian Region: Bias corrected data and projected changes

Csaba Zsolt Torma*[,1,2], **Anna Kis**[1,3], and **Rita Pongrácz**[1,3]

[1] *Department of Meteorology*
Eötvös Loránd University
Pázmány P. s. 1/A, H-1117, Budapest, Hungary

[2] *HAS Post-Doctoral Research Program*
Budapest, Hungary

[3] *Excellence Center, Faculty of Science*
Eötvös Loránd University
Brunszvik u. 2, H-2462, Martonvásár, Hungary

**Corresponding Author e-mail: tcsabi@caesar.elte.hu*

(Manuscript received in final form March 5, 2019)

Abstract—This study aims to give a brief overview of an ensemble of regional climate model (RCM) simulations with and without bias correction for daily precipitation for the Carpathian Region located in Central/Eastern Europe. Within the international initiative called the Coordinated Regional Downscaling Experiment (CORDEX), EURO-CORDEX and Med-CORDEX provide RCM simulations targeting Europe as a whole or in a part at the grid resolutions of 0.44° (~50 km) and 0.11° (~12 km). The ensemble of RCMs provides a huge amount of data, which are, however, prone to biases compared to high-resolution observations. First, the bias correction of the daily precipitation output of EURO-CORDEX and Med-CORDEX RCM ensemble at a common 0.11° × 0.11° horizontal grid resolution is performed based on the high-resolution, high-quality observational dataset CARPATCLIM. The region covered by the CARPATCLIM dataset can be considered as the Carpathian Region, for which the RCM ensemble (consisting of six members in total at 0.11° resolution) of a historical period (1976−2005) and under the Representative Concentration Pathway 8.5 (RCP8.5) over two future time slices (2021−2050 and 2070−2099) are assessed. Percentile-based bias correction method was used in order to adjust systematic biases in all simulated precipitation fields. The present study focuses on different precipitation climate indices derived from high-resolution RCM outputs over the entire Carpathian Region and specifically two sub-regions representing high- and lowlands

within the target region. The analyzed indices are as follows: the frequency of rainy days (RR1, days with a total rainfall of at least 1 mm), heavy precipitation days (RR10, days with a total rainfall of at least 10 mm), highest daily precipitation (RX1), maximum consecutive dry periods (CDD, the duration of the longest period with < 1 mm total daily precipitation), maximum consecutive wet periods (CWD, the duration of the longest period with > 1 mm total daily precipitation). Our results indicate that both the spatial distribution and magnitude of mean changes are similar to those found in previous works based on ENSEMBLES project simulations using a different greenhouse gas emission scenario. Furthermore, the present study also aims to introduce a high-resolution bias-corrected precipitation database, which can serve as input for climate change impact and adaptation studies to be carried out for the Carpathian Region and to provide important information to stakeholders and decision makers at local/regional/national levels.

Key-words: EURO-CORDEX, Med-CORDEX, CARPATCLIM, Carpathian Region, precipitation, bias correction, regional climate change, precipitation climate indices

1. Introduction

Information is of great value. One of the most crucial issues concerning climate change is: what impacts and changes will the changing climate have in the future? An important aspect of this question is that all precipitation projections come with a certain degree of uncertainty, which can have different sources. On the one hand, climate models can be useful tools for providing information on human induced climate change (*IPCC*, 2013), but on the other hand, the climatic parameters derived from climate model simulations are encumbered with high uncertainties. In fact, climate model simulations are characterized by biases compared to observations (*Torma et al*., 2011; *Kotlarski et al*., 2014). The main sources of uncertainties of global climate model (GCM) simulations can be attributed to (1) the internal climatic variability (in the absence of any external radiative forcing), (2) the implemented parameterization and model dynamics (model or response uncertainty), (3) the prescribed emission scenarios (scenario uncertainty), or (4) model systematic errors. Furthermore, RCM projections include additional uncertainties due to simulation configuration features as the choice of integration domain, resolution, lateral boundary conditions (LBCs), etc. Precipitation projections for the Carpathian Region, which is characterized by complex topography (with an altitude range between 27 m and 2655 m) and is located in Central Europe, where warmer Mediterranean climate meets the colder, continental northeastern European air masses, come with a certain degree of uncertainty (*IPCC*, 2013; *Gaál et al*., 2014; *Fischer et al*., 2015).

However, climate models may exhibit substantial systematic errors at different horizontal resolutions with distinct origins; valuable efforts can be done by adjusting or correcting those. In general, when bias correcting the raw climate simulation data, we can ensure the equal means between the observations and the bias-corrected climate simulation data (*Déqué et. al*., 2007). More recent and sophisticated methods (*Berg et al*., 2012; *Lafon et al*., 2013) ensure to fit the whole

distribution of climate model simulation to observations for a given meteorological variable (e.g., precipitation). The non-parametric (any prior knowledge of the theoretical distribution of the assessed variable is not required) quantile mapping method is considered to be among the best methods in reproducing not only the means but also other statistical properties (standard deviation, quantiles, etc). In principle, the quantile mapping method is easy to implement, which makes this method attractive among the climate research community (e.g., *Gudmundsson et al*., 2012; *Fang et al*., 2015). Note that the method requires a reliable observational dataset serving as reference data. From this point of view, a high-resolution, quality controlled, and homogenized observational dataset is essential in the bias correcting process. The CARPATCLIM (*Szalai et al*., 2013) dataset served as reference in the present study since it is a high-resolution and high-quality observational dataset, thus optimal for such purposes. Additionally, the CARPATCLIM dataset covers the region of interest, which is the Carpathian Region in this study.

A few RCM-based high-resolution (25 km or finer grid spacing) climate change projects have been accomplished encompassing the entire domain of the Carpathian Region in the last two decades, namely, ENSEMBLES (Ensembles-Based Predictions of Climate Changes and Their Impacts, 2004−2009; *Hewitt* and *Griggs*, 2004), CECILIA (Central and Eastern Europe Climate Change Impact and Vulnerability Assessment, 2006−2009; *Halenka*, 2007), and CORDEX (The Coordinated Regional Downscaling Experiment, *Giorgi et al*., 2009), which is the most recent international initiative with the task of producing reliable regional climate simulations for several well-defined domains under the supervision of the World Climate Research Programme (WCRP). EURO-CORDEX (*Jacob et al*., 2014) and Med-CORDEX (*Ruti et al*., 2016) both target Europe with a more and a less extended modeling domain, respectively. More precisely, EURO-CORDEX covers the entire continent, whereas Med-CORDEX focuses on the Mediterranean region, i.e., the southern part of Europe up to the 50°N. As being parts of CORDEX, they provide RCM simulations targeting European regions at grid resolutions of 0.44° (~50 km, medium resolution) and of 0.11° (~12 km, high-resolution).

We post-processed and analyzed a 6-member RCM ensemble (*Table 1*) involving EURO-CORDEX and Med-CORDEX high-resolution RCM simulations under the high-end greenhouse gas scenario RCP8.5 (*Moss et al*., 2010). Following the work of *Mezghani et al*. (2017), the percentile-based quantile mapping method was used for bias correcting precipitation projections obtained from the high-resolution RCM simulations. The bias-corrected daily total precipitation data obtained from the aforementioned RCM ensemble is assessed for future periods 2021−2050 and 2070−2099 with respect to the reference period 1976−2005 (which is the last 30 years of processed historical simulations) over the Carpathian Region. Changes in mean seasonal precipitation characteristics are reported not only for the entire Carpathian Region, but also for

two sub-regions selected along the same latitude representing low- and highlands with low and high mean altitudes, respectively (*Fig. 1*). Precipitation climate indices are also involved in the assessment of future precipitation characteristic and summarized in detail in *Table 2*.

Table 1. Overview of global (a-d) and regional (e-j) climate models used in the present study. For the regional models the letter in parenthesis indicates the driving GCM (from CMIP5) and whether the run accomplished over the EURO-CORDEX (EC) or MED-CORDEX (MC) domain.

Model	Modelling group	Horizontal resolution	Convection scheme
a, CNRM-CM5 (*Voldoire et al*., 2012)	Centre National de Recherches Meteorologiques and Centre Europeen de Recherches et de Formation Avancee en Calcul Scientifique, France	1.40625°	*Bougeault* (1985) with a *Kuo* (1965) type closure
b, EC-EARTH (*Hazeleger et al.*, 2010)	Irish Centre for High-End Computing, Ireland	1.125°	*Bechtold et al*. (2008)
c, HadGEM2-ES (Collins et al., 2011)	Met Office Hadley Centre, UK	1.875°(lon) × 1.2413°(lat)	*Derbyshire et al*. (2004)
d, MPI-ESM-LR (Jungclaus et al., 2010)	Max Planck Institute for Meteorology, Germany	1.875°	*Tiedtke* (1989)
e, ALADIN (a-MC) (Colin et al., 2010)	Centre National de Recherches Meteorologiques, France	0.11°	*Bougeault* (1985) with a *Kuo* (1965) type closure
f, CCLM (d-EC) (Rockel et al., 2008)	Climate Limited-area Modelling Community, Germany	0.11°	*Tiedtke* (1989)
g, RCA4 (c-EC) (Kupiainen et al., 2014)	Swedish Meteorological and Hydrological Institute, Rossby Centre, Sweden	0.11°	*Kain* and *Fritsch* (1993)
h, RACMO (b-EC) (Meijgaard van et al., 2012)	Royal Netherlands Meteorological Institute, The Netherlands	0.11°	*Tiedtke* (1989), *Nordeng* (1994), *Neggers et al.* (2009)
i, REMO (d-EC) (Jacob et al., 2001)	Max-Planck-Institut für Meteorologie, Germany	0.11°	*Tiedtke* (1989), *Nordeng* (1994), *Pfeifer* (2006)
j, RegCM4 (c-MC) (*Giorgi et al*., 2012)	International Centre for Theoretical Physics, Italy	0.11°	*Grell* (1993), *Emanuel* (1991)

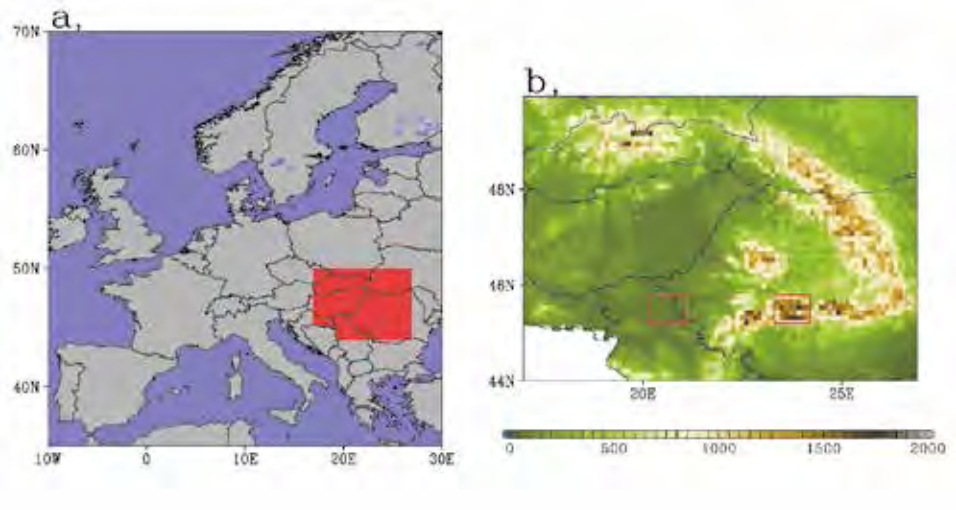

Fig. 1. Analysis region and topography (on a common 0.11° grid) over the Carpathian Region. a) Location of the analysis region within the European domain (red area); b) topography based on the GTOPO30 database. Sub-regions within red boxes are for representing low- and highlands in the region of interest. Units in b) are m.

Table 2. Description of analyzed precipitation indices.

Abbreviation of index	Definition	Unit
CDD	Maximum number of consecutive dry days with daily precipitation sum < 1 mm	day
CWD	Maximum number of consecutive wet days with daily precipitation sum > 1 mm	day
RR1	Number of wet days (daily precipitation sum > 1 mm)	day
RR10	Number of days with heavy precipitation (daily precipitation sum ≥ 10 mm)	day
RX1	Highest total daily precipitation	mm

The present study follows the work of *Mezghani et al.* (2017), which introduces a publicly available bias-corrected dataset consisting projected daily precipitation totals along with near surface air temperature (minimum, maximum, and mean) for the region of Poland. Here we present the initial steps towards

creating similar dataset for the Carpathian Region with special focus on precipitation. One of the main objectives of the present work is to introduce a publicly available high-resolution RCM based, bias-corrected precipitation dataset, which can serve as a fundamental input for application to regional risk assessment or impact studies for the Carpathian Region. We also aim to provide a brief summary on the assessment of the possible future climatic precipitation characteristics over the Carpathian Region based on such dataset. The introduced dataset will be publicly available shortly after publication, upon request.

2. Data and methods

2.1. The CARPATCLIM gridded observational dataset

The CARPATCLIM dataset provides 16 daily meteorological variables (including daily total precipitation) and related derived indicators for the period of 1961−2010 encompassing the Carpathian Region at 0.1° × 0.1° horizontal grid resolution (*Szalai et al.*, 2013). This climatic database is station-based, state-of-the-art quality controlled, covers the Carpathian Mountains and the whole Carpathian Basin (approximately 500 000 km^2), and freely available for scientific purposes through the following link: http://www.carpatclim-eu.org. From a network of meteorological weather stations covering the region of interest 904 stations were used in collecting daily total precipitation data (*Spinoni et al.*, 2015). The technique of Multiple Analysis of Series for Homogenized Database (MASH; *Szentimrey*, 2007) is used for homogenization and checking data quality, while the Meteorological Interpolation based on Surface Homogenized Database (MISH; *Szentimrey* and *Bihari*, 2006) method is applied for gridding and interpolating within the CARPATCLIM database. Thus, the CARPATCLIM is the ideal and best currently publicly available high-resolution climatological dataset, which includes daily total precipitation that can serve as reference for bias correction studies over the Carpathian Region with special focus on precipitation.

2.2. RCM simulations

Several RCM experiments have been accomplished over each of the 14 different sub-regions of the globe in the framework of CORDEX. The European continent is targeted by two different sub-programs of CORDEX: EURO-CORDEX and Med-CORDEX, both provide RCM simulations for Europe (Med-CORDEX is focusing on the Mediterranean region, between the latitudes of 30°N and 50°N) at grid resolutions of 0.44° and 0.11°. As both initiatives provide data encompassing the whole Carpathian Region, they are ideal for investigating RCM simulations obtained from the EURO- and Med-CORDEX programs. We used an ensemble of RCM simulations consisting six RCM simulations driven by four different GCMs (*Table 1*). All RCM simulations involved in the present study

follow the high-end RCP8.5 scenario (*Moss et al*., 2010) and were obtained from the EURO-CORDEX and the Med-CORDEX initiatives. Although some RCMs are available with multiple simulations (different driving GCMs, different realizations, etc.) within the CORDEX project, our selected ensemble includes only one simulation from each individual RCM in the interest of any of the RCMs that should not dominate the selected ensemble. Our study focuses on present climatic conditions (1976−2005), and on projections for the future periods 2021−2050 (near future) and 2070−2099 (far future) with respect to the reference period 1976−2005 (the last 30 years of historic runs within CORDEX).

Since the RCM simulations and the CARPATCLIM dataset are available on different horizontal grids, all simulation data and observational data were interpolated onto a common grid by following the previous work of *Torma et al.* (2015). The Climate Data Operators software (CDO, https://code.mpimet.mpg.de/projects/cdo) was used during the interpolation processes. More specifically, the distance-weighted average remapping method was used in order to all data share the same grid. However, several different interpolation methods are available in the framework of CDO, such as bicubic, bilinear, distance weighted, or field conserving, the distance-weighted method was found to be the most spatial pattern consistent between different horizontal resolutions over regions with complex topography (*Torma et al*., 2015). All data reported in the present study are represented on the common 0.11° grid.

2.3. Bias correction method

Either of available bias correction methods is used, one has to keep in mind, that bias correction is a mere statistical post-processing tool, which cannot be expected to overcome the fundamental shortcomings of any climate model (*Maraun*, 2016). To correct the systematic biases present in our RCM ensemble, we used a percentile-based bias correction method (or quantile mapping; *Wang et al*., 2016). The percentile-based bias correction technique is considered to be flexible and to be a prominent representative of the most frequently used bias correction techniques by the climate research community (e.g., *Teutschbein* and *Seibert*, 2013; *Rajczak et al*., 2016; *Kis et al*., 2017). In general, the quantile mapping method employs a quantile-based transformation of distributions in order to adjust the variance of simulated distribution to better match the variance obtained from the observations. It is also important to note that the quantile mapping has a few limitations, which must be taken into consideration. The method is considered to be sensitive to the length and quality of the calibration or reference dataset (*Fowler* and *Kilsby*, 2007). Regarding the aforementioned facts, under different climatic conditions, unobserved values may not present in the calibration dataset in that given time period (*Themeßl et al*., 2010). Following the work of *Mezghani et al*. (2017), the adjustment of all simulated daily precipitation to the observations was performed for each grid cell after interpolating all data onto the common

0.11° grid. In addition, an adjustment for rainy day frequencies was applied with a given threshold of 0 mm day^{-1}. In order to compute the threshold, the probability of rainy days was first determined based on observations, and then all modeled data below that threshold were set to zero. Accordingly, all modeled data were fitted to the portion of the distributions of observed rainy days. The present study represents data derived from simulations bias-corrected by the quantile mapping technique, where the number of quantiles was set to 1000. Additionally, the quantile mapping method was used on seasonal scale in order to take into account the seasonal behavior of biases (e.g., correction factors were computed for each season for each grid cell). Finally, the quantiles of the RCM simulations for the analyzed periods were mapped onto the corresponding quantiles derived from observations using the entire available period of CARPATCLIM (1961−2010). This was done in order to minimize the sensitivity to the choice of the calibration time period, when some unobserved values may lie outside the range, if too short time period is considered as calibration period.

2.4. Precipitation climate indices

Based on the bias-corrected high-resolution RCM simulation ensemble, in total, 5 precipitation climate indices defined by the Expert Team on Climate Change Detection and Indices (ETCCDI, e.g., *Sillmann et al*., 2013) are calculated and analyzed over the region of interest. The analyzed indices are as follows: frequency of rainy days (RR1), heavy precipitation days (RR10), highest daily precipitation sum (RX1), maximum consecutive dry periods (CDD), and maximum consecutive wet periods (CWD). Indices selected from ETCCDI are analyzed for the following reasons: RR1 and CWD represent wet conditions, while CDD represents dry spells. RX1 represents precipitation intensity and RR10 represents extreme precipitation events. All indices are reported in detail in *Table 2.*

3. Results

3.1. Evaluating raw and bias-corrected RCM-simulated precipitation against CARPATCLIM (1976–2005)

The period 1976–2005 served as reference for which the historical RCM simulations were evaluated first. Model errors usually show spatial and temporal dependence. More specifically, wet and dry regions vary depending on the season across the region of interest. The biases of simulated seasonal and annual precipitation fields compared to CARPATCLIM show their maxima over mountainous regions, which can also be attributed to the low station network density over those regions. As the thorough comparison of analyzed RCMs before and after bias-correction are out of the scope of the present work, here we report only a representative example of RCM performance on representing precipitation

in the form of spatial plot in *Fig. 2*. For this purpose, we show as an example of the high-resolution run of RCM named as KNMI-RACMO22E (hereafter RACMO) driven by EC-EARTH validation against CARPATCLIM before and after bias correcting the daily precipitation sums. *Fig. 2* depicts not only the negative or positive bias of simulated precipitation, but in the form of root mean square error (RMSE) given on each panel, it also gives information on the magnitude of overall deviation between simulated and observed precipitation taking into account all the grid cells over the entire Carpathian Region. In case of RACMO, the raw data holds high seasonal RMSE, especially in winter and summer (16.28 mm month^{-1} and 16.43 mm month^{-1}, respectively), while for the transition seasons, slightly more modest RMSE values were found (12.09 mm month^{-1} for spring, and 12.22 mm month^{-1} for autumn). Relatively smaller RMSE was found on annual scale (10.23 mm month^{-1}). The highest biases occurred along the chains of the Carpathian Mountains, especially over the southern flanks of the Southern Carpathians, where a positive bias can exceed 100 mm month^{-1}. The RMSEs obtained from the bias-corrected simulation found to be much lower compared to those derived from the raw simulation and were close to 2 mm month^{-1} for annual and seasonal means, except for summer (4.01 mm month^{-1}). After bias correction, the annual and seasonal precipitation biases on individual grid cells were found to be between –20 and +20 mm month^{-1}.

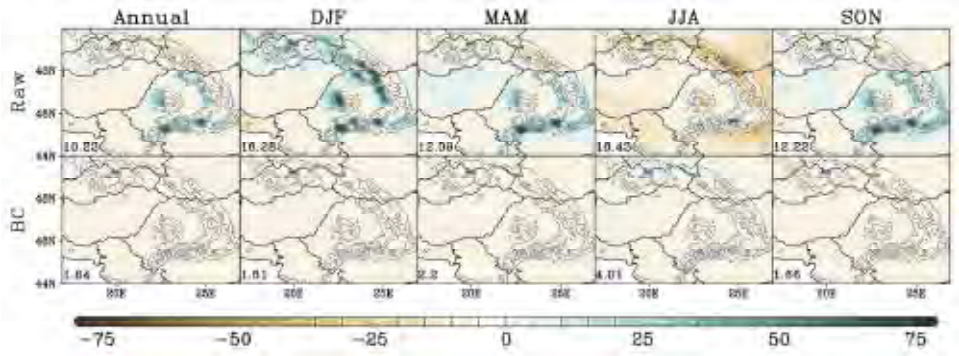

Fig. 2. Annual and seasonal precipitation bias with (labeled as "BC" maps in the lower panels) and without (labeled as "Raw" maps in the upper panels) bias correction for the RACMO model simulation (see *Table 1*), for the period 1976–2005. The root-mean-squared error (RMSE) is averaged for the whole domain and is given in mm/month in the lower left corner of each panel.

Next, the RCM simulations were assessed for the reference period over the two selected sub-regions along the same latitude (*Figs. 3* and *4*), as an additional

measure on their performance across the Carpathian Region. *Fig. 3* reports the individual RCMs simulated seasonal precipitation totals for both sub-regions with and without bias correction. In general, over the mountainous sub-region, the seasonal precipitation positive bias is more pronounced compared to the sub-region with low average elevation. Taking into account all simulations, the relative bias varies between –49% and 53% (–37% and 159%) in the case of lowland (mountainous region). On the one hand, over the mountainous sub-region, the exaggerated simulated seasonal precipitation totals (compared to CARPATCLIM) can indicate the relatively sparse station network density. On the other hand, it can also allude to the fact, that how challenging the simulation of precipitation over mountainous region can be. *Fig. 3* also shows that seasonal precipitation is overestimated by most of the models over both sub-regions in all seasons, except for summer (JJA). Note that only the ALADIN model overestimated the seasonal total precipitation regardless of the season and sub-region with a somehow exaggerated summer maximum. The latter may be attributed to the sensitivity of the applied convective parameterization. After the quantile mapping bias correction, the biases present in the raw simulated seasonal precipitation totals were almost eliminated, leading to negligible differences between RCMs and observational seasonal precipitation totals. In the case of lowland (mountainous region), the relative bias is between –4% and 4% (–1% and 8%), which is substantially less than in the case of raw simulations. The remaining slight discrepancy is due to the fact that the calibration period (1961–2010) embeds the reference period (1976–2005) used in our study and they are not identical.

Other metrics are also known to evaluate the performance of climate models in simulating present climatic conditions (*Zhao et al*., 2013). Besides computing the mean bias and RMSE (e.g., *Fig. 2*), the degree of statistical similarity between the simulated and observational fields can be concisely quantified and displayed in the form of Taylor diagrams (*Taylor*, 2001). *Fig. 4* summarizes the performance of each RCM over the sub-regions with respect to CARPATCLIM over the period 1976−2005 in the form of Taylor diagrams. More specifically, the azimuthal position of symbols present in *Fig. 4* refers to the correlation coefficient between the RCM simulations and the CARPATCLIM, the radial distance from the reference point (marked with black dot) to each symbol indicate the centered RMSE, while the distance from point 0 shows the ratio of standard deviation derived from the RCM simulations against the observations. In *Fig. 4*, all RCM simulations are represented by symbols filled with different colors. More precisely, color refers to the RCM, while the raw and bias-corrected simulated precipitation is denoted by different symbols (square and circle, respectively). Among others, *Fig. 4* reports the imperfection of the raw RCM simulations, which is partly due to biases inherited by the driving fields provided by GCMs. Regardless the sub-region, the raw RCM simulations are characterized by very low (or even negative) and high (in case of ALADIN) spatial correlation

coefficients, varying between –0.3 and 0.93, while after bias correcting the RCM simulated precipitation fields, the spatial correlation coefficients are found to be within the range of 0.65 and 0.94 (so the low and negative values disappear). Regarding the centered RMSE and the standard deviation, both metrics show the clear signal of the bias correction on RCM precipitation fields by tending towards them to the observations over both sub-regions. It is also interesting to note that RACMO with and without bias correction is among the best performing RCMs over both sub-regions. In summary, over both sub-regions the application of the bias correction method leads to the substantial improvement of the simulated precipitation distributions with respect to CARPATCLIM.

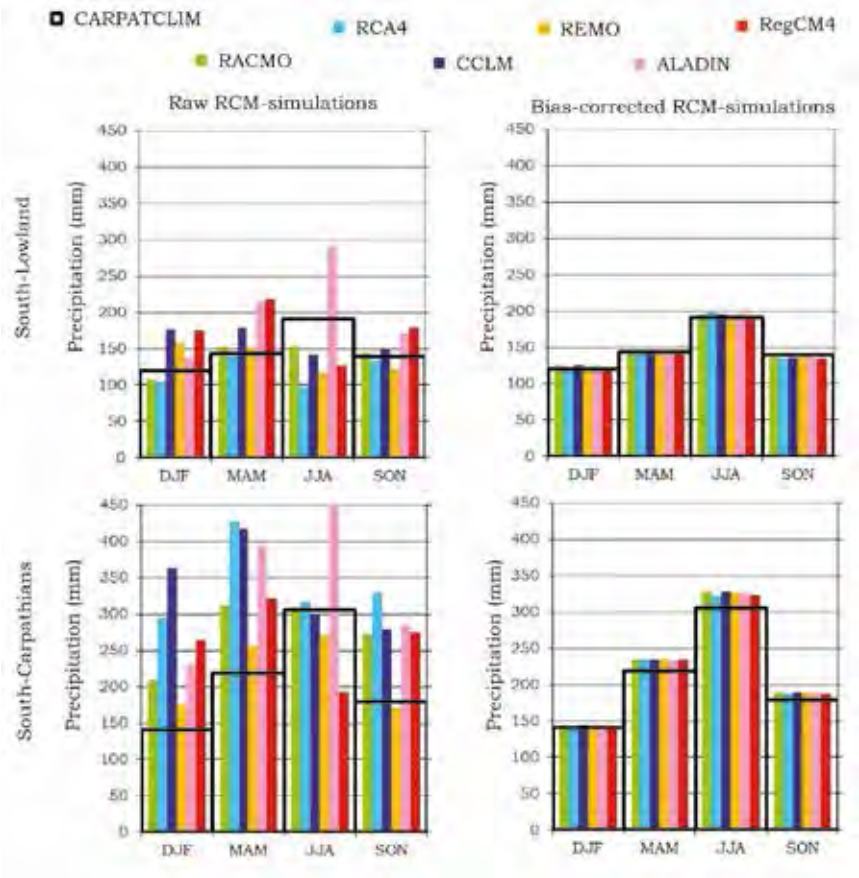

Fig. 3. Seasonal precipitation bias over the sub-regions with (on the right) and without (on the left) bias correction for all RCMs (see Table 1), for the period 1976–2005.

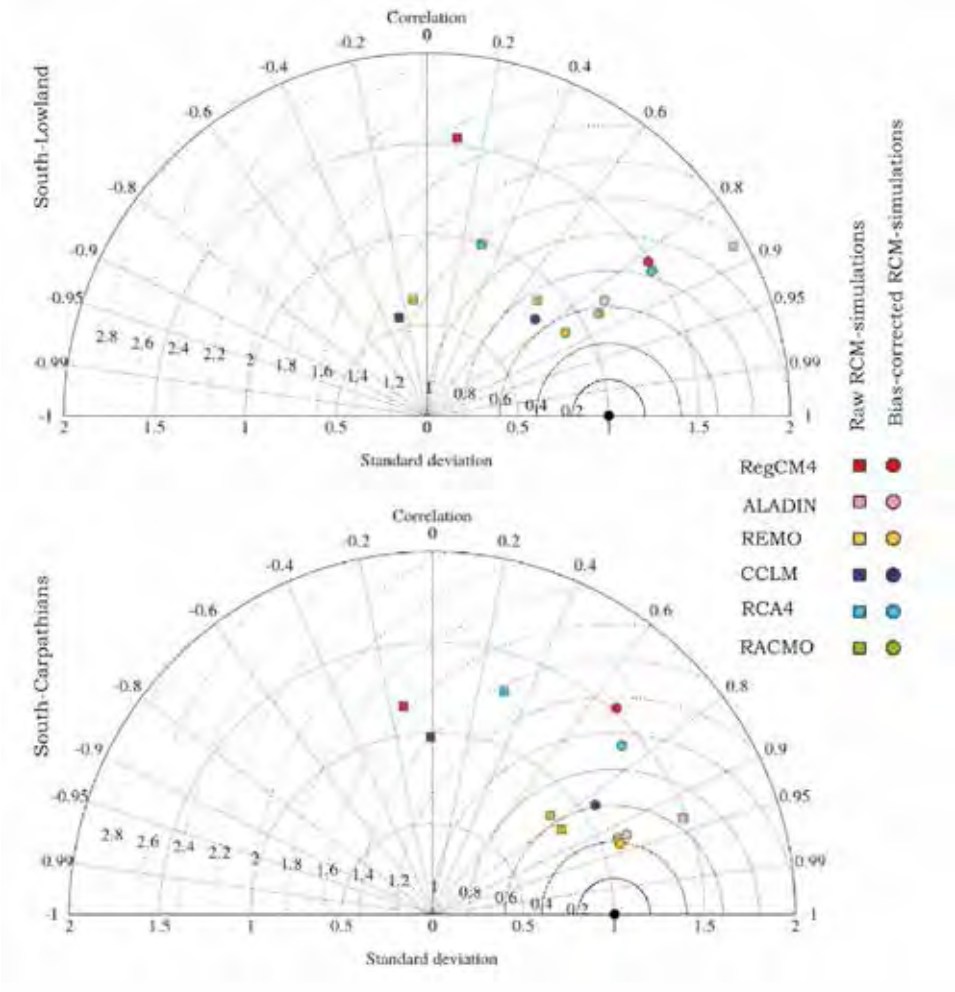

Fig. 4. Taylor diagrams for summarizing the statistical characteristics of simulation data and the effect of bias correction for the two selected sub-regions, for the period 1976–2005.

3.2. Seasonal mean precipitation projections

After having assessed the RCM simulations with and without bias correction for the historical period 1976−2005, now we turn our attention to the projected precipitation changes. Toward this purpose, we analyzed the six-member high-resolution bias-corrected RCM ensemble including projections following

the high-end RCP8.5 greenhouse gas concentration for the future time periods: 2021−2050 and 2070−2099, with respect to the historical period. *Fig. 5* shows the change in ensemble mean seasonal precipitation over the region of interest for both future time slices. Dotting indicates regions where at least 4 out of 6 RCMs agree on that seasonal precipitation change is statistically significant at the 90% confidence level using two-sided t-test. Thus, findings are considered robust over regions highlighted by dots. According to *Fig. 5*, it is evident that during the 21st century, the region of interest is likely to experience a general increase in precipitation during all seasons, except for summer. On the one hand, the mean seasonal precipitation changes found to be similar for both future time periods (regarding the sign and spatial pattern), but on the other hand, these changes found to be more prominent and robust by the end of the 21st century (2070−2099) than by the mid-century. For this reason, hereafter in this section, we focus on changes by the end of the century. The bias-corrected RCM simulations show a maximum winter (DJF) precipitation increase in the western part of the region (mostly covering the territory of Hungary) and surrounding the mountain chains of the Carpathians exceeding 30%. The latter one can indicate the sign of the topographically induced precipitation change. Regarding the sign and spatial distribution, very similar but less pronounced changes were found for spring (MAM) within the range of 0%–30%. It is also interesting to note that precipitation increase in DJF and MAM tends to be more moderate towards the south over the Southern Carpathians, while the precipitation change signal is the opposite over the northern and southern parts of the Southern Carpathians (-15% – 0%, but being mostly not significant) in autumn (SON). Obviously, the orientation of the southern flanks of the Carpathians plays a key role in this process (precipitation shadowing effect) along with the prevailing wind flow change (*Zappa et al*., 2013). The models project significant precipitation decrease in the summer season (JJA) over the selected domain, reaching a maximum of -25% – -30% over the southern regions of the Carpathian Basin. This raises a major concern on future fresh water availability (e.g., irrigation), since the precipitation maximum occurs in the summer season. In summary, our findings on seasonal precipitation change confirm previous studies reporting general winter precipitation increase and decrease in summer over the region of interest (e.g., *Jacob et al*., 2014; *Kis et al*., 2017).

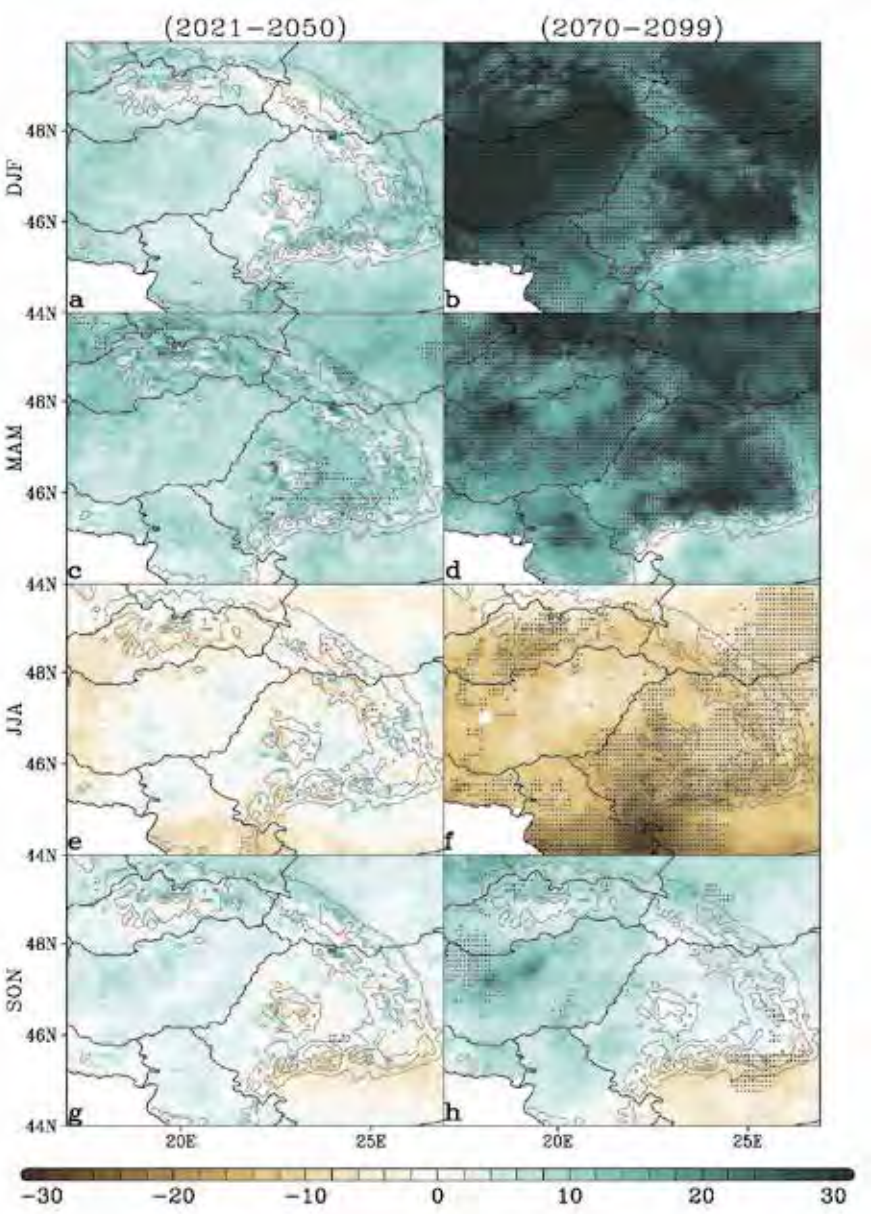

Fig. 5. Ensemble average of the projected seasonal precipitation change over the Carpathian Region. The changes are presented for two different future time slices compared with the reference period 1976–2005, derived from the RCM ensemble (see *Table 1*; units of percentage of reference period values) for 2021–2050: DJF (a), MAM (c), JJA (e), and SON (g). For far future (2070–2099): DJF (b), MAM (d), JJA (f), and SON (h). Dotting indicates areas where at least 4 out of 6 RCMs agree on that precipitation change is statistically significant at the 90% confidence level. Thin contour lines represent topography with the intervals of 500 m. Thick black lines show country borders.

3.3. Estimated changes of precipitation climate indices

As discussed in the previous Section (3.2) the assessed RCM ensemble projects robust precipitation change only by the end of the 21st century, therefore climate index changes are analyzed and reported only for this later future period in *Fig. 6.* More specifically, Figure 6 summarizes the spatial distribution of the aforementioned climate indices' winter and summer changes projected by 2070−2099 with respect to 1976−2005 over the Carpathian Region. Noting that, indices which take into account several days (CDD and CWD) and based on bias corrected model data are not expected to perfectly match with observations due to some residual bias. Whilst one-day indices based on bias corrected data expected to be really close to observations. The estimated changes of CWD and CDD are not found significant in DJF. Whilst, the maximum length of dry periods in JJA is projected to be significantly extended over most part of the region with a maximum increase of 7 days. Note that the maximum increase of CDD is projected over the same region where the maximum summer precipitation decrease is estimated to occur. CWD does not show robust change with any particular topographical feature. Estimated change of RR1 shows similar seasonal and spatial patterns to CDD changes. More specifically, the absolute increase of RR1 is robust in winter and estimated to increase by 2–3 days per season in the northern regions of the Carpathian Mountains. While in summer, the projected decrease of RR1 is found to be significant technically all over the region of interest. It is also interesting to note the evidence of the topographical modulation of the Carpathians on the spatial distribution in the summer change of RR1, where the estimated decrease can reach 7– 8 days per season over the mountain peaks. The more abundant future winter precipitation reported in Section 3.2. is associated with more intense daily precipitation totals: RX1 relative change is estimated to reach a maximum of 50% over the Northeastern Carpathians. A moderate increase of RX1 is simulated for summer over most part of the Carpathian Region, but with a slight decrease (~10%) over the western part of the Southern Carpathians. In terms of the sign and spatial distribution, the increase of RR10 is found to be in line with the winter precipitation change, even the changes are robust only for the interior of the chains of Carpathians reaching 2–3 days more per season. In the meanwhile, RR10 in summer is estimated to decrease with the same magnitude over the peaks of the Carpathians, the region of Croatia, and the southern parts of Serbia covered by the CARPATCLIM dataset.

In summary, the number of days with precipitation total exceeding 1 mm is estimated to decrease; also the intensity of rainy events is estimated to decrease over the western part of the Southern Carpathians, leading the climate of that region considerably drier. In addition, the overall winter and summer precipitation changes are fostered by the projected robust changes found for RX1 and RR1, respectively.

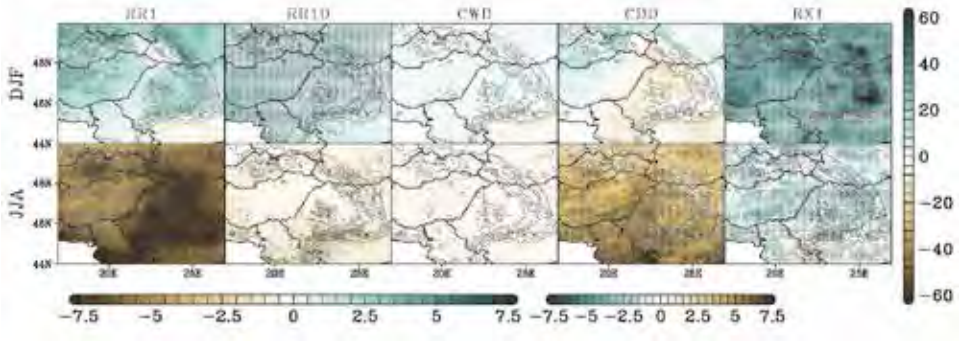

Fig. 6. Ensemble average of the projected winter (DJF) and summer (JJA) change of precipitation climate indices for the far future (2070–2099). Dotting indicates areas where at least 4 out of 6 RCMs agree on that precipitation change is statistically significant at the 90% confidence level. Thin contour lines represent topography with the intervals of 500 m. Units are day season^{-1}, while changes are given in % for RX1. Thick black lines show country borders.

In order to assess the possible role of orography on the projected changes in precipitation and the analyzed climate indices, further assessments are needed. Toward this purpose, the estimated changes of the precipitation indices over the two specific sub-regions within the Carpathian Region for time slices 2021−2050 and 2070−2099 compared to the reference period 1976−2005 were computed and are reported in *Fig. 7*. The bars with different colors depict the arithmetic mean of the climate index derived from the RCM simulations (2021−2050 is represented by dark, while 2070−2099 period is represented by light colors), while the vertical black line displayed over each bar indicates the minimum and maximum values (the entire spread of the six-member RCM ensemble). According to the sign and magnitude of the estimated changes of climate indices, slight differences were found between the analyzed sub-regions. In general, most climate indices show a more pronounced change in the far future (2070−2099) compared to the earlier time slice (2021−2050). No substantial changes were found for the frequency of rainy days (RR1) in DJF and MAM, while it is projected to decrease in JJA and SON by ~10–20% on average, with the maximum in JJA. Slight differences can be seen over the sub-regions in the estimated seasonal changes of RR10. More specifically, days with precipitation sum exceeding 10 mm are projected to become more frequent in DJF and MAM (by ~30–50% and by 20–35%, respectively). It is interesting to note that a more pronounced increase in RR10 is found over the sub-region with lower mean elevation. By the end of the 21st century, about 15% less RR10 is projected in JJA over both sub-regions, whilst small decrease (~5%) along with a more robust increase (~15%) is estimated in SON over the low elevation and the mountainous sub-regions, respectively. Thus, the estimated changes of RR1 and

RR10 envision the modulation of the annual precipitation cycle over the analyzed sub-regions. RX1 shows very similar increase in all seasons over both sub-regions (~10–20% in DJF, ~10–30% in MAM, and ~5–15% in JJA), except for SON, when over the mountainous sub-region, the increase of RX1 is more modest (~10%) compared to the other sub-region at lower elevation (~35%). According to the assessed precipitation climate indices, longer wet periods (CWD) are projected in DJF and MAM (~10%), whereas shorter wet periods in JJA and in SON (5–15%). Along with this, longer dry periods (CDD) are projected over both sub-regions by ~10–30% in JJA and SON by the end of the 21st century. Note that only negligible changes are estimated in CDD for DJF and MAM, regardless of the sub-region.

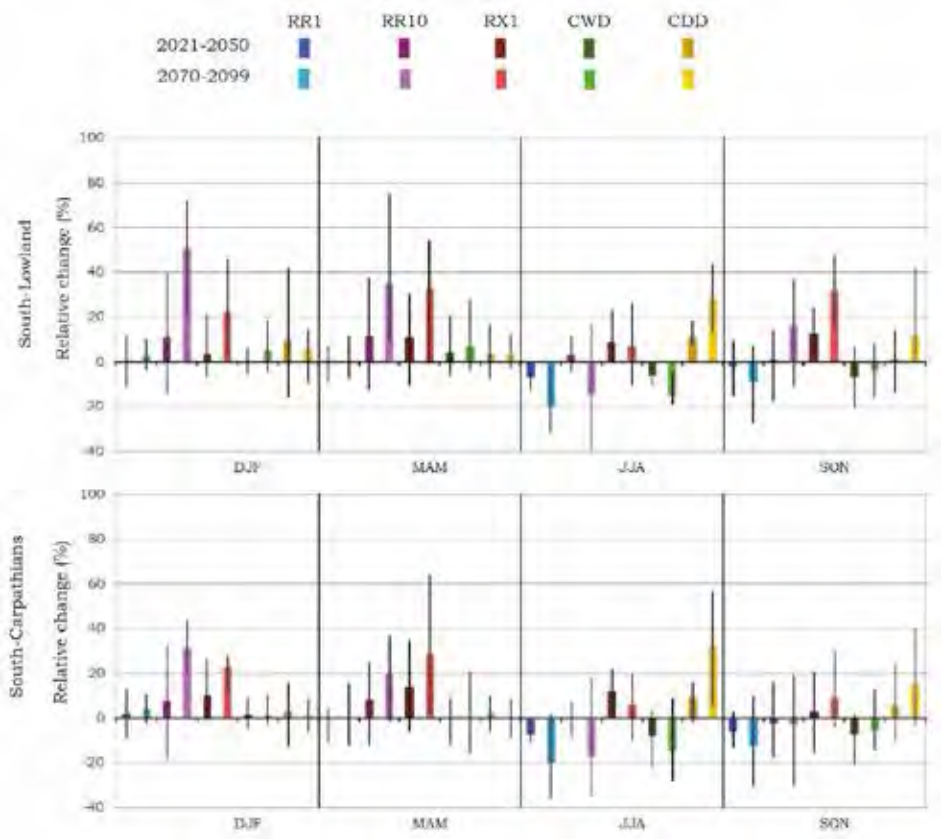

Fig. 7. Relative changes of precipitation climate indices for the two sub-regions for 2021–2050 and 2070–2099 with respect to 1976–2005. Changes are given in %. Color bars represent the ensemble mean, while the vertical black lines are drawn from the smallest to the greatest projected changes.

Different processes and different underlying mechanisms may be responsible for the seasonal precipitation change patterns projected for these sub-regions and for the entire Carpathian Region, which is in fact exciting and also challenging to be addressed, but the detailed investigation of it is out of the scope of the present study. It will be investigated in a future work.

4. Conclusions

The high-resolution, high-quality observational dataset, CARPATCLIM served as long-term reference dataset for the Carpathian Region to correct for systematic bias in daily precipitation simulated by six EURO-CORDEX and Med-CORDEX simulations. Following the work of *Mezghani et al.* (2017), the quantile mapping method was used in order to eliminate biases present in the ensemble of RCM simulations. The six-member high-resolution (~12 km) RCM ensemble assuming the high-emission greenhouse gas scenario (RCP8.5) was assessed for future time slices 2021–2050 and 2070–2099 with respect to the reference period 1976–2005. Based on the ensemble mean of bias-corrected RCM simulations, more robust changes are projected by the end of the 21st century than for the near future time slice. The present study also reported on the projected changes of precipitation climate indices over the entire Carpathian Region and with special focus on two sub-regions representing high- and lowlands within the target region. The sub-regions were selected in favor of the quest of the role of topography on precipitation change. The analyzed climate indices are: frequency of rainy days (RR1, days with a total rainfall of at least 1 mm), heavy precipitation days (RR10, days with a total rainfall of at least 10 mm), highest daily total precipitation (RX1), maximum consecutive dry days (CDD, duration of the longest period with < 1 mm total daily precipitation), maximum consecutive wet periods (CWD, duration of the longest period with > 1 mm total daily precipitation).

By and large, the key findings of the present study are as follows: (1) the influence of orography on seasonal precipitation change is evident throughout the analyzed periods, (2) the estimated precipitation change holds an unequivocal seasonality as most models project significant winter (DJF) precipitation increase (~30%), while in general drier (~20%) summers (JJA) are projected over the most part of the Carpathian Region by the end of the 21st century, (3) RR10 shows a clear signal of increase over the sub-regions in all seasons (10 –50%), except for summer (~ -15%), while RX1 shows increase in all seasons.

The present study also introduces a high-resolution bias-corrected precipitation database, which can serve as input for further climate change impact and adaptation studies to be carried out for the Carpathian Region at local/regional/national levels. Furthermore, the present work draws attention to the important role that a high-resolution, quality controlled observational dataset may play not only in validation studies, but also in creating bias-corrected RCM simulation-based dataset for further scientific purposes.

Acknowledgements: The research leading to these results has received funding from the following sources: the Hungarian Academy of Sciences under the Premium Postdoctoral Research Program and János Bolyai Research Scholarship, the Széchenyi 2020 program, the European Regional Development Fund and the Hungarian Government via the AgroMo project (GINOP-2.3.2-15-2016-00028), the Hungarian National Research, Development and Innovation Fund under grant K-129162. All data from EURO-CORDEX and Med-CORDEX modeling groups used in this work and CARPATCLIM, Database © European Commission – JRC 2013, along with GTOPO30 data provided by the U.S. Geological Survey are acknowledged. The data used in this work can be found at the following web sites: http://cordexesg.dmi.dk/esgf-web-fe/ (EURO-CORDEX), http://www.medcordex.eu/medcordex.php (MED_CORDEX), http://www.carpatclim-eu.org/pages/download/ (CARPATCLIM)

References

Bechtold, P., Köhler, M., Jung, T., Doblas-Reyes, F., Leutbecher, M., Rodwell, M.J., Vitart, F., and *Balsamo, G.*, 2008: Advances in simulating atmospheric variability with the ECMWF model: From synoptic to decadal time-scales. *Q. J. Roy. Meteor. Soc., 134*, 1337–1351. https://doi.org/10.1002/qj.289

Berg, P., Feldmann, H., and *Panitz, H.J.*, 2012: Bias correction of high resolution regional climate model data. *J. Hydrol. 448–449*, 80–92. https://doi.org/10.1016/j.jhydrol.2012.04.026

Bougeault, P., 1985: A Simple Parameterization of the Large-Scale Effects of Cumulus Convection. *Mon. Weather Rev. 113*, 2108–2121. https://doi.org/10.1175/1520-0493(1985)113<2108:ASPOTL>2.0.CO;2

Colin, J., Déqué, M., Radu, R., and *Somot, S.*, 2010: Sensitivity studies of heavy precipitations in limited area model climate simulation: influence of the size of the domain and the use of the spectral nudging technique. *Tellus A 62*, 591–604. https://doi.org/10.1111/j.1600-0870.2010.00467.x

Collins, W.J. Bellouin, N., Doutriaux-Boucher, M., Gedney, N., Halloran, P., Hinton, T., Hughes, J., Jones, C.D., Joshi, M., Liddicoat, S., Martin, G., O'Connor, F., Rae, J., Senior, C., Sitch, S., Totterdell, I., Wiltshire, A., and *Woodward, S.*, 2011: Development and evaluation of an Earth System model, HADGEM2. *Geosci. Model Dev. 4*, 1051–1075. https://doi.org/10.5194/gmd-4-1051-2011

Derbyshire, S.H., Beau, I., Bechtold, P., Grandpeix, J.-Y., Piriou, J.-M., Redelsperger, J.-L., and *Soares, P.M.M.*, 2004: Sensitivity of moist convection to environmental humidity. *Q. J. Roy. Meteor. Soc. 130*, 3055–3079. https://doi.org/10.1256/qj.03.130

Déqué, M., Rowell, D. P., Lüthi, D., Giorgi, F., Christensen, J. H., Rockel, B., Jacob, D., Kjellström, E., de Castro, M., and *van den Hurk, B.*, 2007: An intercomparison of regional climate simulations for Europe: assessing uncertainties in model projections, *Climatic Change 81*, 53–70. https://doi.org/10.1007/s10584-006-9228-x

Emanuel, K.A., 1991: A scheme for representing cumulus convection in large-scale models. *J. Atmos. Sci. 48*, 2313–2335. https://doi.org/10.1175/1520-0469(1991)048<2313:ASFRCC>2.0.CO;2

Fang, G.H., Yang, J., Chen, Y.N., and *Zammit, C.*, 2015: Comparing bias correction methods in downscaling meteorological variables for a hydrologic impact study in an arid area in China. *Hydrol. Earth Syst. Sci. 19*, 2547–2559. https://doi.org/10.5194/hess-19-2547-2015

Fischer, A.M., Keller, D.E., Liniger, M.A., Rajczak, J, Schär, C., and *Appenzeller, C.*, 2015: Projected changes in precipitation intensity and frequency in Switzerland: a multi-model perspective. *Int. J. Climatol. 35*, 3204–3219. https://doi.org/10.1002/joc.4162

Fowler, H.J. and *Kilsby, C.G.*, 2007: Using regional climate model data to simulate historical and future river flows in northwest England. *Climatic Change 80*, 337–367. https://doi.org/10.1007/s10584-006-9117-3

Gaál, L., Beranová, R., Hlavcová, K., and *Kysely, J.*, 2014: Climate Change Scenarios of Precipitation Extremes in the Carpathian Region Based on an Ensemble of Regional Climate Models. *Adv. Meteor.* ID 943487, 14p. https://doi.org/10.1155/2014/943487

Giorgi, F., Jones, C., and *Asrar, G.*, 2009: Addressing climate information needs at the regional level: The CORDEX framework. *WMO Bulletin 58*, 175–183.

Giorgi, F., Coppola, E., Solmon. F., Mariotti, L., Sylla, M.B., Bi, X., Elguindi, N., Diro, G.T., Nair, V., Giuliani, G., Turuncoglu, U.U., Cozzini, S., Güttler, I., O'Brien, T.A., Tawfik, A.B., Shalaby, A., Zakey, A.S., Steiner, A.L., Stordal, F., Sloan, L.C., and *Brankovic, C.*, 2012: RegCM4: model description and preliminary results over multiple CORDEX domains. *Clim. Res. 52*, 7–29. https://doi.org/10.3354/cr01018

Grell, G., 1993: Prognostic evaluation of assumptions used by cumulus parameterizations. *Mon. Weather Rev. 121*, 764–787. https://doi.org/10.1175/1520-0493(1993)121<0764:PEOAUB>2.0.CO;2

Gudmundsson, L., Bremnes, J.B., Haugen, J.E., and *Engen-Skaugen, T.*, 2012: Technical Note: Downscaling RCM precipitation to the station scale using statistical transformations - a comparison of methods. *Hydrol. Earth Sys. Sci. 16*, 3383–3390. https://doi.org/10.5194/hess-16-3383-2012

Halenka, T., 2007: On the Assessment of Climate Change Impacts in Central and Eastern Europe - EC FP6 Project CECILIA. *Geophys. Res. Abstr. 9*, 10545.

Hazeleger,W., Severijns, C., Semmler, T., Stefanescu, S., Yang, S., Wang, X., Wyser, K., Dutra, E., Baldasano, J.M., Bintanja, R., Bougeault, P., Caballero, R., Ekman, A.M.L., Christensen, J.H., van den Hurk, B., Jimenez, P., Jones, C., Kållberg, P., Koenigk, T., McGrath, R., Miranda, P., van Noije, T., Palmer, T., Parodi, J.A., Schmith, T., Selten, F., Storelvmo, T., Sterl, A., Tapamo, H., Vancoppenolle, M., Viterbo, P., and *Willén, U.*, 2010: EC-EARTH: a seamless Earth system prediction approach in action. *Bull. Am. Meteorol. Soc. 91*, 1357–1375. https://doi.org/10.1175/2010BAMS2877.1

Hewitt, C.D., and *Griggs, D.*, 2004: Ensembles-Based Predictions of Climate Changes and Their Impacts. *Eos Trans. AGU 85*(52), 566–567. https://doi.org/10.1029/2004EO520005

IPCC, 2013: Climate Change 2013: The Physical Science Basis. Contribution of Working Group I to the Fifth Assessment Report of the Intergovernmental Panel on Climate Change [Stocker, T.F., D. Qin, G.-K. Plattner, M. Tignor, S.K. Allen, J. Boschung, A. Nauels, Y. Xia, V. Bex and P.M. Midgley (eds.)]. Cambridge University Press, Cambridge, United Kingdom and New York, NY, USA. https://doi.org/10.1017/CBO9781107415324

Jacob, D., van den Hurk, B., Andræ, U., Elgered, G., Fortelius, C., Graham, L. P., Jackson, S. D., Karstens, U., Kopken, C., Lindau, R., Podzun, R., Rockel, B., Rubel, F., Sass, B.H., Smith, R.N.B., and *Yang, X.*, 2001: A comprehensive model intercomparison study investigating the water budget during the BALTEX-PIDCAP period. *Meteorol. Atmos. Phys. 77*, 19–43. https://doi.org/10.1007/s007030170015

Jacob, D., Petersen, J., Eggert, B., Alias, A., Christensen, O.B., Bouwer, L.M., Braun, A., Colette, A., Déqué, M., Georgievski, G., Georgopoulou, E., Gobiet, A., Menut, L., Nikulin, G., Haensler, A., Hempelmann, N., Jones, C., Keuler, K., Kovats, S., Kröner, N., Kotlarski, S., Kriegsmann, A., Martin, E., van Meijgaard, E., Moseley, C., Pfeifer, S., Preuschmann, S., Radermacher, C., Radtke, K., Rechid, D., Rounsevel, M., Samuelsson, P., Somot, S., Soussana, J.-F., Teichmann, C., Valentini, R., Vautard, R., Weber, B., and *Yiou, P.*, 2014: EURO-CORDEX New high resolution climate change projections for European impact research. *Reg. Environ. Change 14*, 563–578. https://doi.org/10.1007/s10113-013-0499-2

Jungclaus, J.H., Lorenz, S.J., Timmreck, C., Reick, C.H., Brovkin, V., Six, K., Segschneider, J., Giorgetta, M.A., Crowley, T.J., Pongratz, J., Krivova, N.A., Vieira, L.E., Solanki, S.K., Klocke, D., Botzet, M., Esch, M., Gayler, V., Haak, H., Raddatz, T.J., Roeckner, E., Schnur, R., Widmann, H., Claussen, M., Stevens, B., and *Marotzke, J.*, 2010: Climate and carbon cycle variability over the last millennium. *Clim. Past 6*, 723–737. https://doi.org/10.5194/cp-6-723-2010

Kain, J.S., and *Fritsch, J.M.*, 1993: Convective parameterization for mesoscale models: the Kain-Fritsch scheme. The representation of cumulus convection in numerical models. *Meteorol. Monogr. 24*, 165–170. https://doi.org/10.1007/978-1-935704-13-3_16

Kis, A., Pongrácz, R., and *Bartholy, J.*, 2017: Multi-model analysis of regional dry and wet conditions for the Carpathian Region. *Int. J. Climatol. 37*, 4543–4560. https://doi.org/10.1002/joc.5104

Kotlarski, S., Keuler, K., Christensen, O.B., Colette, A., Déqué, M., Gobiet, A., Goergen, K., Jacob, D., Lüthi, D., van Meijgaard, E., Nikulin, G., Schär, C., Teichmann, C., Vautard, R., Warrach-Sagi, K., and *Wulfmeyer, V.*, 2014: Regional climate modeling on European scales: A joint standard evaluation of the EURO-CORDEX RCM ensemble. *Geosci. Model Dev. 7*, 1297–1333. https://doi.org/10.5194/gmd-7-1297-2014

Kuo, H.L., 1965: On Formation and Intensification of Tropical Cyclones Through Latent Heat Release by Cumulus Convection. *J. Atmos. Sci. 22*, 40–63. https://doi.org/10.1175/1520-0469(1965)022<0040:OFAIOT>2.0.CO;2

Kupiainen, M., Jansson, C., Samuelsson, P., Jones, C., Willén, U., Hansson, U., Ullerstig, A., Wang, S., and *Döscher, R.*, 2014: Rossby Centre regional atmospheric model, RCA4, Rossby Center News Letter, Rossby Centre regional atmospheric model, RCA4

Lafon, T., Dadson, S., Buys, G., and *Prudhomme, C.*, 2013: Bias correction of daily precipitation simulated by a regional climate model: a comparison of methods, *Int. J. Climatol. 33*, 1367–1381. https://doi.org/10.1002/joc.3518

Maraun, D., 2016: Bias correcting climate change simulations – a critical review. *Curr. Clim. Change Rep., 2*, 211–220. https://doi.org/10.1007/s40641-016-0050-x

van Meijgaard, E., van Ulft, L.H., Lenderink, G., de Roode, S.R., Wipfler, L., Boers, R., and *Timmermans, R.M.A.*, 2012: Refinement and application of a regional atmospheric model for climate scenario calculations of Western Europe. *Climate Scenarios*. KvR 054/12, 44p.

Mezghani, A., Dobler, A., Haugen, J.E., Benestad, R.E., Parding, K.M., Piniewski, M., Kardel, I., and *Kundzewicz, Z.W.*, 2017: CHASE-PL Climate Projection dataset over Poland – bias adjustment of EURO-CORDEX simulations. *Earth Syst. Sci. Data 9*, 905–925. https://doi.org/10.5194/essd-9-905-2017

Moss, R.H., Edmonds, J.A., Hibbard, K.A., Manning, M.R., Rose, S.K., van Vuuren, D.P., Carter, T.E., Emori, S., Kainuma, M., Kram, T., Meehl, G.A., Mitchell, J.F.B., Nakicenovic, N., Riahi, K., Smith, S.J., Stouffer, R.J., Thomson, A.M., Weyant, J.P., and *Wilbanks, T.J.*, 2010. The next generation of scenarios for climate change research and assessment. *Nature 463*, 747–756. https://doi.org/10.1038/nature08823

Neggers, R.A.J., Köhler, M., and *Beljaars, A.C.M.*, 2009: A dual mass flux framework for boundary layer convection, Part I: Transport. *J. Atmos. Sci. 66*, 1465–1487. https://doi.org/10.1175/2008JAS2635.1

Nordeng, T.E., 1994: Extended versions of the convection parametrization scheme at ECMWF and their impact upon the mean climate and transient activity of the model in the tropics. *ECMWF Tech. Memo. No. 206*.

Pfeifer, S., 2006: Modeling cold cloud processes with the regional climate model REMO. MPI for Meteorology, Hamburg, *Reports on Earth System Science No. 23*.

Rajczak, J., Kotlarski, S., and *Schär, C.*, 2016: Does quantile mapping of simulated precipitation correct for biases in transition probabilities and spell lengths? *J. Climate 29*, 1605–1615. https://doi.org/10.1175/JCLI-D-15-0162.1

Rockel, B., Will, A., and *Hense, A.*, 2008: Special issue: regional climate modeling with COSMO-CLM (CCLM). *Meteorol. Z. 17*, 347–348. https://doi.org/10.1127/0941-2948/2008/0309

Ruti, S.M., Somot, S., Giorgi, F., Dubois, C., Flaounas, E., Obermann, A., Dell'Aquila, A., Pisacane, G., Harzallah, A., Lombardi, E., Ahrens, B., Akhtar, N., Alias, A., Arsouze, T., Aznar, R., Bastin, S., Bartholy, J., Béranger, K., Beuvier, J., Bouffies-Cloché, S., Brauch, J., Cabos, W., Calmanti, S., Calvet, J-C., Carillo, A., Conte, D., Coppola, E., Djurdjevic, V., Drobinski, P., Elizalde-Arellano, A., Gaertner, M., Galàn, P., Gallardo, C., Gualdi, S., Goncalves, M., Jorba, O., Jordà, G., L'Heveder, B., Lebeaupin-Brossier, C., Li, L., Liguori, G., Lionello, P., Maciàs, D., Nabat, P., Önol, B., Raikovic, B., Ramage, K., Sevault, F., Sannino, G., Struglia, M.V., Sanna, A., Torma, Cs., and *Vervatis, V.*, 2016: MED-CORDEX initiative for Mediterranean Climate studies. *Bull. Amer. Meteor. Soc. online*, https://doi.org/10.1175/BAMS-D-14-00176.1

Sillmann, J., Kharin, V.V., Zwiers, F.W., Zhang, X., and *Bronaugh, D.*, 2013: Climate extremes indices in the CMIP5 multimodel ensemble: Part 2. Future climate projections. *J. Geophys. Res. Atmos. 118*, 2473–2493. https://doi.org/10.1002/jgrd.50188

Spinoni, J., Szalai, S., Szentimrey, T., Lakatos, M., Bihari, Z., Nagy, A., Németh, Á., Kovács, T., Mihic, D., Dacic, M., Petrovic, P., Kržic, A., Hiebl, J., Auer, I., Milkovic, J., Štepánek, P., Zahradnícek, P., Kilar, P., Limanowka, D., Pyrc, R., Cheval, S., Birsan, M.-V., Dumitrescu, A., Deak, G., Matei, M., Antolovic, I., Nejedlík, P., Štastn´y, P., Kajaba, P., Bochnícek, O., Galo, D., Mikulová, K., Nabyvanets, Y., Skrynyk, O., Krakovska, S., Gnatiuk, N., Tolasz, R., Antofie, T., and *Vogt, J.*, 2015: Climate of the Carpathian region in the period 1961–2010: Climatologies and trends of 10 variables. *Int. J. Climatol. 35*, 1322–1341. https://doi.org/10.1002/joc.4059

Szalai, S., Auer, I., Hiebl, J., Milkovich, J., Radim, T.. Stepanek, P., Zahradnicek, P., Bihari, Z., Lakatos, M., Szentimrey, T., Limanowka, D., Kilar, P., Cheval, S., Deak, Gy., Mihic, D., Antolovic, I., Mihajlovic, V., Nejedlik, P., Stastny, P., 738 Mikulova, K., Nabyvanets, I., Skyryk, O., Krakovskaya, S.,Vogt, J., Antofie, T., and *Spinoni, J.,* 2013: Climate of the Greater Carpathian Region. Final 740 Technical Report. http://www.carpatclim-eu.org.

Szentimrey, T., and *Bihari, Z.,* 2006: MISH (Meteorological Interpolation based on Surface Homogenized Data Basis). In: (Eds: *O.E.Tveito, M.Wegehenkel, F. van der Wel and H. Dobesch*) COST Action 719 Final Report, The use of GIS in climatology and meteorology, 54-56.

Szentimrey, T., 2007: Manual of homogenization software MASHv3.02. Hungarian Meteorological Service, Budapest. 65p.

Taylor, K.E., 2001: Summarizing multiple aspects of model performance in a single diagram. *J Geophys Res, 106(D7)*, 7183–7192. https://doi.org/10.1029/2000JD900719

Teutschbein, C., and *Seibert, J.,* 2013: Is bias correction of regional model (RCM) simulations possible for non-stationary conditions? *Hydrol. Earth Syst. Sci. 17*, 5061–5077. https://doi.org/10.5194/hess-17-5061-2013

Themeßl, M. J., Gobiet, A., and *Leuprecht, A.,* 2010: Empirical-statistical downscaling and error correction of daily precipitation from regional climate models, *Int. J. Climatol*. *31*, 1530–1544. https://doi.org/10.1002/joc.2168

Tiedtke, M., 1989: A comprehensive mass flux scheme for cumulus parameterization in large-scale models. *Mon. Weather Rev. 117*, 1779–1799. https://doi.org/10.1175/1520-0493(1989)117<1779:ACMFSF>2.0.CO;2

Torma, Cs., Coppola, E., Giorgi, F., Bartholy, J., and *Pongrácz, R.,* 2011: Validation of a high resolution version of the regional climate model RegCM3 over the Carpathian Basin. *J. Hydrometeorol. 12,* 84–100. https://doi.org/10.1175/2010JHM1234.1

Torma, Cs., Giorgi, F., and *Coppola, E.,* 2015: Added value of regional climate modeling over areas characterized by complex terrain-Precipitation over the Alps. *J. Geophys. Res. Atmos*. *120*, 3957–3972. https://doi.org/10.1002/2014JD022781

Voldoire, A., Sanchez-Gomez, E., Salas y Mélia, D., Decharme, B., Cassou, C., Sénési, S., Valcke, S., Beau, I., Alias, A., Chevallier, M., Déqué, M., Deshayes, J., Douville, H., Fernandez, E., Madec, G., Maisonnave, E., Moine, M.-P., Planton, S., Saint-Martin, D., Szopa, S., Tyteca, S., Alkama, R., Belamari, S., Braun, A., Coquart, L., and *Chauvin, F.,* 2012: The CNRM-CM5.1 global climate model: description and basic evaluation. *Clim. Dyn. 40*, 2091–2121. https://doi.org/10.1007/s00382-011-1259-y

Wang, L., Ranasinghe, R., Maskey, S., van Gelder, P.H.A.J.M., and *Vrijling, K.,* 2016: Comparison of empirical statistical methods for downscaling daily climate projections from CMIP5 GCMs: a case study of the Huai River Basin, China. *Int. J. Climatol.* 36, 145–164. https://doi.org/10.1002/joc.4334

Zappa, G., Shaffrey, L.C., Hodges, K.I., Sansom, P.G., and *Stephenson, D.B.,* 2013: A multimodel assessment of future projections of North Atlantic and European extratropical cyclones in the CMIP5 climate models. *J. Climate* 26, 5846–5862. https://doi.org/10.1175/JCLI-D-12-00573.1

Zhao, Z.-C., Luo, Y., and *Huang, J.-B.,* 2013: A review on evaluation methods of climate modeling. *Adv. Clim. Change Res. 4*, 137–144. https://doi.org/10.3724/SP.J.1248.2013.137

DOI:10.28974/idojaras.2020.1.3

IDŐJÁRÁS

Quarterly Journal of the Hungarian Meteorological Service
Vol. 124, No. 1, January – March, 2020, pp. 47–72

Validation of the existing models for estimating diffuse solar radiation over Egypt

S. M. Robaa

Astronomy, Space Sciences and Meteorology Department,
Faculty of Science, Cairo University, Giza - Egypt
Email: d_robaa@hotmail.com

(Manuscript received in final form February 7, 2019)

Abstract— The main objective of this study is to review and test the applicability of well-established models collected from the literature for estimating the monthly average daily diffuse solar radiation on a horizontal surface in Egypt. The different meteorological data measured at eight stations during the period 1987–2016 were used to calculate the monthly mean values of diffuse solar radiation over these stations using the collected models. The selected eight stations measure diffuse solar radiation component and have been chosen to cover the whole of Egypt. The collected models (fourteen models) were compared on the basis of many statistical error tests such as the relative percentage error, (*e%*), mean percentage error (*MPE*), mean bias error (*MBD*), root mean square error (*RMSE*), *t*-test, and Nash-Sutcliffe equation (*NSE*). According to the results, the Tarhan and Sarı model (Model 12) showed the best estimation of the diffuse solar radiation on a horizontal surface for all of the eight stations, and therefore, it is recommended for predicting diffuse solar radiation at any location in Egypt.

Key-words: solar energy, diffuse solar radiation, sunshine duration, extraterrestrial radiation, solar radiation models, model comparison, Egypt.

1. Introduction

Knowledge of local solar radiation components is essential in the design and study of many solar energy applications (*Lu et al,* 1998; *Li* and *Lam,* 2000; *Wong* and *Chow,* 2001; *Driesse* and *Thevenard,* 2002; *Almorox* and *Hontoria,* 2004; *Al-Mohamad,* 2004; *Kumar* and *Umanand,* 2005). Although Egypt is a vast country and has abundant solar energy, solar radiation measurements are not easily

available in Egypt (especially the diffuse solar radiation) because of not being able to afford the measuring equipments and techniques involved (*Ibrahim*, 1985). Therefore, it is important to develop methods to estimate the solar radiation on the basis of the more readily available meteorological data. Several models have been developed to estimate the amount of global solar radiation on horizontal surfaces in Egypt (*Ibrahim*, 1985; *Sabbagh*, 1977; *El-Shahawy*, 1984; *El-Shazly*, 1998; *Trabea* and *Shaltout*, 2000; *Darwish* and *Taha*, 2000; *Tadros*, 2000; *El-Metwally*, 2004 and 2005; *El-Sebaii*, and *Trabea*, 2005; *Khalil* and *Shaffie*, 2013; *El-Metwally* and *Wald*, 2013; *Khalil* and *Shaffie*, 2016). Unfortunately, the diffuse radiation measurements are very rare in Egypt, and there are no researches, except for the study of *El-Sebaii* and *Trabea* (2003), which made a concerning estimation of diffuse solar radiation in Egypt. Therefore, the main objective of this paper is to validate the best available models that predict the monthly mean daily diffuse radiation on a horizontal surface against an independent data set over Egypt, and thus, to select the most accurate model. All the most accurate empirical models which are used to estimate diffuse solar radiation, *D*, have been collected from literatures to evaluate the applicability of these models to estimate *D* over different stations in Egypt. The collected models were compared on the basis of many statistical error tests.

2. Comparison of models with literature

The most accurate empirical models concerning estimation of diffuse solar radiation collected from the literature are as follows:

Model 1 (*Hawas* and *Muneer*, 1984):

$$\frac{D}{H} = 1.35 - 1.6075\left(\frac{H}{H_0}\right), \quad (1)$$

Model 2 (*Ulgen* and *Hepbasli*, 2009):

$$\frac{D}{H_0} = 0.1155 - 0.1958\left(\frac{H}{H_0}\right), \quad (2)$$

Model 3 (*Gopinathan*, 1988):

$$\frac{D}{H} = 0.697 - 0.577\left(\frac{n}{N_o}\right), \quad (3)$$

Model 4 (*Jamil* and *Akhtar*, 2017):

$$\frac{D}{H} = 0.2932 - 1.8655\left(\frac{H}{H_0}\right) - 1.5114\left(\frac{n}{N_o}\right), \quad (4)$$

Model 5 (*Gopinathan*, 1988):

$$\frac{D}{H} = 0.879 - 0.575\left(\frac{H}{H_0}\right) - 0.323\left(\frac{n}{N_o}\right), \quad (5)$$

Model 6 (*El-Sebaii et al.* 2010):

$$\frac{D}{H_0} = 3.0020 - 3.8820\left(\frac{H}{H_0}\right) - 0.1500\left(\frac{n}{N_o}\right), \quad (6)$$

Model 7 (*El-Sebaii* and *Trabea*, 2003):

$$\frac{D}{H} = -0.209 + 2.183\left(\frac{n}{N_o}\right) - 1.785\left(\frac{n}{N_o}\right)^2, \quad (7)$$

Model 8 (*Tarhan* and *Sarı*, 2005):

$$\frac{D}{H} = 0.9885 - 1.4276\left(\frac{H}{H_0}\right) + 0.5679\left(\frac{H}{H_0}\right)^2, \quad (8)$$

Model 9 (*Jamil* and *Akhtar*, 2017):

$$\frac{D}{H} = 0.3116 + 1.8043\left(\frac{H}{H_0}\right) + 0.0501\left(\frac{H}{H_0}\right)^2 - 1.5118\left(\frac{n}{N_o}\right), \quad (9)$$

Model 10 (*Jamil* and *Akhtar*, 2017):

$$\frac{D}{H} = 0.3017 - 1.8726\left(\frac{H}{H_0}\right) - 1.5454\left(\frac{n}{N_o}\right) + 0.0212\left(\frac{n}{N_o}\right)^2, \quad (10)$$

Model 11 (*Jamil* and *Akhtar*, 2017):

$$\frac{D}{H_0} = -0.1776 + 1.6206\left(\frac{H}{H_0}\right) - 0.6843\left(\frac{n}{N_o}\right) - 0.2136\left(\frac{n}{N_o}\right)^2, \quad (11)$$

Model 12 (*Tarhan* and *Sarı*, 2005):

$$\frac{D}{H} = 1.0207 - 1.6582\left(\frac{H}{H_0}\right) + 1.1018\left(\frac{H}{H_0}\right)^2 - 0.4019\left(\frac{H}{H_0}\right)^3, \quad (12)$$

Model 13 (*Aras et al.* 2006):

$$\frac{D}{H} = 1.7111 - 4.9062\left(\frac{H}{H_0}\right) + 6.6711\left(\frac{H}{H_0}\right)^2 - 3.9235\left(\frac{H}{H_0}\right)^3, \quad (13)$$

Model 14 (*Jamil* and *Akhtar*, 2017):

$$\frac{D}{H} = 0.2191 + 2.3964\left(\frac{H}{H_0}\right) - 0.3877\left(\frac{H}{H_0}\right)^2 - 1.7828\left(\frac{n}{N_o}\right) + 0.1705\left(\frac{n}{N_o}\right)^2, \quad (14)$$

where D is the monthly average of the daily diffuse solar radiation, H is the monthly average of the daily global solar radiation, H_o is the monthly average daily extraterrestrial radiation, n is the day length, and N_o is the maximum possible sunshine duration. H_o was calculated from the following equation (*Duffie,* 1991):

$$H_o = \frac{24}{\pi} I_s f (\cos\varphi \cos\delta \sin w + \frac{2\pi}{360} w \sin\varphi \sin\delta), \quad (15)$$

where I_s is the solar constant (=1367Wm^{-2}), f is the eccentricity correction factor of the Earth's orbit, φ is the latitude of the site, δ is the sun declination, and w is the mean sunrise hour angle for the given month. f, δ, w, and N_o can be computed by the following equations (*Duffie,* 1991):

$$f = \left(1 + 0.033 \cos\frac{360n'}{365}\right), \quad (16)$$

$$\delta = 23.45 \sin\left[\frac{360(284 + n')}{365}\right], \quad (17)$$

$$w = \cos^{-1}(-\tan\varphi \tan\delta), \quad (18)$$

$$N_o = 2w/15, \quad (19)$$

where n' is the day of the year.

3. Data and comparison methods

In this study, monthly mean values of global solar radiation and sunshine hours measured at of eight stations during the period 1987–2016 have been obtained from the Egyptian Meteorology Authority (EMA) to calculate the diffuse solar radiation, D over these stations using the above corresponding models. *Table 1* gives the list of the stations and their coordinates in addition to the type of the measured radiation at each station and its date of commencement of records. The monthly mean values of extraterrestrial solar radiation, H_o, and the day length, n, were calculated for each month of the year and for each station using Eqs. (15–19), and they were then employed to estimate D for each station.

Table 1. Coordinates of the Egyptian radiation measurements network and the radiation components measured together with the date of commencement of recording

Station	Latitude (N)	Longitude (E)	Elevation (m)	Measurement				Date of commencement of records*
				G	*D*	*I*	*S*	
Sidi-Barrani	31°38’	25°24’	27	X	X	-	X	1984
Matruh	31°20’	27°13’	38	X	X	-	X	1961 (1981)
El-Arich	31°05’	33°49’	32	X	X	-	X	1980
Tahrir	30°39’	30°42’	16	X	X	-	X	1960 (1981)
Cairo	30°05’	31°17’	36	X	X	X	X	1969 (1974)
Qena	26°03’	32°12’	96	X	X	-	X	1979
El-Kharga	25°27’	30°32’	78	X	X	-	X	1964 (1981)
Aswan	23°58’	32°47’	192	X	X	-	X	1972 (1981)

* The year in brackets indicates the data of commencement of diffuse and/or direct solar radiation records.

G is the global solar radiation; *D* is the diffuse solar radiation, *I* is the direct solar radiation, and *S* is the sunshine duration.

The calculated values of diffuse solar radiation, D_c, were compared with the corresponding mean measured values, D_m (mean of the period 1987–2016) in each model. Moreover, the performance of the models was also evaluated on the basis of the following statistical error tests: relative percentage error (*e*%), mean percentage error (MPE), mean bias error (MBE) root mean square error (RMSE), t-statistic (t), and Nash–Sutcliffe equation (NSE). *e%, MPE, MBE, RMSE, t* and *NSE* are defined by Equations (20–25), respectively, as below (*Tiba*, 2001; *Ulgen* and *Hepbasli*, 2003 and 2004; *Notton et al.* 2004; *Soares et al.* 2004; *Tymvios et al.* 2005; *Mediavilla et al.* 2005; *Ulgen* and *Hepbasli*, 2002; *Togrul* and *Togrul*, 2002; *Stone*, 1993; *Chen et al.*, 2004):

$$e = [(D_{i,m} - D_{i,c}) / D_{i,m}] * 100 \,, \tag{20}$$

$$MPE = \sum_{i=1}^{N} \frac{[(D_{i,m} - D_{i,c}) / D_{i,m}] * 100}{N} \,, \tag{21}$$

$$MBE = \sum_{i=1}^{N} \frac{(D_{i,m} - D_{i,c})}{N} \,, \tag{22}$$

$$RMSE = \left(\frac{\sum_{i=1}^{N} (D_{i,m} - D_{i,c})}{N} \right)^{0.5}, \quad (23)$$

$$t = \left(\frac{(n-1)MBE^2}{RMSE^2 - MBE^2} \right)^{0.5}, \quad (24)$$

$$NSE = 1 - \frac{\sum_{i=1}^{N} (D_{i,m} - D_{i,c})^2}{\sum_{i=1}^{N} (D_{i,m} - \bar{D}_{i,c})^2}, \quad (25)$$

where $D_{i,m}$ and $D_{i,c}$ are the ith measured and calculated values of diffuse solar radiation, respectively, while N is the number of observations taken into account.

4. Results and discussion

The values of monthly mean daily diffuse solar radiation intensity estimated using the above fourteen models (1–14) were compared with the corresponding measured values at the used eight stations. The relative percentage errors, *e(%)*, between the estimated and measured values of the monthly mean daily diffuse solar radiation intensity were determined using Eq. (20) for the 12 months of the year. The statistical tests of *MPE*, *MBE*, *RMSE*, *t-test*, and *NES* were also calculated using Eqs. (21–25), respectively. The results are given in *Tables 2–9*. Furthermore, *Table 10* summarizes the maximum and minimum values of the statistics errors, *MPE*, *MBE*, *RMSE*, *t-test*, and *NSE*, of each fourteen models at the eight selected stations.

It can be seen that the estimated values of D_c at each station are in favorable agreement with the measured values D_m for all the months of the year (*Tables 2–9*), whereas the percentage errors, *e(%)*, for a single month not reaches ±10% for any of the locations. Based on all statistical test results of *MPE*, *MBE*, *RMSE*, *t-test*, and *NES* (*Tables 2–10*), all models are recommended for using to estimate the diffuse radiation at all stations, whereas all statistical test results are in the range of acceptable values between (–0.49 and +5.12) for *MPE*; (-0.39 and +2.78) for *MBE*; (+0.22 and +3.51) for *RMSE*; (+0.03 and +7.96) for *t-test*; and (0.9502 and 0.9999) for *NES*. On the other hand, it was found that the Tarhan and Sarı model, (Model 12), shows the best results among the all models for all of the stations. This is due to the fact that Model (12) has the lowest *MPE*, *MBE*, *RMSE*,

and *t-test* value and highest *NES* values compared to the other fourteen models. It was found that, the overall percentage error, *e%*, of Model (12) is in the range of acceptable values between –5.04 and +3.31% with the lowest mean percentage error (*MPE*) values that range from –0.49% to +0.27%. Furthermore, 95.8% of these values *(e%)* lie between –2.64 and +2.94 for Model (12). Also, the *MBE* values of Model (12) are usually equal to zero or very close to zero, while the values of *t-test* range from +0.03 to 1.88. Furthermore, Model (12) has the highest values of *NES* and closest to 1.0, whereas they range from 0.9956 to 0.9999. These are considered excellent indicators in that the Tarhan and Sarı model (Model 12) gives precise estimation for each station and all Egypt with acceptable errors. Although Model (13) is almost like Model (12), Model (13) has higher values of *MPE, MBE, RMSE*, and *t-test* and lower values of *NES* than of Model (13), (See *Tables 2–9*). Therefore, it can be concluded that the Tarhan and Sarı model (Model 12) is extremely recommended for use to estimate diffuse solar radiation at any location in Egypt, i.e., Model (12) is the best model for estimating diffuse solar radiation on a horizontal surface over Egypt.

Table 2. Monthly mean values (1987–2016) of measured diffuse solar radiation, *Dm* (MJ.m^{-1}) and the corresponding calculated values, *Dc* (MJ.m^{-1}), that estimated using the different fourteen models in addition to the performance statistics errors (*MPE, MBE, RMSE, t-test* and *NSE*) at Sidi-Barrani

Month	***Dm* (1987-2016)**	**Model 1**		**Model 2**		**Model 3**		**Model 4**		**Model 5**		**Model 6**		**Model 7**		**Model 8**		**Model 9**		**Model 10**	
		Dc	*e%*	*Dc*	*e%*	*Dc*	*e%*	*Dc*	*e%*	*Dc*	*e%*	*Dc*	*e%*	*Dc*	*e%*	*Dc*	*e%*	*Dc*	*e%*	*Dc*	*e%*
Jan	**4.89**	4.95	-1.27	4.98	-1.77	4.90	-0.23	4.89	0.02	5.24	-7.07	4.71	3.60	5.22	-6.73	4.95	-1.20	4.77	2.36	4.74	3.10
Feb	**6.05**	6.30	-4.15	6.29	-3.98	6.21	-2.67	6.15	-1.66	6.42	-6.13	6.13	-1.37	6.21	-2.63	6.27	-3.65	6.50	-7.37	6.30	-4.10
Mar	**8.11**	8.11	-0.02	7.91	2.49	7.86	3.04	7.52	7.27	7.78	4.12	7.69	5.21	7.92	2.31	7.94	2.06	8.59	-5.94	7.65	5.68
Apr	**9.75**	9.71	0.43	10.01	-2.68	9.35	4.10	8.91	8.58	9.04	7.28	8.95	8.17	9.15	6.11	9.45	3.12	9.70	0.47	8.91	8.62
May	**9.80**	9.80	0.01	10.05	-2.59	9.49	3.21	9.04	7.71	9.21	5.99	9.11	6.99	9.15	6.68	9.58	2.23	10.13	-3.39	9.08	7.32
Jun	**8.95**	8.90	0.57	8.80	1.71	8.65	3.39	8.31	7.18	8.32	7.09	8.14	9.08	8.45	5.59	8.73	2.41	9.16	-2.38	8.17	8.73
Jul	**9.11**	9.36	-2.71	9.52	-4.51	9.16	-0.50	8.91	2.21	8.80	3.38	8.78	3.64	8.99	1.27	9.24	-1.48	9.27	-1.80	8.58	5.83
Aug	**8.21**	8.37	-1.95	8.48	-3.25	8.21	-0.02	8.05	1.92	7.97	2.88	8.00	2.57	8.24	-0.35	8.29	-0.99	8.40	-2.36	7.78	5.21
Sep	**7.92**	8.05	-1.60	8.15	-2.85	7.89	0.39	7.74	2.32	7.71	2.71	7.69	2.85	7.96	-0.57	7.97	-0.59	8.10	-2.27	7.55	4.72
Oct	**6.38**	6.45	-1.10	6.50	-1.90	6.41	-0.53	6.41	-0.45	6.47	-1.47	6.28	1.57	6.55	-2.73	6.48	-1.50	6.58	-3.14	6.37	0.15
Nov	**5.32**	5.39	-1.39	5.23	1.73	5.34	-0.47	5.35	-0.50	5.49	-3.25	5.37	-0.87	5.49	-3.20	5.40	-1.44	5.62	-5.66	5.41	-1.72
Dec	**4.80**	4.83	-0.64	4.89	-1.94	4.74	1.25	4.65	3.13	5.01	-4.46	4.98	-3.66	4.86	-1.26	4.79	0.27	5.13	-6.88	4.79	0.25
MPE		–	0.59	–	3.24	–	-3.2	–	3.12	–	3.69	–	4.08	–	-2.23	–	0.08	–	-1.02	–	2.18
MBE		–	0.46	–	0.73	–	-0.58	–	0.84	–	0.91	–	0.73	–	0.29	–	0.12	–	0.05	–	0.73
RMS		–	0.98	–	0.85	–	0.71	–	1.63	–	1.54	–	1.58	–	0.78	–	0.46	–	0.79	–	1.34
t-test		–	3.14	–	2.99	–	5.99	–	3.05	–	3.49	–	2.96	–	2.75	–	0.11	–	0.19	–	3.69
NSE		–	0.983	–	0.966	–	0.970	–	0.9514	–	0.9502	–	0.9563	–	0.979	–	0.991	–	0.9812	–	0.970

Table 2. continued

Month	*Dm* (1987-2016)	Model 11		Model 12		Model 13		Model 14	
		Dc	*e*%	*Dc*	*e*%	*Dc*	*e*%	*Dc*	*e*%
Jan	**4.89**	5.03	-2.83	5.02	-2.64	5.29	-8.17	4.88	0.23
Feb	**6.05**	5.68	6.04	6.34	-4.74	6.18	-2.21	6.14	-1.45
Mar	**8.11**	8.40	-3.55	8.00	1.39	8.02	1.08	7.50	7.48
Apr	**9.75**	10.11	-3.74	9.48	2.77	9.19	5.72	8.80	9.79
May	**9.80**	10.16	-3.65	9.59	2.16	9.01	8.05	9.02	7.92
Jun	**8.95**	9.20	-2.77	8.65	3.31	8.61	3.77	8.29	7.39
Jul	**9.11**	9.62	-5.57	9.07	0.46	9.06	0.58	8.89	2.42
Aug	**8.21**	8.56	-4.31	8.15	0.78	8.34	-1.59	8.04	2.13
Sep	**7.92**	8.23	-3.91	7.86	0.73	8.10	-2.30	7.72	2.53
Oct	**6.38**	6.57	-2.96	6.45	-1.08	6.72	-5.34	6.40	-0.24
Nov	**5.32**	5.47	-2.79	5.42	-1.93	5.52	-3.84	5.34	-0.29
Dec	**4.80**	4.94	-3.00	4.85	-1.05	4.66	2.82	4.64	3.34
MPE			-3.98	–	0.07	–	0.12	–	2.35
MBE			-0.88	–	0.00	–	0.23	–	0.82
RMSE			0.89	–	0.33	–	0.54	–	1.23
t-test			7.96	–	0.03	–	0.26	–	2.96
NSE			0.9729	–	**0.9999**	–	0.9899	–	0.9679

Table 3. The same as *Table 2*, but for Matruh

Month	*Dm* (1987-2016)	Model 1		Model 2		Model 3		Model 4		Model 5		Model 6		Model 7		Model 8		Model 9		Model 10	
		Dc	*e%*	*Dc*	*e%*	*Dc*	*e%*	*Dc*	*e%*	*Dc*	*e%*	*Dc*	*e%*	*Dc*	*e%*	*Dc*	*e%*	*Dc*	*e%*	*Dc*	*e%*
Jan	**4.28**	4.29	-0.23	4.33	-1.27	3.98	7.07	4.44	-3.65	4.51	-5.36	4.19	2.05	4.08	4.63	4.11	3.98	4.15	3.14	4.31	-0.70
Feb	**5.91**	5.75	2.67	6.16	-4.15	6.27	-6.13	6.17	-4.40	6.22	-5.27	5.93	-0.37	5.82	1.44	5.94	-0.44	5.96	-0.77	5.97	-1.09
Mar	**8.35**	8.10	3.04	8.35	-0.02	8.01	4.12	8.05	3.58	8.03	3.85	7.92	5.14	8.16	2.23	8.48	-1.50	8.21	1.65	7.95	4.80
Apr	**9.33**	8.95	4.10	9.29	0.43	8.65	7.28	8.80	5.69	8.72	6.49	9.03	3.25	9.14	1.99	9.30	0.34	9.06	2.92	8.82	5.49
May	**10.12**	9.80	3.21	10.12	0.01	9.51	5.99	9.65	4.60	9.58	5.30	9.32	7.93	9.83	2.84	10.34	-2.21	10.1	-0.20	9.94	1.80
Jun	**9.43**	9.11	3.39	9.38	0.57	8.76	7.09	8.94	5.24	8.85	6.16	8.90	5.67	9.19	2.50	9.42	0.16	9.17	2.71	8.93	5.27
Jul	**9.83**	9.88	-0.50	10.10	-2.71	9.50	3.38	9.69	1.44	9.59	2.41	9.68	1.56	9.62	2.18	9.81	0.17	9.56	2.75	9.31	5.34
Aug	**8.72**	8.72	-0.02	8.89	-1.95	8.47	2.88	8.60	1.43	8.53	2.16	8.57	1.67	8.54	2.05	8.70	0.18	8.52	2.27	8.34	4.37
Sep	**7.98**	7.95	0.40	8.11	-1.60	7.76	2.71	7.86	1.55	7.81	2.13	8.03	-0.57	7.90	0.96	8.08	-1.32	7.90	1.02	7.71	3.35
Oct	**6.48**	6.51	-0.53	6.55	-1.10	6.58	-1.47	6.54	-1.00	6.56	-1.23	6.86	-5.88	6.81	-5.14	6.69	-3.25	6.61	-1.98	6.53	-0.71
Nov	**5.22**	5.20	0.47	5.29	-1.39	5.39	-3.25	5.32	-1.86	5.35	-2.55	5.01	4.08	5.07	2.78	5.32	-1.93	5.26	-0.86	5.21	0.21
Dec	**4.46**	4.40	1.25	4.49	-0.64	4.66	-4.46	4.39	1.61	4.32	3.03	4.29	3.74	4.24	4.85	4.35	2.44	4.36	2.18	4.37	1.91
MPE		–	0.98	–	5.12	–	1.84	–	2.93	–	3.95	–	1.28	–	-1.72	–	0.23	–	0.37	–	-1.29
MBE		–	1.63	–	2.78	–	-0.75	–	1.09	–	2.07	–	-0.21	–	1.14	–	-0.25	–	1.32	–	-0.81
RMSE		–	2.06	–	1.96	–	0.96	–	3.51	–	0.13	–	0.59	–	1.19	–	0.51	–	0.65	–	0.98
t-test		–	4.19	–	5.74	–	2.75	–	4.32	–	5.32	–	3.23	–	0.79	–	0.81	–	0.79	–	2.05
NSE		–	0.979	–	0.960	–	0.980	–	0.9588	–	0.9609	–	0.9781	–	0.969	–	0.989	–	0.9748	–	0.977

Table 3. continued

Month	*Dm* (1987-2016)	Model 11		Model 12		Model 13		Model 14	
		Dc	*e*%	*Dc*	*e*%	*Dc*	*e*%	*Dc*	*e*%
Jan	**4.28**	4.23	1.22	4.27	0.26	4.23	1.10	4.19	2.18
Feb	**5.91**	5.96	-0.93	6.03	-2.01	5.95	-0.68	5.96	-0.85
Mar	**8.35**	8.08	3.23	8.77	-5.01	8.28	0.86	8.15	2.44
Apr	**9.33**	8.94	4.20	9.16	1.85	9.12	2.27	9.00	3.56
May	**10.12**	10.04	0.80	9.99	1.30	10.19	-0.70	10.09	0.30
Jun	**9.43**	9.05	3.99	9.37	0.63	9.23	2.07	9.11	3.35
Jul	**9.83**	9.43	4.05	9.71	1.19	9.62	2.11	9.50	3.40
Aug	**8.72**	8.43	3.32	8.65	0.85	8.57	1.75	8.48	2.80
Sep	**7.98**	7.81	2.18	7.76	2.77	7.95	0.43	7.85	1.60
Oct	**6.48**	6.57	-1.34	6.61	-2.03	6.63	-2.30	6.59	-1.66
Nov	**5.22**	5.24	-0.32	5.22	-0.06	5.28	-1.12	5.25	-0.59
Dec	**4.46**	4.37	2.04	4.42	0.98	4.40	1.24	4.37	2.11
MPE		–	2.60	–	0.11	–	0.42	–	2.07
MBE		–	0.79	–	-0.04	–	0.33	–	-0.82
RMSE		–	0.88	–	0.32	–	0.59	–	1.06
t-test		–	3.11	–	0.15	–	0.96	–	2.68
NSE		–	0.9806	–	0.9996	–	0.9889	–	0.9663

Table 4. The same as *Table 2*, but for El-Arish

Month	Dm (1987-2016)	Model 1		Model 2		Model 3		Model 4		Model 5		Model 6		Model 7		Model 8		Model 9		Model 10	
		Dc	*e%*	*Dc*	*e%*	*Dc*	*e%*	*Dc*	*e%*	*Dc*	*e%*	*Dc*	*e%*	*Dc*	*e%*	*Dc*	*e%*	*Dc*	*e%*	*Dc*	*e%*
Jan	**4.88**	4.90	-0.34	4.95	-1.34	4.54	6.90	5.05	-3.38	5.09	-4.34	4.83	0.95	4.62	5.23	4.64	4.87	4.67	4.20	4.87	0.27
Feb	**6.73**	6.56	2.56	7.01	-4.22	7.15	-6.30	7.01	-4.14	7.02	-4.24	6.83	-1.48	6.59	2.04	6.63	1.54	6.71	0.30	6.74	-0.12
Mar	**8.96**	8.70	2.93	8.97	-0.09	8.61	3.95	8.62	3.85	8.52	4.87	8.60	4.03	8.71	2.83	9.10	-1.60	8.72	2.72	8.44	5.77
Apr	**9.79**	9.40	3.99	9.76	0.36	9.09	7.11	9.21	5.96	9.05	7.51	9.58	2.15	9.54	2.59	9.79	0.04	9.40	3.98	9.16	6.46
May	**10.19**	9.87	3.10	10.20	-0.06	9.60	5.82	9.69	4.87	9.55	6.32	9.49	6.83	9.84	3.44	10.37	-1.81	10.1	0.86	9.91	2.77
Jun	**10.01**	9.68	3.28	9.96	0.50	9.32	6.92	9.46	5.50	9.29	7.19	9.55	4.56	9.70	3.10	10.00	0.05	9.63	3.78	9.39	6.24
Jul	**9.52**	9.58	-0.61	9.78	-2.78	9.21	3.21	9.36	1.71	9.19	3.43	9.48	0.45	9.26	2.78	9.51	0.07	9.16	3.82	8.92	6.31
Aug	**9.08**	9.09	-0.13	9.26	-2.02	8.83	2.71	8.93	1.70	8.79	3.18	9.03	0.56	8.84	2.65	9.07	0.06	8.78	3.34	8.60	5.34
Sep	**9.31**	9.28	0.29	9.47	-1.67	9.07	2.54	9.14	1.81	9.02	3.15	9.47	-1.67	9.16	1.56	9.44	-1.42	9.12	2.08	8.91	4.32
Oct	**7.04**	7.08	-0.64	7.12	-1.17	7.16	-1.64	7.09	-0.73	7.05	-0.21	7.53	-6.98	7.36	-4.54	7.28	-1.03	7.10	-0.91	7.02	0.26
Nov	**6.15**	6.13	0.36	6.24	-1.46	6.36	-3.42	6.25	-1.59	6.24	-1.53	5.97	2.97	5.94	3.38	6.21	-3.35	6.14	0.21	6.08	1.18
Dec	**4.81**	4.76	1.14	4.84	-0.71	5.03	-4.63	4.72	1.87	4.61	4.06	4.68	2.64	4.55	5.45	4.66	3.04	4.65	3.24	4.67	2.88
MPE		–	1.05		1.19		1.40		1.99		-2.37		1.37		2.73		0.36		2.13		-2.11
MBE		–	0.82		2.11		1.42		1.37		0.91		1.32		2.27		-0.16		1.19		-0.93
RMSE		–	1.38		2.73		2.64		3.43		1.92		1.65		0.53		0.73		1.53		1.02
t-test		–	1.86		1.76		1.68		1.58		2.35		3.79		4.71		1.01		3.95		4.07
NSE		–	0.977		0.985		0.979		0.9868		0.9731		0.9648		0.960		0.990		0.9726		0.962

Table 4. continued

Month	Dm (1987-2016)	Model 11		Model 12		Model 13		Model 14	
		Dc	*e*%	*Dc*	*e*%	*Dc*	*e*%	*Dc*	*e*%
Jan	**4.88**	4.77	2.18	4.98	-2.03	4.91	-0.71	4.92	-0.87
Feb	**6.73**	6.71	0.24	6.71	0.24	6.73	0.07	6.58	2.16
Mar	**8.96**	8.58	4.29	9.41	-5.04	8.88	0.84	8.74	2.41
Apr	**9.79**	9.37	4.27	9.61	1.82	9.57	2.25	9.44	3.54
May	**10.19**	10.00	1.86	10.06	1.28	10.26	-0.73	10.16	0.27
Jun	**10.01**	9.50	5.06	9.95	0.61	9.80	2.05	9.68	3.33
Jul	**9.52**	9.03	5.11	9.44	0.82	9.48	0.41	9.37	1.58
Aug	**9.08**	8.68	4.39	8.85	2.54	8.89	2.08	8.77	3.38
Sep	**9.31**	9.01	3.25	9.20	1.17	9.15	1.73	9.05	2.77
Oct	**7.04**	7.06	-0.28	7.18	-2.05	7.20	-2.32	7.16	-1.68
Nov	**6.15**	6.10	0.74	6.09	0.95	6.08	1.22	6.02	2.09
Dec	**4.81**	4.66	3.11	4.81	-0.08	4.87	-1.15	4.84	-0.61
MPE		–	2.99	–	-0.08	–	0.31	–	-1.33
MBE		–	1.11	–	0.13	–	0.28	–	-0.91
RMSE		–	1.88	–	0.22	–	0.49	–	0.84
t-test		–	5.78	–	0.19	–	1.03	–	2.45
NSE		–	0.9596	–	0.9997	–	0.9923	–	0.9744

Table 5. The same as *Table 2*, but for Tahrir

Month	*Dm (1987-2016)*	Model 1		Model 2		Model 3		Model 4		Model 5		Model 6		Model 7		Model 8		Model 9		Model 10	
		Dc	*e%*	*Dc*	*e%*	*Dc*	*e%*	*Dc*	*e%*	*Dc*	*e%*	*Dc*	*e%*	*Dc*	*e%*	*Dc*	*e%*	*Dc*	*e%*	*Dc*	*e%*
Jan	**4.79**	4.75	0.84	4.89	-2.09	4.60	3.87	4.99	-4.25	4.87	-1.69	4.64	3.09	4.55	5.05	4.88	-1.88	4.71	1.67	4.73	1.22
Feb	**6.06**	6.01	0.83	6.27	-3.53	6.26	-3.35	6.25	-3.13	6.23	-2.86	6.04	0.28	5.95	1.79	5.99	1.11	5.99	1.23	6.06	0.06
Mar	**8.83**	8.70	1.42	8.77	0.66	8.48	3.95	8.58	2.84	8.44	4.45	8.53	3.43	8.78	0.62	8.72	1.28	8.60	2.57	8.39	5.03
Apr	**9.70**	9.49	2.17	9.82	-1.27	9.01	7.11	9.11	6.06	9.23	4.83	9.47	2.37	9.57	1.31	9.42	2.89	9.34	3.76	9.18	5.36
May	**9.69**	9.54	1.52	9.62	0.73	9.13	5.82	9.22	4.80	9.05	6.57	9.19	5.13	9.61	0.81	9.71	-0.23	9.63	0.57	9.47	2.31
Jun	**9.02**	8.85	1.89	8.91	1.19	8.40	6.92	8.64	4.25	8.49	5.88	8.67	3.83	8.88	1.58	8.78	2.69	8.70	3.55	8.51	5.65
Jul	**8.60**	8.45	1.69	8.79	-2.24	8.32	3.21	8.41	2.21	8.43	1.94	8.46	1.62	8.48	1.43	8.69	-0.99	8.37	2.70	8.11	5.71
Aug	**8.35**	8.26	1.07	8.48	-1.55	8.12	2.71	8.04	3.70	8.19	1.87	8.22	1.61	8.24	1.36	8.12	2.73	8.07	3.36	7.94	4.86
Sep	**8.13**	8.07	0.69	8.23	-1.18	7.92	2.54	7.80	4.00	8.07	0.74	8.13	-0.06	8.12	0.07	7.95	2.25	7.93	2.43	7.82	3.78
Oct	**6.47**	6.41	0.90	6.54	-1.04	6.58	-1.64	6.53	-0.93	6.70	-3.60	6.84	-5.76	6.65	-2.79	6.60	-2.00	6.55	-1.30	6.47	-0.01
Nov	**5.31**	5.28	0.55	5.36	-1.01	5.49	-3.42	5.46	-2.78	5.27	0.72	5.14	3.18	5.31	0.02	5.22	1.65	5.25	1.15	5.26	0.96
Dec	**4.55**	4.54	0.21	4.54	0.25	4.69	-3.13	4.37	3.98	4.40	3.35	4.37	4.05	4.36	4.24	4.59	-0.88	4.49	1.31	4.41	2.99
MPE		–	1.23	–	1.59	–	-0.71	–	1.68	–	0.18	–	0.865	–	2.43	–	-0.88	–	2.56	–	-1.10
MBE		–	1.12	–	1.74	–	1.16	–	1.34	–	1.59	–	0.58	–	1.73	–	-0.54	–	1.15	–	-0.40
RMSE		–	2.01	–	3.08	–	2.28	–	2.54	–	1.23	–	1.19	–	1.03	–	0.88	–	1.705	–	0.62
t-test		–	1.77	–	1.67	–	2.01	–	2.69	–	3.53	–	2.4	–	4.33	–	1.54	–	4.865	–	2.13
NSE		–	0.978	–	0.986	–	0.976	–	0.9758	–	0.9670	–	0.9775	–	0.9667	–	0.998	–	0.9661	–	0.981

Table 5. continued

Month	***Dm (1987-2016)***	**Model 11**		**Model 12**		**Model 13**		**Model 14**	
		Dc	*e%*	*Dc*	*e%*	*Dc*	*e%*	*Dc*	*e%*
Jan	**4.79**	4.79	0.08	4.86	-1.37	4.67	2.54	4.70	1.83
Feb	**6.06**	6.05	0.24	6.05	0.16	6.00	0.92	5.97	1.54
Mar	**8.83**	8.86	-0.37	9.02	-2.10	8.78	0.56	8.70	1.49
Apr	**9.70**	9.40	3.05	9.50	2.04	9.51	2.01	9.43	2.77
May	**9.69**	9.54	1.57	9.66	0.27	9.74	-0.47	9.70	-0.10
Jun	**9.02**	8.76	2.83	8.90	1.33	8.85	1.92	8.78	2.62
Jul	**8.60**	8.34	2.97	8.55	0.62	8.43	1.95	8.45	1.76
Aug	**8.35**	8.06	3.47	8.16	2.31	8.21	1.70	8.14	2.54
Sep	**8.13**	7.95	2.21	8.01	1.45	8.10	0.33	8.00	1.55
Oct	**6.47**	6.55	-1.16	6.61	-2.18	6.57	-0.97	6.56	-1.33
Nov	**5.31**	5.27	0.85	5.25	1.09	5.36	-1.57	5.30	0.26
Dec	**4.55**	4.48	1.51	4.58	-0.61	4.41	3.14	4.49	1.26
MPE		–	0.98	–	-0.49	–	0.98	–	0.55
MBE		–	0.49	–	-0.39	–	-0.83	–	0.41
RMSE		–	0.84	–	0.53	–	1.06	–	0.94
t-test		–	2.22	–	0.32	–	1.79	–	3.39
NSE		–	0.9841	–	0.9993	–	0.9958	–	0.9706

*Table 6.*The same as *Table 2*, but for Cairo

Month	***Dm (1987-2016)***	**Model 1**		**Model 2**		**Model 3**		**Model 4**		**Model 5**		**Model 6**		**Model 7**		**Model 8**		**Model 9**		**Model 10**	
		Dc	*e%*	*Dc*	*e%*	*Dc*	*e%*	*Dc*	*e%*	*Dc*	*e%*	*Dc*	*e%*	*Dc*	*e%*	*Dc*	*e%*	*Dc*	*e%*	*Dc*	*e%*
Jan	**4.50**	4.39	2.35	4.64	-3.17	4.45	1.09	4.53	-0.58	4.42	1.68	4.47	0.60	4.35	3.36	4.51	-0.33	4.46	0.87	4.50	-0.07
Feb	**5.90**	5.97	-1.26	6.10	-3.33	6.08	-3.10	5.98	-1.42	5.93	-0.53	5.86	0.70	5.81	1.51	5.87	0.59	5.86	0.73	5.89	0.11
Mar	**7.60**	7.40	2.68	7.47	1.75	7.28	4.20	7.36	3.14	7.41	2.53	7.42	2.35	7.48	1.59	7.36	3.15	7.52	1.10	7.49	1.47
Apr	**8.30**	7.91	4.64	8.10	2.39	7.80	5.97	7.95	4.21	8.05	3.07	8.08	2.63	8.09	2.54	7.96	4.13	8.02	3.40	7.99	3.70
May	**9.30**	8.96	3.67	9.04	2.76	8.72	6.20	8.84	4.97	8.96	3.69	9.07	2.45	9.24	0.69	9.20	1.04	9.20	1.07	9.18	1.29
Jun	**9.00**	8.60	4.40	8.76	2.72	8.42	6.40	8.64	4.04	8.66	3.73	8.71	3.26	8.77	2.57	8.62	4.17	8.71	3.19	8.69	3.49
Jul	**8.50**	8.29	2.45	8.50	-0.01	8.28	2.57	8.34	1.91	8.36	1.69	8.47	0.31	8.32	2.06	8.30	2.36	8.26	2.83	8.23	3.16
Aug	**8.40**	8.24	1.89	8.31	1.07	8.21	2.29	8.18	2.65	8.26	1.62	8.22	2.17	8.20	2.36	8.08	3.80	8.11	3.41	8.10	3.59
Sep	**8.10**	7.97	1.61	7.99	1.41	7.97	1.64	7.94	1.97	8.07	0.40	8.01	1.10	8.00	1.25	7.86	3.02	7.91	2.32	7.89	2.62
Oct	**6.10**	6.12	-0.37	6.16	-0.99	6.26	-2.62	6.30	-3.35	6.29	-3.19	6.34	-3.88	6.22	-2.04	6.16	-1.01	6.18	-1.23	6.17	-1.10
Nov	**5.60**	5.68	-1.43	5.71	-1.89	5.68	-1.35	5.59	0.20	5.58	0.37	5.46	2.42	5.57	0.58	5.53	1.31	5.54	1.00	5.54	1.02
Dec	**4.60**	4.67	-1.46	4.50	2.12	4.59	0.11	4.42	4.01	4.43	3.80	4.53	1.58	4.47	2.78	4.55	1.06	4.53	1.41	4.55	1.19
MPE		–	1.45	–	0.88	–	0.19	–	2.05	–	-0.35	–	1.71	–	0.67	–	0.05	–	0.93	–	-0.06
MBE		–	1.23	–	1.66	–	0.87	–	1.54	–	0.52	–	0.87	–	0.67	–	-0.03	–	0.38	–	-0.62
RMS		–	2.27	–	2.15	–	1.73	–	1.79	–	1.05	–	1.45	–	0.83	–	0.56	–	1.12	–	0.84
t-test		–	2.23	–	2.60	–	2.21	–	3.51	–	2.53	–	3.63	–	3.23	–	1.88	–	2.59	–	1.96
NSE		–	0.977	–	0.976	–	0.976	–	0.9713	–	0.9828	–	0.9718	–	0.9740	–	0.996	–	0.9827	–	0.988

Table 6. continued

Month	*Dm (1987–2016)*	Model 11		Model 12		Model 13		Model 14	
		Dc	*e%*	*Dc*	*e%*	*Dc*	*e%*	*Dc*	*e%*
Jan	**4.50**	4.44	1.31	4.49	0.23	4.42	1.70	4.43	1.57
Feb	**5.90**	5.87	0.58	5.85	0.85	5.85	0.83	5.84	1.06
Mar	**7.60**	7.59	0.09	7.62	-0.31	7.54	0.83	7.54	0.79
Apr	**8.30**	8.09	2.53	8.10	2.40	8.08	2.71	8.08	2.65
May	**9.30**	9.25	0.55	9.29	0.09	9.27	0.30	9.28	0.22
Jun	**9.00**	8.79	2.37	8.82	1.98	8.77	2.55	8.78	2.50
Jul	**8.50**	8.29	2.46	8.40	1.19	8.30	2.39	8.32	2.11
Aug	**8.40**	8.18	2.58	8.20	2.43	8.19	2.56	8.18	2.56
Sep	**8.10**	8.00	1.27	7.98	1.50	7.99	1.33	7.99	1.41
Oct	**6.10**	6.17	-1.07	6.21	-1.76	6.12	-1.10	6.17	-1.20
Nov	**5.60**	5.62	-0.36	5.56	0.67	5.66	-0.29	5.60	-0.05
Dec	**4.60**	4.49	2.33	4.59	0.32	4.50	2.28	4.52	1.79
MPE		–	0.77	–	-0.04	–	0.16	–	0.74
MBE		–	0.45	–	0.01	–	0.24	–	0.40
RMSE		–	0.89	–	0.33	–	0.68	–	1.03
t-test		–	2.80	–	0.86	–	1.92	–	2.99
NSE		–	0.9774	–	0.9999	–	0.9927	–	0.9766

*Table 7.*The same as *Table 2,* but for El-Kgarga

Month	*Dm (1987-2016)*	Model 1		Model 2		Model 3		Model 4		Model 5		Model 6		Model 7		Model 8		Model 9		Model 10	
		Dc	*e%*	*Dc*	*e%*	*Dc*	*e%*	*Dc*	*e%*	*Dc*	*e%*	*Dc*	*e%*	*Dc*	*e%*	*Dc*	*e%*	*Dc*	*e%*	*Dc*	*e%*
Jan	**4.50**	4.46	0.89	4.53	-0.75	4.46	0.85	4.44	1.39	4.47	0.67	4.47	0.74	4.43	1.64	4.48	0.49	4.48	0.55	4.47	0.75
Feb	**5.44**	5.51	-1.34	5.55	-1.93	5.51	-1.20	5.44	0.04	5.44	0.03	5.40	0.72	5.40	0.81	5.41	0.58	5.40	0.79	5.41	0.58
Mar	**7.42**	7.20	2.91	7.26	2.14	7.18	3.28	7.24	2.36	7.21	2.84	7.29	1.73	7.31	1.53	7.30	1.62	7.39	0.40	7.34	1.13
Apr	**8.29**	7.92	4.43	8.06	2.73	7.93	4.30	8.01	3.37	7.99	3.60	8.04	3.02	8.03	3.12	8.01	3.33	8.05	2.90	8.03	3.17
May	**8.65**	8.28	4.32	8.37	3.23	8.28	4.32	8.41	2.83	8.45	2.37	8.50	1.76	8.56	0.99	8.58	0.80	8.60	0.58	8.58	0.76
Jun	**8.20**	7.85	4.22	7.94	3.22	7.80	4.83	7.93	3.30	7.88	3.95	7.94	3.23	7.95	3.03	7.93	3.27	7.99	2.58	7.95	2.99
Jul	**7.81**	7.64	2.18	7.74	0.84	7.70	1.44	7.65	1.99	7.65	2.02	7.69	1.57	7.61	2.61	7.62	2.41	7.65	2.01	7.60	2.64
Aug	**7.78**	7.60	2.27	7.68	1.34	7.61	2.23	7.59	2.51	7.57	2.71	7.56	2.79	7.55	2.97	7.53	3.19	7.55	2.92	7.54	3.07
Sep	**7.89**	7.75	1.79	7.82	0.91	7.78	1.37	7.76	1.61	7.76	1.71	7.76	1.71	7.74	1.93	7.72	2.14	7.74	1.91	7.73	2.01
Oct	**5.61**	5.71	-1.86	5.73	-2.09	5.79	-3.25	5.76	-2.69	5.73	-2.10	5.75	-2.56	5.70	-1.57	5.67	-1.04	5.69	-1.49	5.67	-1.15
Nov	**4.59**	4.62	-0.62	4.63	-0.76	4.57	0.53	4.57	0.39	4.55	0.84	4.51	1.71	4.55	0.80	4.57	0.47	4.55	0.83	4.57	0.48
Dec	**4.20**	4.15	1.28	4.08	2.96	4.16	0.85	4.06	3.40	4.10	2.43	4.14	1.50	4.12	1.98	4.13	1.69	4.16	0.87	4.14	1.49
MPE		–	1.75	–	0.41	–	0.95	–	1.36	–	-0.15	–	1.32	–	0.52	–	0.27	–	0.43	–	0.34
MBE		–	1.38	–	1.09	–	0.87	–	1.10	–	0.43	–	0.62	–	0.02	–	0.21	–	0.49	–	-0.11
RMS		–	2.03	–	1.60	–	1.59	–	1.31	–	0.95	–	1.28	–	0.83	–	0.72	–	0.87	–	0.93
t-test		–	2.87	–	2.57	–	2.92	–	3.37	–	2.21	–	3.11	–	2.59	–	1.72	–	2.24	–	2.37
NSE		–	0.974	–	0.979	–	0.974	–	0.9727	–	0.9895	–	0.9772	–	0.9813	–	0.991	–	0.9889	–	0.982

Table 7. continued

Month	*Dm (1987-2016)*	Model 11		Model 12		Model 13		Model 14	
		Dc	*e%*	*Dc*	*e%*	*Dc*	*e%*	*Dc*	*e%*
Jan	**4.50**	4.43	1.51	4.48	0.36	4.45	1.13	4.45	1.16
Feb	**5.44**	5.40	0.70	5.40	0.71	5.40	0.81	5.40	0.82
Mar	**7.42**	7.39	0.46	7.37	0.66	7.37	0.61	7.35	0.96
Apr	**8.29**	8.07	2.62	8.05	2.87	8.06	2.80	8.05	2.91
May	**8.65**	8.61	0.42	8.61	0.44	8.61	0.44	8.61	0.49
Jun	**8.20**	8.00	2.46	7.98	2.62	7.99	2.57	7.97	2.75
Jul	**7.81**	7.62	2.42	7.67	1.80	7.64	2.20	7.62	2.37
Aug	**7.78**	7.58	2.57	7.56	2.81	7.57	2.74	7.56	2.82
Sep	**7.89**	7.79	1.30	7.75	1.82	7.76	1.62	7.75	1.71
Oct	**5.61**	5.67	-1.08	5.69	-1.40	5.59	-1.30	5.68	-1.17
Nov	**4.59**	4.60	-0.32	4.56	0.57	4.65	0.27	4.58	0.22
Dec	**4.20**	4.10	2.30	4.16	1.01	4.13	1.57	4.13	1.64
MPE		–	0.69	–	0.13	–	0.32	–	0.54
MBE		–	0.53	–	0.11	–	0.37	–	0.14
RMSE		–	0.98	–	0.58	–	0.90	–	0.98
t-test		–	3.06	–	1.60	–	1.98	–	2.73
NSE		–	0.9850	–	0.9956	–	0.9897	–	0.9796

Table 8. The same as *Table 2,* but for Qena

Month	*Dm (1987-2016)*	Model 1		Model 2		Model 3		Model 4		Model 5		Model 6		Model 7		Model 8		Model 9		Model 10	
		Dc	*e%*	*Dc*	*e%*	*Dc*	*e%*	*Dc*	*e%*	*Dc*	*e%*	*Dc*	*e%*	*Dc*	*e%*	*Dc*	*e%*	*Dc*	*e%*	*Dc*	*e%*
Jan	**4.53**	4.48	1.14	4.52	0.32	4.50	0.76	4.46	1.52	4.51	0.58	4.50	0.64	4.48	1.10	4.51	0.42	4.49	1.03	4.47	1.32
Feb	**4.79**	4.82	-0.65	4.83	-0.94	4.82	-0.59	4.77	0.43	4.77	0.30	4.75	0.75	4.75	0.80	4.76	0.65	4.75	0.75	4.75	0.76
Mar	**6.41**	6.24	2.64	6.26	2.25	6.21	3.06	6.28	1.95	6.27	2.23	6.34	1.06	6.35	0.96	6.34	1.14	6.38	0.43	6.37	0.54
Apr	**7.16**	6.88	3.90	6.94	3.05	6.87	3.95	6.92	3.25	6.91	3.46	6.94	2.96	6.94	3.01	6.93	3.10	6.96	2.76	6.96	2.71
May	**8.73**	8.42	3.57	8.46	3.03	8.44	3.35	8.56	1.91	8.59	1.58	8.63	1.17	8.66	0.79	8.67	0.62	8.69	0.50	8.69	0.43
Jun	**8.38**	8.06	3.76	8.10	3.26	8.01	4.39	8.11	3.17	8.07	3.61	8.13	2.91	8.14	2.81	8.13	2.95	8.17	2.52	8.17	2.52
Jul	**6.91**	6.77	2.09	6.82	1.41	6.79	1.73	6.75	2.30	6.76	2.21	6.79	1.79	6.75	2.31	6.77	2.10	6.76	2.22	6.75	2.31
Aug	**6.31**	6.16	2.39	6.18	1.93	6.15	2.47	6.13	2.74	6.12	2.95	6.13	2.85	6.12	2.95	6.12	3.00	6.13	2.74	6.14	2.65
Sep	**6.80**	6.68	1.70	6.71	1.26	6.69	1.54	6.68	1.77	6.67	1.93	6.67	1.81	6.67	1.92	6.66	1.98	6.69	1.60	6.70	1.46
Oct	**5.17**	5.29	-2.28	5.29	-2.39	5.31	-2.67	5.28	-2.13	5.25	-1.57	5.27	-2.03	5.25	-1.53	5.23	-1.22	5.23	-1.29	5.23	-1.19
Nov	**4.67**	4.67	-0.11	4.68	-0.19	4.64	0.68	4.64	0.60	4.64	0.65	4.61	1.27	4.63	0.82	4.64	0.52	4.66	0.25	4.67	-0.03
Dec	**4.16**	4.06	2.34	4.02	3.18	4.09	1.64	4.05	2.69	4.07	2.06	4.11	1.18	4.10	1.43	4.10	1.35	4.09	1.59	4.08	1.94
MPE		–	1.56	–	0.81	–	0.40	–	0.83	–	0.13	–	0.87	–	0.37	–	0.29	–	0.56	–	0.60
MBE		–	1.24	–	1.10	–	0.56	–	0.56	–	0.23	–	0.41	–	0.11	–	0.16	–	0.34	–	0.43
RMS		–	1.67	–	1.45	–	1.27	–	1.07	–	0.91	–	1.00	–	0.78	–	0.73	–	0.85	–	0.94
t-test		–	3.12	–	2.97	–	2.56	–	2.98	–	2.27	–	2.42	–	2.16	–	1.97	–	2.39	–	2.79
NSE		–	0.973	–	0.976	–	0.981	–	0.9770	–	0.9804	–	0.9843	–	0.9863	–	0.993	–	0.9881	–	0.9874

Table 8. continued

Month	*Dm (1987-2016)*	Model 11		Model 12		Model 13		Model 14	
		Dc	*e%*	*Dc*	*e%*	*Dc*	*e%*	*Dc*	*e%*
Jan	**4.53**	4.50	0.76	4.50	0.73	4.48	1.22	4.49	0.90
Feb	**4.79**	4.75	0.77	4.75	0.76	4.75	0.78	4.75	0.79
Mar	**6.41**	6.36	0.81	6.36	0.81	6.37	0.57	6.34	1.01
Apr	**7.16**	6.95	2.89	6.95	2.94	6.96	2.76	6.95	2.94
May	**8.73**	8.69	0.47	8.68	0.61	8.69	0.43	8.66	0.83
Jun	**8.38**	8.15	2.68	8.15	2.71	8.16	2.54	8.14	2.83
Jul	**6.91**	6.77	2.09	6.77	2.05	6.76	2.26	6.77	2.08
Aug	**6.31**	6.13	2.81	6.12	2.88	6.14	2.70	6.13	2.84
Sep	**6.80**	6.68	1.77	6.67	1.87	6.69	1.54	6.68	1.76
Oct	**5.17**	5.23	-1.28	5.24	-1.46	5.16	-1.24	5.25	-1.60
Nov	**4.67**	4.65	0.39	4.64	0.69	4.73	0.12	4.63	0.74
Dec	**4.16**	4.10	1.33	4.11	1.22	4.08	1.75	4.10	1.41
MPE		–	0.35	–	0.27	–	0.56	–	0.71
MBE		–	0.13	–	0.11	–	0.40	–	0.28
RMSE		–	0.78	–	0.68	–	0.92	–	0.99
t-test		–	2.17	–	1.88	–	2.65	–	2.58
NSE		–	0.9876	–	0.9987	–	0.9896	–	0.9819

Table 9. The same as *Table 2*, but for Aswan

Month	*Dm (1987-2016)*	Model 1		Model 2		Model 3		Model 4		Model 5		Model 6		Model 7		Model 8		Model 9		Model 10	
		Dc	*e%*	*Dc*	*e%*	*Dc*	*e%*	*Dc*	*e%*	*Dc*	*e%*	*Dc*	*e%*	*Dc*	*e%*	*Dc*	*e%*	*Dc*	*e%*	*Dc*	*e%*
Jan	**4.78**	4.73	0.95	4.76	0.45	4.75	0.67	4.72	1.31	4.74	0.84	4.74	0.84	4.74	0.93	4.74	0.87	4.74	0.89	4.73	1.02
Feb	**5.64**	5.67	-0.62	5.66	-0.32	5.65	-0.14	5.61	0.61	5.61	0.55	5.60	0.75	5.60	0.78	5.60	0.70	5.60	0.76	5.60	0.76
Mar	**7.20**	6.99	2.85	7.04	2.24	7.01	2.65	7.10	1.45	7.09	1.60	7.15	0.74	7.14	0.88	7.14	0.84	7.16	0.62	7.15	0.67
Apr	**7.96**	7.65	3.92	7.70	3.26	7.66	3.71	7.71	3.13	7.70	3.24	7.73	2.86	7.73	2.95	7.73	2.90	7.74	2.82	7.74	2.82
May	**8.61**	8.31	3.46	8.41	2.31	8.40	2.46	8.49	1.35	8.51	1.18	8.54	0.83	8.56	0.63	8.56	0.52	8.57	0.48	8.57	0.52
Jun	**8.90**	8.54	4.08	8.59	3.44	8.54	4.00	8.63	2.99	8.61	3.21	8.66	2.72	8.66	2.75	8.66	2.73	8.67	2.60	8.67	2.62
Jul	**8.11**	7.96	1.91	7.96	1.81	7.95	1.97	7.92	2.31	7.93	2.26	7.95	2.00	7.93	2.20	7.93	2.21	7.94	2.15	7.93	2.18
Aug	**8.12**	7.92	2.43	7.92	2.44	7.90	2.71	7.89	2.84	7.88	2.95	7.89	2.80	7.89	2.88	7.89	2.83	7.89	2.78	7.90	2.77
Sep	**7.67**	7.55	1.62	7.55	1.59	7.54	1.73	7.53	1.85	7.52	1.92	7.54	1.71	7.53	1.84	7.54	1.72	7.54	1.69	7.54	1.66
Oct	**6.21**	6.36	-2.48	6.33	-1.98	6.34	-2.12	6.32	-1.83	6.31	-1.55	6.31	-1.66	6.30	-1.41	6.28	-1.20	6.29	-1.29	6.29	-1.33
Nov	**5.33**	5.31	0.29	5.32	0.23	5.29	0.67	5.29	0.71	5.29	0.74	5.29	0.76	5.30	0.61	5.32	0.25	5.31	0.32	5.31	0.33
Dec	**4.41**	4.32	1.99	4.29	2.62	4.33	1.85	4.32	2.06	4.33	1.74	4.35	1.38	4.35	1.38	4.34	1.64	4.35	1.46	4.34	1.58
MPE		–	0.98	–	0.47	–	0.27	–	0.60	–	0.25	–	0.71	–	0.36	–	0.94	–	0.45	–	0.43
MBE		–	0.90	–	0.66	–	0.39	–	0.34	–	0.17	–	0.38	–	0.12	–	0.23	–	0.24	–	0.27
RMS		–	1.47	–	1.18	–	1.09	–	0.92	–	0.84	–	0.93	–	0.78	–	0.83	–	0.82	–	0.81
t-test		–	2.84	–	2.62	–	2.42	–	2.57	–	2.22	–	2.40	–	2.16	–	1.81	–	2.28	–	2.33
NSE		–	0.983	–	0.978	–	0.981	–	0.9816	–	0.9834	–	0.9862	–	0.9870	–	0.996	–	0.9879	–	0.993

Table 9. continued

Month	*Dm (1987–2016)*	Model 11		Model 12		Model 13		Model 14	
		Dc	*e%*	*Dc*	*e%*	*Dc*	*e%*	*Dc*	*e%*
Jan	**4.78**	4.74	0.83	4.74	0.92	4.74	0.84	4.73	1.10
Feb	**5.64**	5.60	0.78	5.60	0.78	5.63	0.23	5.60	0.70
Mar	**7.20**	7.13	0.91	7.13	0.95	7.10	1.41	7.11	1.23
Apr	**7.96**	7.73	2.91	7.73	2.94	7.72	3.01	7.72	3.03
May	**8.61**	8.55	0.65	8.55	0.73	8.49	1.37	8.52	1.09
Jun	**8.90**	8.65	2.76	8.65	2.79	8.63	2.99	8.64	2.91
Jul	**8.11**	7.94	2.08	7.94	2.14	7.95	2.03	7.93	2.19
Aug	**8.12**	7.89	2.82	7.89	2.86	7.91	2.57	7.89	2.84
Sep	**7.67**	7.53	1.76	7.53	1.80	7.55	1.57	7.53	1.80
Oct	**6.21**	6.30	-1.44	6.30	-1.50	6.20	-1.61	6.32	-1.72
Nov	**5.33**	5.30	0.57	5.29	0.67	5.42	0.18	5.29	0.73
Dec	**4.41**	4.35	1.37	4.35	1.39	4.31	2.19	4.33	1.74
MPE		–	0.53	–	0.33	–	0.52	–	0.65
MBE		–	0.20	–	0.20	–	0.53	–	0.31
RMSE		–	0.89	–	0.47	–	1.05	–	0.96
t-test		–	2.37	–	1.37	–	2.64	–	2.57
NSE		–	0.9848	–	0.9994	–	0.9900	–	0.9818

Table10. Summary of maximum and minimum values of the statistical error tests, *MPE, MBE, RMSE, t-test,* and *NSE* of the fourteen models at the nine stations

Station	Value/ (Model Number)	*MPE*		*MBE*		*RMSE*		*t-test*		*NES*	
		Farthest from 0	Closest to 0	Farthest from 0	Closest to 0	Farthest from 0	Closest to 0	Farthest from 0	Closest to 0	Farthest from 1	Closest to 1
Sidi-Barrani	value	4.08	0.07	0.91	0.00	1.63	0.33	7.96	0.03	0.9502	0.9999
	(Model No.)	(6)	**(12)**	(5)	**(12)**	(4)	**(12)**	(11)	**(12)**	(5)	**(12)**
Matruh	value	5.12	0.11	2.78	-0.04	3.51	0.32	5.74	0.15	0.9588	0.9996
	(Model No.)	(2)	**(12)**	(2)	**(12)**	(4)	**(12)**	(2)	**(12)**	(4)	**(12)**
El-Arish	value	2.99	-0.08	2.27	0.13	3.43	0.22	5.78	0.19	0.9596	0.9997
	(Model No.)	(11)	**(12)**	(7)	**(12)**	(4)	**(12)**	(11)	**(12)**	(11)	**(12)**
Tahrir	value	2.56	-0.49	1.74	-0.39	3.08	0.53	4.87	0.32	0.9661	0.9993
	(Model No.)	(9)	**(12)**	(2)	**(12)**	(2)	**(12)**	(9)	**(12)**	(9)	**(12)**
Cairo	value	2.05	-0.04	1.66	0.01	2.27	0.33	3.63	0.86	0.9713	0.9999
	(Model No.)	(4)	**(12)**	(2)	**(12)**	(1)	**(12)**	(6)	**(12)**	(4)	**(12)**
El-Kharga	value	1.75	0.13	1.38	0.11	2.03	0.58	3.37	1.60	0.9727	0.9956
	(Model No.)	(1)	**(12)**	(1)	**(12)**	(1)	**(12)**	(4)	**(12)**	(4)	**(12)**
Qena	value	1.56	0.27	1.24	0.11	1.76	0.68	3.12	1.88	0.9734	0.9987
	(Model No.)	(1)	**(12)**	(1)	**(12)**	(1)	**(12)**	(1)	**(12)**	(1)	**(12)**
Aswan	value	0.98	0.12	0.90	0.12	1.47	0.47	2.84	1.37	0.9783	0.9994
	(Model No.)	(1)	**(12)**	(1)	**(12)**	(1)	**(12)**	(1)	**(12)**	(1)	**(12)**

5. Conclusions

The most accurate empirical models that estimate diffuse solar radiation were collected from the literature to evaluate their applicability for estimate diffuse solar radiation over Egypt. The collected models were compared on the basis of the many statistical error tests; relative percentage error *(e%)*, mean percentage error (*MPE*), mean bias error (*MBD*), root mean square error (*RMSE*), *t-test*, and Nash-Sutcliffe equation (*NSE*). According to the results, the Tarhan and Sarı model (Model 12) showed the best estimation of the diffuse solar radiation on a horizontal surface for all stations. Therefore, the Tarhan and Sarı model (Model 12) is extremely recommended for predicting diffuse solar radiation at any location in Egypt.

References

Al-Mohamad A., 2004: Global, direct and diffuse solar radiation in Syria. *Appl Energy 79 (2)*, 191–200. https://doi.org/10.1016/j.apenergy.2003.12.011

Almorox, J., and *Hontoria C.*, 2004: Global solar radiation estimation using sunshine duration in Spain. *Energy Conv. Manage 45*, 1529–35. https://doi.org/10.1016/j.enconman.2003.08.022

Aras, H., Balli, O., Hepbasli, A., 2006: Estimating the horizontal diffuse solar radiation over the Central Anatolia region of Turkey. *Energy Conv. Manage 47*, 2240–2249. https://doi.org/10.1016/j.enconman.2005.11.024

Chen, R., Ersi, K., Yang, J., Lu, S., Zhao, W., 2004: Validation of five global radiation models with measured daily data in China. *Energy Conv. Manage 45*, 1759–69. https://doi.org/10.1016/j.enconman.2003.09.019

Darwish, M. A., and *Taha, N. E.*, 2000: Estimation of diffuse radiation over the Arab World (Eastern Region). 5th conference-Meteorology &Sustainable development 22-24 February 2000. Cairo, Egypt.

Driesse, A. and *Thevenard, D. A.*, 2002: Test of Suehrcke's sunshine radiation relationship using a global data set. *Sol. Energy 72*, 167–75. https://doi.org/10.1016/S0038-092X(01)00082-2

Duffie, J. A. and *Beckman, W. A.*, 1991: Solar engineering of thermal process. New York: Wiley.

El-Metwally, M., 2004: Simple new methods to estimate global solar radiation based on meteorological data in Egypt. *Atmos. Res. 69*, 217–239. https://doi.org/10.1016/j.atmosres.2003.09.002

El-Metwally, M., 2005: Sunshine and global solar radiation estimation at different sites in Egypt. *J. Atmos. Solar –Terr. Phys. 67*, 1331–1342. https://doi.org/10.1016/j.jastp.2005.04.004 https://doi.org/10.1080/01431161.2013.834393

El-Metwally, M. and Wald, L., 2013: Monthly means of daily solar irradiation over Egypt estimated from satellite database and various empirical formulae. *Int. J. Remote Sens. 34*, 8182–8198. https://doi.org/10.1080/01431161.2013.834393

El-Sebaii, A.A., and *Trabea, A.A.*, 2003: Estimation of horizontal diffuse solar radiation in Egypt. *Energy Conv. Manage. 44*, 2471–2482. https://doi.org/10.1016/S0196-8904(03)00004-9

El-Sebaii, A.A., and *Trabea, A.A.*, 2005: Estimation of Global Solar Radiation on Horizontal Surfaces over Egypt. *Egypt. J. Solids. 28*, 163–175.

El-Sebaii, A.A., Al-Hazmi, F. S., Al-Ghamdi, A.A., Yaghmour, S.J., 2010: Global, direct and diffuse solar radiation on horizontal and tilted surfaces in Jeddah, Saudi Arabia. *Appl. Energy 87*, 568–76. https://doi.org/10.1016/j.apenergy.2009.06.032

El-Shahawy, M.A., 1984: Estimation of daily global solar radiation. *Bull. Fac. Sci. Cairo Univ. 52*, 641–653.

El-Shazly, M.S., Abdelmageed, A.M. and *El-Noubi, M.*, 1998: Solar radiation characteristics at Qena/ Egypt. *Mausam 49*, 59–70.

Gopinathan, K.K., 1988: Empirical correlations for diffuse solar radiation. *Sol Energy 40*, 369–70. https://doi.org/10.1016/0038-092X(88)90009-6

Hawas, M.M. and *Muneer, T.*, 1984: Study of diffuse and global radiation characteristic in India. *Energy Conv. Manage 24*, 143–9. https://doi.org/10.1016/0196-8904(84)90026-8

Ibrahim, S.M.A., 1985: Predicted and measured global solar radiation in Egypt. *Sol Energy 35*, 185–8. https://doi.org/10.1016/0038-092X(85)90009-X

Jamil, B. and *Akhtar, N.*, 2017: Comparative analysis of diffuse solar radiation models based on sky clearness index and sunshine period for humid-subtropical climatic region of India: A case study. *Renew. Sustain. Energy Rev. 78*, 329–355. https://doi.org/10.1016/j.rser.2017.04.073

Khalil, S.A., and *Shaffie, A. M.*, 2013: A comparative study of total, direct and diffuse solar irradiance by using different models on horizontal and inclined surfaces for Cairo, Egypt. *Renew. Sustain. Energy Rev. 27*, 853–63. https://doi.org/10.1016/j.rser.2013.06.038

Khalil, S.A., and *Shaffie, A.M.*, 2016: Evaluation of transposition models of solar irradiance over Egypt. *Renew. Sustain. Energy Rev. 66*, 105–119. https://doi.org/10.1016/j.rser.2016.06.066

Kumar, R. and *Umanand, L.*, 2005: Estimation of global radiation using clearness index model for sizing photovoltaic system. *Renew Energy 30*, 2221–2233. https://doi.org/10.1016/j.renene.2005.02.009

Li, D.H.W. and *Lam, J.C.*, 2000: Solar heat gain factors and the implications for building designs in subtropical regions. *Energy Build. 32*, 47–55. https://doi.org/10.1016/S0378-7788(99)00035-3

Lu, Z., Piedrahita R.H., and *Neto, C.D.S.*, 1998: Generation of daily and hourly solar radiation values for modeling water quality in aquaculture ponds. *Trans ASAE 41*, 1853–1859. https://doi.org/10.13031/2013.17323

Mediavilla, M.D., Miguel, A., and *Bilbao, J.*, 2005: Measurement and comparison of diffuse solar irradiance models on inclined surfaces in Valladolid, Spain. *Energy Conv. Manage 46*, 2075–92. https://doi.org/10.1016/j.enconman.2004.10.023

Notton, G., Cristofari, C., and *Muselli, M., Poggi, P.*, 2004: Calculation on an hourly basis of solar diffuse irradiations from global data for horizontal surfaces in Ajaccio. *Energy Conv. Manage 45*, 2849–2866. https://doi.org/10.1016/j.enconman.2004.01.003

Sabbagh, J.A., Sayigh, A.M., El Salam, E.M., 1977: Estimation of the total radiation from meteorological data. *Solar Energy 19*, 307–311. https://doi.org/10.1016/0038-092X(77)90075-5

Soares, J., Oliveira, A. P., Boznar, M. Z., Mlakar, P., Escobedo, J. F., and *Machado, A.J.*, 2004: Modeling hourly diffuse solar radiation in the city of Sao Paulo using a neural network technique. *Appl. Energy 79*, 201–214. https://doi.org/10.1016/j.apenergy.2003.11.004

Stone, R.J., 1993: Improved statistical procedure for the evaluation of solar radiation models. *Sol Energy 51*, 289–91. https://doi.org/10.1016/0038-092X(93)90124-7

Tadros, M.T.Y., 2000: Uses of Sunshine Duration to Estimate the Global Solar Radiation over Eight Meteorological Stations in Egypt. *Renew. Energy 21*, 231–246. https://doi.org/10.1016/S0960-1481(00)00009-4

Tarhan, S. and *Sarı, A.*, 2005: Model selection for global and diffuse radiation over the Central Black Sea (CBS) region of Turkey. *Energy Conv. Manage 46*, 605–613. https://doi.org/10.1016/j.enconman.2004.04.004

Tiba, C., 2001: Solar radiation in the Brazilian Northeast. *Renew. Energy 22*, 565–578. https://doi.org/10.1016/S0960-1481(00)00116-6

Togrul, I.T., and *Togrul, H.*, 2002: Global solar radiation over Turkey: comparison of predicted and measured data. *Renew. Energy 25*, 55–67. https://doi.org/10.1016/S0960-1481(00)00197-X

Trabea, A., and *Shaltout, M.A.*, 2000: Correlation of Global Solar Radiation with Meteorological Parameters over Egypt. *Renew. Energy 21*, 297–308. https://doi.org/10.1016/S0960-1481(99)00127-5

Tymvios, F.S., Jacovides, C.P., Michaelides, S.C., and *Scouteli, C.*, 2005: Comparative study of Angstrom and artificial neural networks methodologies in estimating global solar radiation. *Sol Energy 78*, 752–62. https://doi.org/10.1016/j.solener.2004.09.007

Ulgen, K., and *Hepbasli, A.*, 2002: Comparison of solar radiation correlations for Izmir, Turkey. *Int. J. Energy Res. 26*, 413–430. https://doi.org/10.1002/er.794

Ulgen, K., and *Hepbasli, A.*, 2003: Comparison of diffuse fraction of daily and monthly global radiation for Izmir, Turkey. *Energy Sour. 25*, 637–649. https://doi.org/10.1080/00908310390212444

Ulgen, K., and *Hepbasli, A.*, 2004: Solar radiation models. Part 2: Comparison and developing new models. *Energy Sour. 26*, 521–530. https://doi.org/10.1080/00908310490429704

Ulgen, K., and *Hepbasli, A.*, 2009: Diffuse solar radiation estimation models for Turkey's big cities. *Energy Conv. Manage 50*, 149–56. https://doi.org/10.1016/j.enconman.2008.08.013

Wong, L.T., and *Chow, W.K.*, 2001: Solar radiation model. *Appl. Energy 69*,191–224. https://doi.org/10.1016/S0306-2619(01)00012-5

DOI:10.28974/idojaras.2020.1.4

IDŐJÁRÁS

Quarterly Journal of the Hungarian Meteorological Service
Vol. 124, No. 1, January – March, 2020, pp. 73–95

Spatial distribution of the daily, monthly, and annual precipitation concentration indices in the Lake Urmia basin, Iran

Yousef Ramezani[*], **Abbas Khashei-Siuki**, and **Mohammad Nazeri Tahroudi**

Department of Water Engineering,
University of Birjand, Birjand, Iran

**Corresponding Author e-mail: y.ramezani@birjand.ac.ir*

(Manuscript received in final form February 4, 2019)

Abstract— Investigations of the long-term observations of climate variables, as a practical approach to monitor climate changes, have attracted the interest of many researchers around the world. One of the important variables in this context is precipitation. The investigation of precipitation, one of the most important meteorological factors directly affecting accessibility to water resources, is of special importance. In every region, studies of precipitation on daily, monthly, or annual scales provide important information on the distribution, concentration, and dispersion of precipitation, as well as some conclusions about the associated hydrological problems. In this study, the precipitation concentration was calculated and zoned by means of the precipitation concentration index (*PCI*) in the basin of Lake Urmia, using monthly and annual rainfall data of 42 selected rain gauge stations, from which 24 stations located in the West Azerbaijan province (in the west of Lake Urmia) and 18 stations located in the East Azerbaijan province (in the east of Lake Urmia) during 1984–2013. The results of the studies of the precipitation concentration index over the basin of Lake Urmia showed that the dominant concentrations of spring, autumn, and winter precipitation were moderate, indicating a moderate distribution for the precipitation of the months in these seasons. In addition, in the period under study, uniform and regular precipitation concentrations (*PCI*<10) were observed only in winter and in the borders of the basin. In summer, almost the entire surface of the basin (excluding its northeastern part) faced a strongly irregular distribution of precipitation, indicating irregular rainfall in July, August, and September. Most of the basin of Lake Urmia is covered by an irregular distribution of precipitation on an annual scale. By investigating the precipitation distribution in the first and the last 10 years of the statistical period considered and by comparing them, it was revealed that the greatest increase in the precipitation concentration index was in autumn, it rose by approximately 20.55 percent. According to the results, on the basin scale, the concentration index showed that the daily rainfall of the Lake Urmia basin was neither in regular nor in strongly irregular conditions at any of the stations studied. All the stations studied were in fairly regular, moderate

concentration and fairly irregular conditions of daily precipitation distribution. The results also showed that the moderate concentration includes most of the daily precipitation distributions throughout the basin.

Key-words: precipitation pattern, precipitation concentration, Lake Urmia, meteorological drought, Lorenz curve.

1. Introduction

In the present era, climate change is one of the most important environmental challenges. Understanding the human impacts on the environment, particularly those related to the warming caused by the increase in greenhouse gases, reveals that a number of parameters are being changed. According to scientific reports, the average surface air temperature has increased by 0.6 oC during the 20th century, where an upward trend is also expected for the evaporation rate. Hence, the atmosphere will be able to transfer more water vapor, and so, the precipitation rate will consequently be affected (*Tabari et al.*, 2011). Under the influence of global warming, rainfall patterns have changed, and extreme weather events like floods, droughts, rains, storms, and so on have occurred as a result. For instance, a significant reduction in the number of rainy days was confirmed in many parts of the world, including China (*Gong and Ho*, 2002; *Ren et al.*, 2000; *Zhai et al.*, 2005; *Zhang et al.*, 2008). One of the most important aspects of climate change, which needs to be studied more accurately, is the investigation of temporal distribution of precipitation and its historical changes. Therefore, it seems necessary to employ indices to express the changes caused by the effects of precipitation on water resources like groundwater, surface water, and snow reserves. Some prominent indices are the standardized precipitation index (SPI), precipitation concentration index (PCI), and concentration index (CI). Low amounts of precipitation and severe fluctuations on daily, seasonal, and annual scales are the inherent characteristics of Iran's climate.

The precipitation concentration index (*PCI*) is a strong indicator of the temporal distribution of precipitation, which is commonly used on annual scales. The increase in the value of this index means that precipitation has a minor distribution in the region. The *PCI* is also an evaluator to determine the precipitation changes in a specific region, and its analytical results demonstrates the availability of water in an environment. Information about the outcome can be used in management programs. Changes in the intensity, duration, time, and amount of precipitation are major indicatives of climate change. These changes can be assessed by the concentration index. The concentration index (*CI*) and the corresponding concentration curve are actually used to measure the quantity inequality of a parameter of a particular variable. For example, in statistics, this index can be used to determine better health subsidies for the poor in different countries. It is also possible to use this index to study precipitation distribution in a basin or a country, or in any other field of science. The concentration index is

defined by a concentration curve (Lorenz curve). In this curve, the *x* axis is the cumulative percentage of samples, which is ranked by specified values, and the *y* axis in the curve is the cumulative percentage of the multiplication of the midpoint of clusters by the number of observations in each cluster. In fact, the Lorenz curve is a concept utilized in economic theories to assess the spatiotemporal changes in time series of daily precipitation and precipitation concentration. The Lorenz curve provides a graphical representation of the cumulative percentage of the total annual precipitation. In addition, in this curve, data are extracted using the Gini coefficient and the Lorenz asymmetry coefficient so as to measure the precipitation concentration parameter.

To illustrate the performance of the two indices in examining the spatiotemporal changes, a practical example is given with real data in the following. In fact, the concentration index (CI) is an index used to evaluate the statistical properties of daily precipitation. PCI is a part of the well-known Fournier index, which has a strong background in the analysis of natural systems like soil erosion (*De Luis et al.,* 2011). The results obtained from calculating PCI could be employed in managerial programs of hydrologic, water, and environmental resources as a tool for early warning when faced with floods or erosion (*Adegun et al.,* 2012). This concept can also be used in planning irrigation and designing modern systems. Unbalanced distribution of precipitation could reduce crop yield by reducing the stored moisture in the ground and by increasing the number of irrigation periods. In addition to this, an unbalanced distribution of precipitation means more drought, and it is possible that even rainfalls with less than the average amount of precipitation in an area may cause severe floods. This is because the soil moisture is decreased, as a result of which vegetation is devastated. Finally, it increases the protective measures in the basin in order to maintain the water structures.

Martin-Vide (2004) calculated the concentration index for daily precipitation in Peninsular Spain and divided the region into two regions with the highest distribution and regular distribution. *Zhang et al.* (2009) calculated the concentration index for the precipitation series of the Pearl River basin (*Zhang et al.,* 2009). *Alijani et al.* (2008) examined the rainfall intensity of Iran at 90 synoptic stations, and showed that the precipitation distribution throughout Iran is irregular, and that the Caspian border stations, Zagros mountain chains, and the northwest part of the country have the most significant contributions of precipitation and are subject to severe rainfalls (*Alijani et al.,* 2008). *Li et al.* (2011) calculated CI values for the Kaidu River basin (*Li et al.,* 2011). *De Luis et al.* (2011) studied the amount of annual, seasonal, and humid and dry periods of PCI adjacent to Spain for two periods (1976–2005 and 1964–1975). The analyses of two sub-periods revealed that the significant changes in precipitation in Spain occurred between 1964 and 2005. *Adegun et al.* (2012) have evaluated PCI on seasonal and annual scales since 1974 through 2011 for two regions in Nigeria. The results of PCI for the region showed that 87 and 71 percent of the examined

years fell within the first and second limits of the moderate concentration range, respectively. *Cortesi et al.* (2012) examined the daily precipitation concentration in different regions of Europe (*Cortesi et al.*, 2012). *Shi et al.* (2013) studied the daily precipitation concentration in the Lankang River basin using the concentration index, and concluded that the results of this indicator are able to improve the water resources management of the river (*Shi et al.*, 2013). *Valli et al.* (2013) used PCI, in a part of their study, to show the rainfall patterns in the state of Andhra Pradesh from 1981 to 2010 at two annual and seasonal scales. The results indicated that there was an irregular precipitation distribution (with values ranging from 16 to 35) in the region (*Valli et al.*, 2013). *Khalili et al.* (2016) investigated the distribution of monthly and annual precipitation at synoptic stations of Iran during the last half century in two 25-year periods. Scientists believe that changes in the concentration of greenhouse gases, resulting from the consumption of fossil fuels, have led to drastic changes in some certain components of the hydrological cycle, including precipitation in different parts of the world; wherein Lake Urmia is not excluded from these changes and has faced critical conditions in recent years. According to the statistics provided by the relevant organizations, it is seen that there is no significant changes in the amounts of precipitation over the basin; it seems that the temporal distribution of precipitation, as well as the rainfall pattern, have changed in recent years. Hence, the aim of the present study is to investigate the changes in the pattern and distribution of daily, monthly, and annual precipitation at rain gauge stations in the basin of Lake Urmia from 1984 to 2013.

2. Materials and methods

2.1. Study area

Lake Urmia is the accumulation center of surface runoff surplus to the demand of the rivers within the enclosed basin of Lake Urmia. With an area of approximately 5,750 square kilometers and an average altitude of 1,276 meters above mean sea level, this lake is located in the middle of the northern basin. The Lake Urmia basin is located in the northwest part of Iran. There are 16 wetlands with areas ranging from five to 120 hectares (some of which have dried up), mostly containing fresh or fresh and saline water, and possess high value as ecosystems. The Lake Urmia basin is situated within the eastern longitudes from 14–44 to 47–53 and northern latitudes of 35–40 and 30–38. In the basin of Lake Urmia, precipitation changes from 220 to 900 mm and the mean rainfall is 263 mm, whereas the precipitation increases from the central parts of the basin towards the surrounding highlands. In this study, daily, monthly, and annual rainfall data from the rain gauge stations located in the basin of the lake have been used from 2013 to 1984, a period of 30 years. The positions of Lake Urmia and the rain gauge

stations studied in the basin are illustrated in *Fig. 1*, and the attributes of the rain gauge stations are presented in *Table 1*.

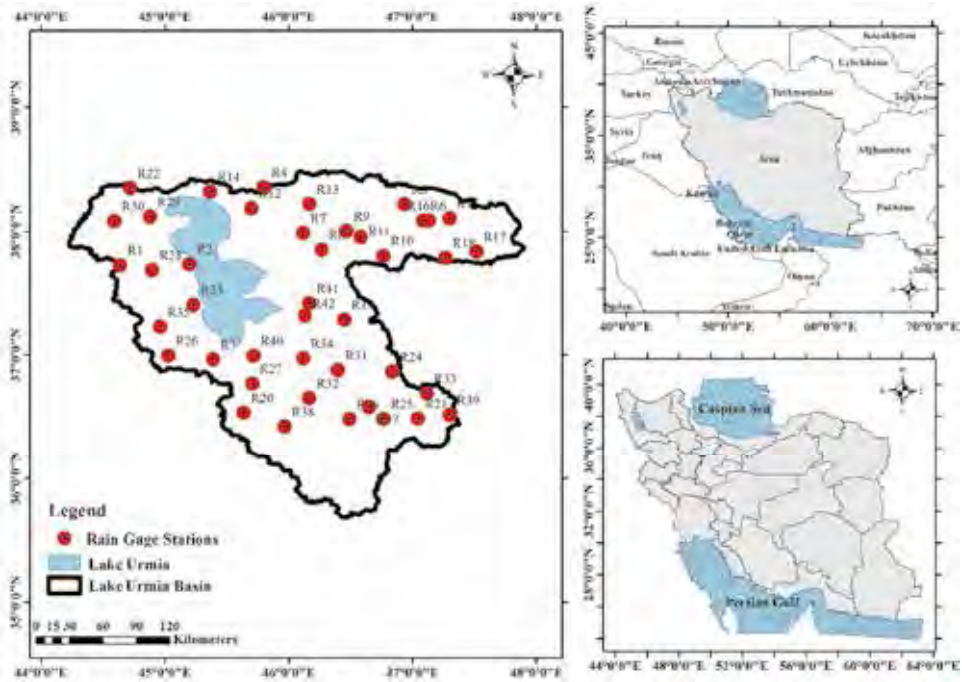

Fig. 1. Location map of the selected stations in the Lake Urmia basin.

Table. 1. Statistical properties of rain gauge stations located in the Lake Urmia basin in the period from 1984 to 2013

Station Number	Station	Elevation (m)	Longitude	Latitude	Annual Precipitation (mm/y)
1	Agchekol	1710	46.45	37.28	424.0
2	Bashsizojan	1850	46.77	37.80	352.6
3	Basmanj	1700	46.47	38.00	172.0
4	Ghezelche	1844	47.30	38.10	339.5
5	Ghoshchi	1980	47.27	37.78	768.3
6	Haris	1690	47.52	37.83	463.7
7	Khoshehmehr	1320	46.13	37.32	309.0
8	Khormazard	1556	46.17	37.42	398.3
9	Mehraban	1608	47.13	38.08	327.2
10	Pardel	1415	46.17	38.22	238.1
11	Payam	1790	45.80	38.35	457.7
12	Saeedabad	1950	46.58	37.95	381.3
13	Saray	1545	46.93	38.22	287.6
14	Isfahlan	1400	46.12	37.98	272.6
15	Shabestar	1400	45.70	38.18	297.4
16	Tasoj	1390	47.08	38.08	372.5
17	Zarnaq	1600	45.37	38.32	297.7
17	Zenjanab	2110	46.27	37.85	332.9
19	Afan	1620	45.64	36.53	578.8
20	Alasagel	1700	47.04	36.49	392.7
21	Babarood	1282	45.23	37.40	342.8
22	Badamloo	2119	46.84	36.86	638.4
23	Bagch	1898	46.77	36.48	348.3
24	Chehreq	1611	44.59	38.08	366.3
25	Chobchole	1361	46.40	36.88	306.3
26	Dashband	1318	46.17	36.65	397.3
27	Gerdeyaghob	1280	45.72	37.00	268.7
28	Ghezel Gonbad	1374	45.97	36.42	402.5
29	Ghezel-Ghaber	1657	46.65	36.58	322.6
30	Ghoshkhana	2260	47.30	36.51	379.8
31	Moshabad	1281	45.20	37.73	248.4
32	Naqade	1306	45.39	36.96	323.2
33	Pey Ghala	1306	45.03	36.99	486.1
34	Pole sorkhe	1350	45.71	36.77	35.0
35	Sari Ghamesh	1391	46.49	36.48	322.5
36	Sero	1628	44.64	37.72	360.8
37	Tamar	1387	44.88	38.11	212.6
38	Tapik	1398	44.90	37.68	368.6
39	Urban	1840	44.72	38.35	310.0
40	Zarineh	1390	46.12	36.97	422.5
41	Zereshoran	2100	47.12	36.69	427.6
42	Zharabad	1569	44.96	37.23	542.3

2.2. Concentration index (CI)

CI is a concentration index that is used to assess the daily concentration and the statistical structure of precipitation. The daily statistical structure of precipitation can be depicted by precipitation concentration curves, which are related to cumulative precipitation percentages to the cumulative percentage of days with rainfall. The concentration index (CI) is a curve that defines the contrast or concentration of different amounts of daily precipitation. The method of calculating the concentration index (CI) is based on the principle that the overall proportion of days with rainfall to the total precipitation is adjustable by a negative exponential distribution (*Brooks and Carruthers*, 1953; *Martin-Vide*, 2004). Considering the geographical characteristics and the temporal period, the possibility of a small amount of daily precipitation would be more than large quantities of precipitation. So, starting with the classification from the lowest class, the absolute eventuate frequency will be decreased (*Martin-Vide*, 2004). To investigate the effects of different amounts of daily rainfall and to determine the share of the high values of precipitation to the entire rainfall, the cumulative rainfall percentage (Y) and the cumulative percentage of days (X) were studied during Y events. Based on the studies of (*Martin-Vide*, 2004; *Olascoaga*, 1950; *Riehl*, 1949), in order to investigate the concentration index (CI), first of all, the daily precipitation data are classified in 1 mm/day clusters. The number of days with specified rainfall is determined in each cluster, and its cumulative value is calculated as well.

Finally, the cumulative percentage of rainy days and the amount of precipitation associated with the rainy days are obtained. According to the aforementioned stages, an exponential curve of the cumulative percentages of rainy days (X) versus the cumulative rainfall percentage (*Y*) is achieved. *Martin-Vide* (2004) recommended the $Y = (a \times X)\exp(\mathrm{b} \times X)$ model for this curve, where *a* and *b* are the regression coefficients.

The Gini concentration index ($Gini = 2S / 10000$) is employed as a concentration measuring index, where *S* equals the area enclosed by the first quarter bisector and a polygon line or Lorenz curve. In fact, the precipitation concentration is based on the *Gini* coefficient. The Lorenz curve is depicted by $Y = (a \times X)\exp(\mathrm{b} \times X)$ model, where coefficients *a* and *b* are calculated by the least squares method (*Martin-Vide*, 2004). After determining coefficients *a* and *b*, the definite integral of the exponential curve between 0 and 100 illustrates the area under curve or *A*′:

$$A' = \left[\frac{a}{b} e^{bX} \left(X - \frac{1}{b} \right) \right]_0^{100} \cdot \qquad ((1)$$

Based on this equation, the area enclosed by the curve and the distribution line of X = 100 between 5000 and the value calculated by Eq.(2) are different (*Martin Vide,* 2004; *Zamani et al.,* 2018). From these precipitation concentrations, which are similar to the *Gini* coefficient, it can be found that:

$$CI = S'/5000. \tag{2}$$

Therefore, the value of *CI* is a fraction of the amount of *S'* and the triangle area formed at the bottom of the chart. Coefficients *a* and *b* can be obtained by the following equation:

$$\ln a = \frac{\sum X_i^2 \sum \ln Y_i + \sum X_i \sum X_i \ln X_i - \sum X_i \sum \ln X_i - \sum X_i \sum X_i \ln Y_i}{n\sum X_i^2 - (\sum X_i)^2}, \tag{3}$$

$$b = \frac{n\sum X_i \ln Y_i + \sum X_i \sum \ln X_i - n\sum X_i \ln X_i - \sum X_i \sum \ln Y_i}{n\sum X_i^2 - (\sum X_i)^2}. \tag{4}$$

In Eqs. (3) and (4), X and Y values are described in detail in *Table 3*. The flowchart of the proposed methodology is demonstrated in *Fig. 2*.

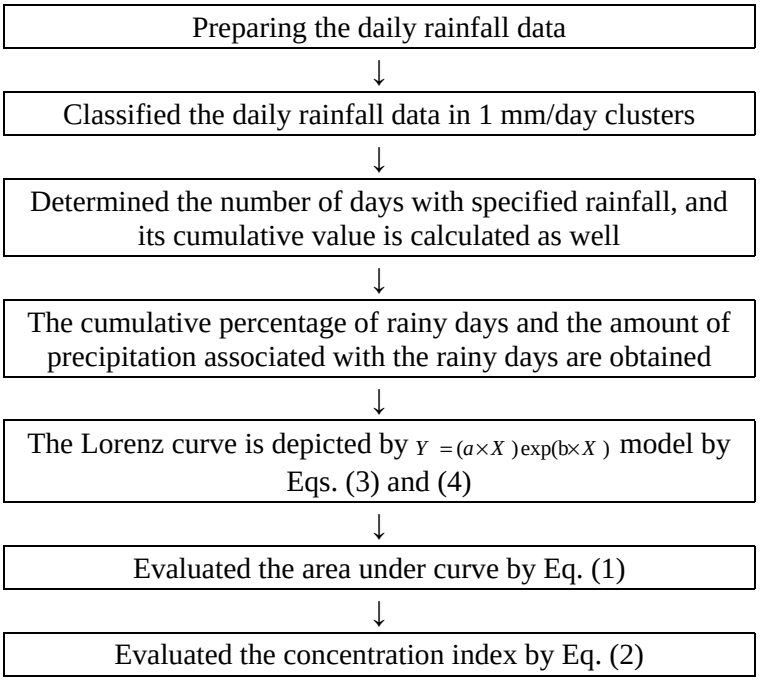

Fig. 2. Flowchart of the proposed *CI* methodology

2.3. Precipitation concentration index (PCI)

The *PCI* is an indicator used to determine the precipitation changes of a specific region, and its analytical results demonstrates the water availability in an environment. The *PCI* is recommended as a measure of the precipitation concentration and distribution. The seasonal and annual scales of this index are calculated by Eqs. (5) and (6) (*Oliver*, 1980), respectively:

$$PCI_{Seasonal} = \frac{\sum_{i=1}^{3} p_i^2}{(\sum_{i=1}^{3} p_i)^2} * 25, \quad (5)$$

$$PCI_{Annual} = \frac{\sum_{i=1}^{12} p_i^2}{(\sum_{i=1}^{12} p_i)^2} * 100, \quad (6)$$

where P_i is the amount of monthly precipitation for the *i*th month. The number 3 in Eq. (5) indicates the number of months in a season. On the basis of the suggested formula and the initial results of *Oliver* (1980), the minimum theoretical value of *PCI* is 8.3, indicating a complete uniformity in precipitation distribution (which means that the same amount of precipitation occurs in each month). A *PCI* equals to 16.7 shows that the total rainfall is concentrated in the half of the temporal interval, and a value of 25 for this index indicates that the total precipitation received has occurred in one-third of the temporal interval (this means that the total rainfall occurs in four months). *Oliver* (1980) – according to the preliminary results of his studies – suggested that a *PCI* less than 10 shows a uniform distribution of rainfall (low concentration of precipitation). *PCI* values from 11 to 15 represent average precipitation concentration, and values between 16 and 20 reflect the irregular distribution of precipitation. Based on the classification of *Oliver* (1980), a *PCI* greater than 20 is indicative of a great chaotic distribution of precipitation (strong precipitation concentration) (*De Luis et al.*, 2011).

Results of applying this index in the various climates of the world such as Spain, Nigeria, and India showed that *PCI* index can be useful in investigating precipitation concentration distribution (*Adegun et al.*, 2012; *De Luis et al.*, 2011; *Tahroudi et al.*, 2019; *Valli et al.*, 2013; *Zamani et al.*, 2018; *Khozeymehnezhad, and Tahroudi, 2019*).

3. Results and discussion

3.1. The results of the concentration index in Lake Urmia basin

The statistical analysis of daily, monthly, and annual precipitation data of enclosed basins such as Lake Urmia basin is climatically important from the distribution point of view. Hence, the investigation of an index, which is able to show distributions and concentrations, can be very valuable. The *PCI* is calculated at annual and seasonal scales by using the data of monthly and annual precipitation from the selected rain gauge stations over the basin of Lake Urmia in the period from 1984 to 2013 along with Eqs. (5) and (6). The mean results are presented in *Table 2.*

Table 2. Results of calculation of the *PCI* index in rain gauge stations located in the Lake Urmia basin

Station Number	Station	Latitude	Longitude	Spring	Summer	Autumn	Winter	Annual
1	Agchekol	37.28	46.45	11.86	20.02	12.13	9.88	15.29
2	Bashsizojan	37.80	46.77	11.67	17.06	12.71	9.79	14.98
3	Basmanj	38.00	46.47	11.05	16.84	12.43	10.17	14.95
4	Ghezelche	38.10	47.30	11.51	17.81	11.13	10.83	15.88
5	Ghoshchi	37.78	47.27	11.39	19.70	11.77	9.32	15.29
6	Haris	37.83	47.52	11.60	16.64	13.17	10.22	16.91
7	Khoshehmehr	37.32	46.13	12.79	23.21	12.96	10.57	17.41
8	Khormazard	37.42	46.17	12.72	21.53	13.18	10.31	17.11
9	Mehraban	38.08	47.13	11.87	16.75	11.9	10.70	16.90
10	Pardel	38.22	46.17	11.19	18.76	12.15	11.1	15.60
11	Payam	38.35	45.80	10.92	18.67	11.59	10.21	15.44
12	Saeedabad	37.95	46.58	11.96	17.29	13.95	10.29	16.97
13	Saray	38.22	46.93	11.41	17.49	12.46	10.06	14.87
14	Isfahlan	37.98	46.12	11.75	20.09	12.61	10.67	17.07
15	Shabestar	38.18	45.70	12.25	20.30	12.38	10.4	17.36
17	Tasoj	38.08	47.08	11.24	15.13	12.37	10.52	15.50
17	Zarnaq	38.32	45.37	12.08	17.72	13.3	11.08	17.60
18	Zenjanab	37.85	46.27	10.68	19.16	13.04	10.28	15.99
19	Afan	36.53	45.64	13.61	22.05	13.03	9.60	17.08
20	Alasagel	36.49	47.04	12.92	21.65	14.31	9.46	16.06
21	Babarood	37.40	45.23	13.36	21.49	13.82	10.84	17.38
22	Badamloo	36.86	46.84	12.30	21.99	11.49	9.3	15.57
23	Bagch	36.48	46.77	12.64	23.71	13.79	10.17	18.13
24	Chehreq	38.08	44.59	10.38	14.85	12.34	10.45	14.23
25	Chobchole	36.88	46.40	14.24	25.00	12.36	10.61	18.54
26	Dashband	36.65	46.17	13.51	23.25	13.52	10.2	18.12
27	Gerdeyaghob	37.00	45.72	13.3	22.06	13.61	10.76	19.69
28	Ghezel Gonbad	36.42	45.97	14.82	23.79	14.51	10.28	18.61

Table 2. Continued

Station Number	Station	Latitude	Longitude	Spring	Summer	Autumn	Winter	Annual
29	Ghezel-Ghaber	36.58	46.65	13.58	23.03	13.97	9.66	16.97
30	Ghoshkhana	36.51	47.30	13.26	22.95	12.85	9.48	16.86
31	Mosh Abad	37.73	45.20	12.53	21.18	13.79	11.58	18.54
32	Naqade	36.96	45.39	12.96	21.15	12.66	10.55	16.99
33	Pey Ghala	36.99	45.03	13.62	21.00	12.00	9.63	15.89
34	Pole sorkhe	36.77	45.71	12.82	21.53	13.01	10.47	17.81
35	Sari Ghamesh	36.48	46.49	12.96	21.15	12.66	10.55	16.99
36	Sero	37.72	44.64	11.46	17.30	11.95	10.74	15.95
37	Tamar	38.11	44.88	12.18	21.06	15.12	12.77	19.08
38	Tapik	37.68	44.90	12.97	20.21	14.81	11.40	18.33
39	Urban	38.35	44.72	11.40	18.05	12.33	13.27	17.52
40	Zarrine	36.97	46.12	13.12	20.95	13.1	10.15	17.44
41	Zereh Shoran	36.69	47.12	12.21	21.75	14.88	9.35	16.93
42	Zhar Abad	36.58	46.65	13.65	20.65	13.34	10.56	16.75

The results of studying the precipitation concentration of Lake Urmia showed that on an annual scale over the basin, there is no regular concentration at the rain gauge stations studied (*PCI* <10). On an annual scale, Stations 4, 3, 2, 18, 11, 22, and 24 are of moderate concentration and distribution of precipitation. Also, on this scale, rain gauge Stations 1, 10, 8, 19, 20, 21, 23, 25, 28, 29, 34, 36, 40, 41, and 42 have irregular distribution of monthly precipitation in more than 50 percent of the studied years, which means that the distribution of precipitation is irregular in 12 months in the studied years. Strongly irregular distribution was also observed on this scale at Tepik (38), Moshabad (31), Gerdeyaghob (27), and Dashband (26) stations.

In spring, there is at least one regular precipitation concentration (*PCI*<10) on the seasonal scale over the basin and through the years studied. In spring, at all the stations surveyed, 50 percent of the years that were investigated have moderate precipitation concentration and distribution. Meanwhile, Stations 22 and 41 experienced an almost uniform precipitation distribution in spring; also, on this scale, Stations 37 and 39 were of the highest number of years with irregular precipitation concentration. This means that in the years studied, the distribution of precipitation was irregular in three months of each year. A strongly irregular distribution of precipitation on this scale was evident in one to three years of the years studied at Stations 2, 12, and 7 in the east of Lake Urmia and at Stations 42,

41, 40, 39, 38, 35, 33, 32, 31, 30, 29, 28, 27, 26, 25, 23, 21, 20, and 19 in the western part of the basin. The results suggested an increase in the precipitation irregularity at the western stations compared to the eastern stations over the last 30 years. On the seasonal scale and in summer, throughout the basin during the years studied, no regular precipitation concentrations were observed. In summer, the prevailing concentration of the stations was classified as strongly irregular. Meanwhile, the number of stations to the west of Lake Urmia was higher in percentage terms, and their concentrations were more irregular than the stations to the east of the lake. Stations located in the eastern part of the lake in this season (summer) were of relatively less moderate and irregular precipitation concentrations. The results showed that in summer, the precipitation in the different months of this season is distributed in an extremely irregular manner. On a seasonal scale and in autumn, through the basin and over the years studied, a regular concentration of precipitation was seen in a few years at each station. In autumn, the prevailing concentration of precipitation was in two categories of moderate and irregular concentrations at the stations studied. In the meantime, as in summer, the stations in the western part of the lake were more in percentage terms and had more irregular concentrations than the stations in the eastern part of the basin.

The extremely irregular concentration of precipitation was observed in one to three years at most of the stations. No strongly irregular precipitation concentration was observed on a seasonal scale and in winter over the basin in the years studied. In winter, the prevailing precipitation concentration of the stations studied were within either moderate or regular concentration categories. In winter, the precipitation distribution was more regular in January, February, and March than in the other months of the year. To investigate the distribution of the precipitation concentration index in the basin of Lake Urmia, the results of the studies of the index were zoned in the region on two seasonal and annual scales, and are presented in *Fig. 3*.

As it is obvious from *Fig. 3*, in spring, small regions to the northwest and northeast of Lake Urmia have regular concentrations and distributions. There is also a small region that is irregularly concentrated in terms of precipitation distribution in the southwestern part of the Lake Urmia basin.

Finally, it is clear, that most parts of the lake basin have moderate concentration and distribution of precipitation in spring. Precipitation around the lake in this season and in April, May, and June is in the moderate distribution category in terms of the distributions of the months. In summer, the prevailing concentration of rain gauge stations is strongly irregular in the basin of Lake Urmia.

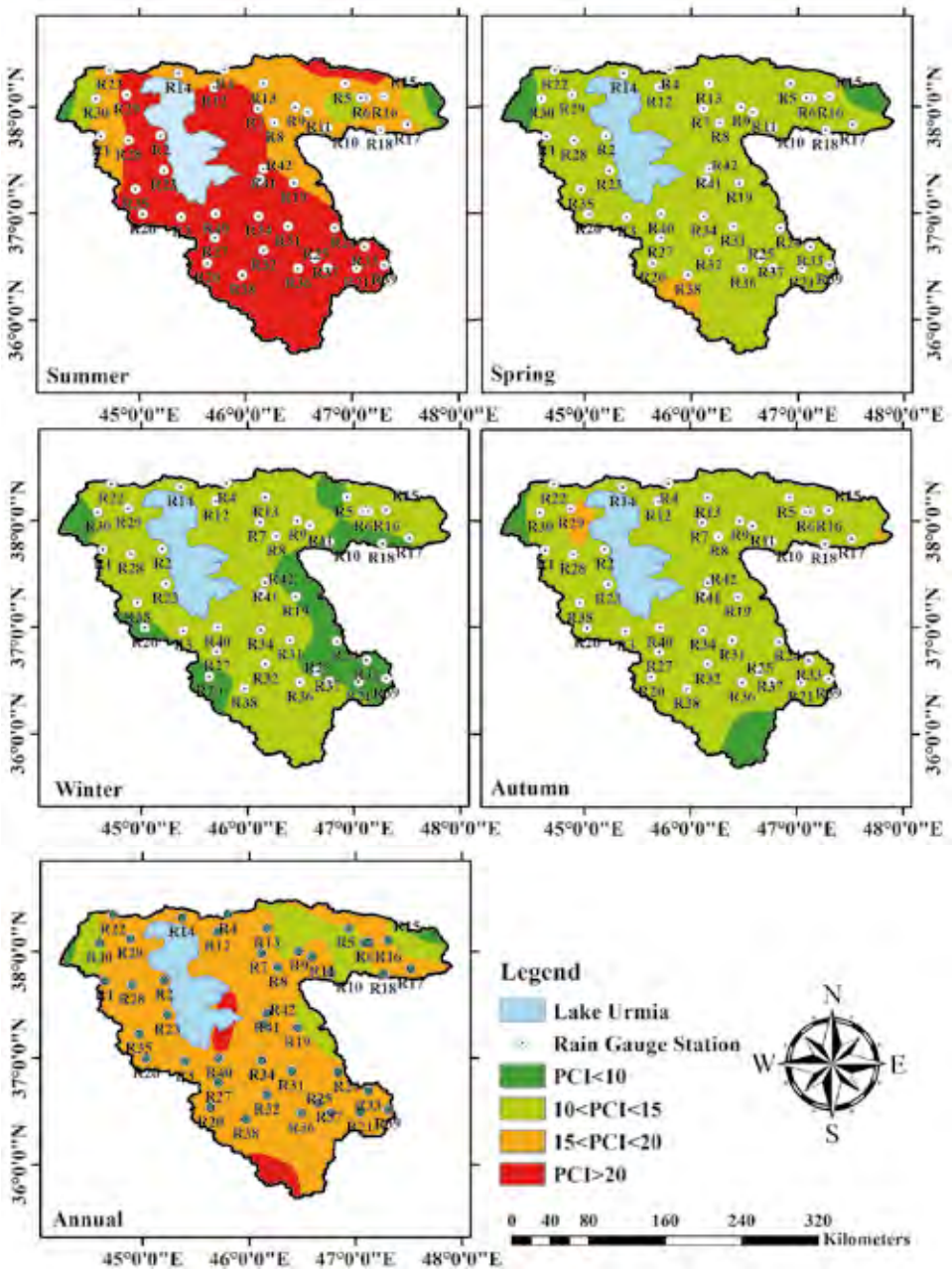

Fig. 3. Spatial distribution of *PCI* in annual and seasonal time scales in the period of 1984–2013.

As it can be seen in *Fig. 3*, the surroundings of the lake and the southern parts of the basin possess strongly irregular distribution of precipitation. The results indicated strongly irregular distribution of precipitation in the months of

summer (July, August, and September) and a decrease in the summer rainfall. In this season (summer), the areas in the northwestern and northeastern parts of the basin and to the northwest of Lake Urmia have irregular concentrations of precipitation, while by getting away from the lake, the distribution of precipitation is more regular. The results of zoning the concentration index of rainfall in autumn showed that almost all the regions in the lake basin have moderate concentration and distribution of precipitation. In this season (autumn), a small area to the northwest of Lake Urmia has an irregular distribution of monthly precipitation.

Compared to the other seasons, the distribution of rainfall is more regular in winter. In winter, most of the rain gauge stations in the basin of the lake showed moderate distribution of precipitation. In the surroundings of the lake in this season, the concentration is moderate. Border areas in the basin of Lake Urmia in winter have regular distribution of precipitation. No irregular and strongly irregular concentrations were seen in this season (winter). On the annual scale, the distribution of most of the stations was irregular, which means that the precipitation distribution was irregular among the months of a year. The southeastern part of Lake Urmia on an annual scale has strongly irregular precipitation concentration. Areas in the northwestern and northeastern parts of the Lake Urmia basin are more regularly concentrated. The results of the present research are in accordance with the studies of (*Khalili et al.,* 2014; *Khalili et al.,* 2016) in investigating the concentration and trend of precipitation at synoptic stations of Iran.

3.2. Investigating the concentration index (CI) while studying the precipitation distribution in the basin of Lake Urmia

Basically, the concentration index shows whether or not the share of rainfall events against the total amount of precipitation events can be generally well described by a negative exponential distribution. This method consists of the collection and classification of daily rainfall values with a 1 mm increase, and then determining the relative effectiveness of different classes by analyzing the relative contribution (1 percent) of precipitation. *CI* is basically between 0 and 1, and geometrically shows the triangle between the line $X = Y$ and the exponential curve. When the share of each class to the total precipitation is the same, *CI* approaches 0, and when the share of precipitation is assigned to one class, the exponential curve changes into $Y=0$ line, and *CI* will equal 1. As it was mentioned in Section 2, in order to calculate the concentration index over the basin, first the recorded precipitation of the basin was classified into 1 mm classes. Finally, the value of the concentration index (*CI*) was obtained using Eq. (2) for each station. Similarly, the concentration index was calculated for all of the stations; the results are presented in *Table 3*. The results of studying the daily concentration index at seasonal scale are presented in *Table 4.*

Table 3. Results of calculation of the annual *CI* of rain gauge stations in the period 1984–2013

Station Number	Station	Latitude	Longitude	a	b	S	Annual *Ci*
1	Aghchekol	37.28	46.45	0.17	0.02	2969.68	0.41
2	Bashsisojan	37.80	46.77	0.1	0.02	2638.43	0.47
3	Basmenj	38.00	46.47	0.17	0.02	3053.47	0.39
4	Ghezelchehsadat	38.10	47.30	0.17	0.02	3053.47	0.39
5	Ghooshchisarab	37.78	47.27	0.16	0.02	3028.96	0.39
6	Herissarab	37.83	47.52	0.09	0.02	2526.12	0.49
7	Khooshehmehr	37.32	46.13	0.17	0.02	2969.68	0.41
8	Khormazard	37.42	46.17	0.14	0.02	2811.98	0.44
9	Mehraban	38.08	47.13	0.12	0.02	2697.35	0.46
10	Pardel	38.22	46.17	0.12	0.02	2654.22	0.47
11	Payam	38.35	45.80	0.12	0.02	2654.22	0.47
12	Saidabad	37.95	46.58	0.1	0.02	2638.43	0.47
13	Saray	38.22	46.93	0.06	0.03	2276.26	0.54
14	Sfahlan	37.98	46.12	0.1	0.02	2638.43	0.47
15	Shabestar	38.18	45.70	0.07	0.03	2391.7	0.52
16	Zarnaghheris	38.08	47.08	0.12	0.02	2697.35	0.46
17	Tasooj	38.32	45.37	0.12	0.02	2654.22	0.47
18	Zinjenab	37.85	46.27	0.14	0.02	2811.98	0.44
19	Afan	36.53	45.64	0.1	0.02	2606.73	0.48
20	Alasaghal	36.49	47.04	0.11	0.02	2628.00	0.47
21	Babarood	37.40	45.23	0.1	0.02	2606.55	0.48
22	Badamlu.xls	36.86	46.84	0.14	0.02	2896.44	0.42
23	Baghche-Misheh	36.48	46.77	0.13	0.02	2780.97	0.44
24	Chehreq	38.08	44.59	0.1	0.02	2585.03	0.48
25	Choblocha	36.88	46.40	0.15	0.02	2905.52	0.42
26	Dashband	36.65	46.17	0.11	0.02	2655.65	0.47
27	Gherdeyaghob	37.00	45.72	0.1	0.02	2538.01	0.49
28	Ghezel	36.42	45.97	0.13	0.02	2824.00	0.44
29	Ghezel-Ghaber	36.58	46.65	0.14	0.02	2896.44	0.42
30	Ghoshkhana	36.51	47.30	0.11	0.02	2628.00	0.47
31	Mosh Abad	37.73	45.20	0.11	0.02	2645.33	0.47
32	Naqade	36.96	45.39	0.12	0.02	2665.45	0.47
33	Pey Ghala	36.99	45.03	0.16	0.02	2912.26	0.42
34	Pole sorkhe	36.77	45.71	0.05	0.03	2163.22	0.57
35	Sari Ghamesh	36.48	46.49	0.14	0.02	2791.31	0.44
36	Sero	37.72	44.64	0.12	0.02	2675.28	0.46
37	Tamar	38.11	44.88	0.17	0.02	3053.47	0.39
38	Tapik	37.68	44.90	0.11	0.02	2704.35	0.46
39	Urban	38.35	44.72	0.16	0.02	2958.55	0.41
40	Zarrine	36.97	46.12	0.11	0.02	2660.5	0.47
41	Zereh Shoran	36.69	47.12	0.12	0.02	2743.48	0.45
42	Zhar Abad	37.23	44.96	0.13	0.02	2787.26	0.44

Table 4. Results of calculation of the seasonal *CI* of rain gauge stations in the period 1984–2013

Station Number	Station	Autumn *Ci*	Winter *Ci*	Spring *Ci*	Summer *Ci*
1	Aghchekol	0.39	0.42	0.41	0.40
2	Bashsisojan	0.48	0.47	0.45	0.48
3	Basmenj	0.4	0.41	0.38	0.40
4	Ghezelchehsadat	0.4	0.41	0.38	0.40
5	Ghooshchisarab	0.42	0.4	0.39	0.42
6	Herissarab	0.47	0.45	0.52	0.55
7	Khooshehmehr	0.39	0.42	0.41	0.40
8	Khormazard	0.43	0.40	0.44	0.43
9	Mehraban	0.46	0.46	0.46	0.46
10	Pardel	0.45	0.43	0.49	0.48
11	Payam	0.45	0.43	0.49	0.48
12	Saidabad	0.48	0.47	0.45	0.48
13	Saray	0.55	0.52	0.53	0.53
14	Sfahlan	0.48	0.47	0.45	0.48
15	Shabestar	0.50	0.51	0.52	0.56
17	Zarnaghheris	0.46	0.46	0.46	0.46
17	Tasooj	0.45	0.43	0.49	0.48
18	Zinjenab	0.43	0.40	0.44	0.43
19	Afan	0.46	0.48	0.48	0.56
20	Alasaghal	0.48	0.47	0.48	0.44
21	Babarood	0.47	0.47	0.48	0.54
22	Badamlu.xls	0.40	0.42	0.44	0.42
23	Baghche-Misheh	0.43	0.46	0.41	0.52
24	Chehreq	0.5	0.46	0.49	0.45
25	Choblocha	0.42	0.41	0.41	0.38
26	Dashband	0.46	0.47	0.46	0.45
27	Gherdeyaghob	0.51	0.47	0.50	0.48
28	Ghezel	0.44	0.45	0.41	0.52
29	Ghezel-Ghaber	0.40	0.42	0.44	0.42
30	Ghoshkhana	0.48	0.47	0.48	0.44
31	Mosh Abad	0.48	0.45	0.48	0.41
32	Naqade	0.47	0.46	0.42	0.40
33	Pey Ghala	0.44	0.40	0.42	0.40
34	Pole sorkhe	0.56	0.57	0.56	0.49
35	Sari Ghamesh	0.45	0.44	0.42	0.45
36	Sero	0.47	0.47	0.46	0.44
37	Tamar	0.40	0.41	0.38	0.40
38	Tapik	0.47	0.46	0.47	0.44
39	Urban	0.42	0.40	0.42	0.48
40	Zarrine	0.55	0.47	0.46	0.50
41	Zereh Shoran	0.53	0.46	0.44	0.34
42	Zhar Abad	0.44	0.46	0.42	0.42

To evaluate the accuracy of the coefficients *a* and *b*, function $Y = (a \times X)\exp(b \times X)$ can be employed along with the Lorenz curve. As examples, Lorenz curves of Stations 21 and 23 are presented in *Figs. 4* and *5*. In *Figs. 4* and *5*, Sum Ni (%) is the cumulative sum of the percentage of data frequency per each class, and Sum Pi is the subtraction of the cumulative sum of the frequency values of each class from the class mean.

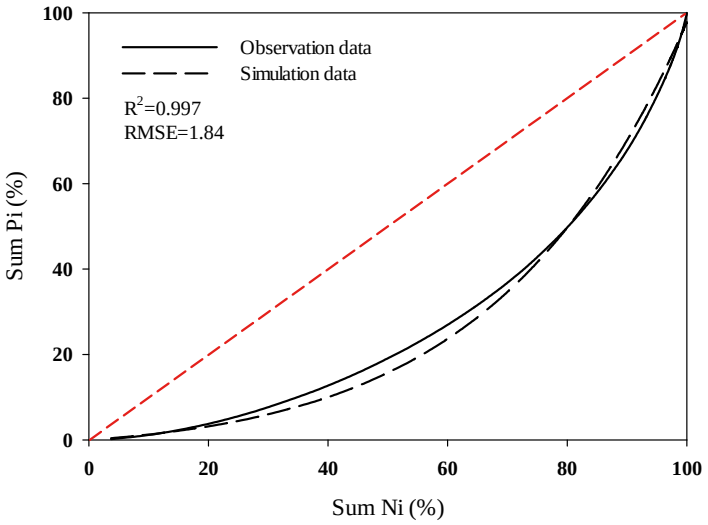

Fig. 4. Concentration (or Lorenz) curves for observed and estimated *CI* values of Babarood station (21)

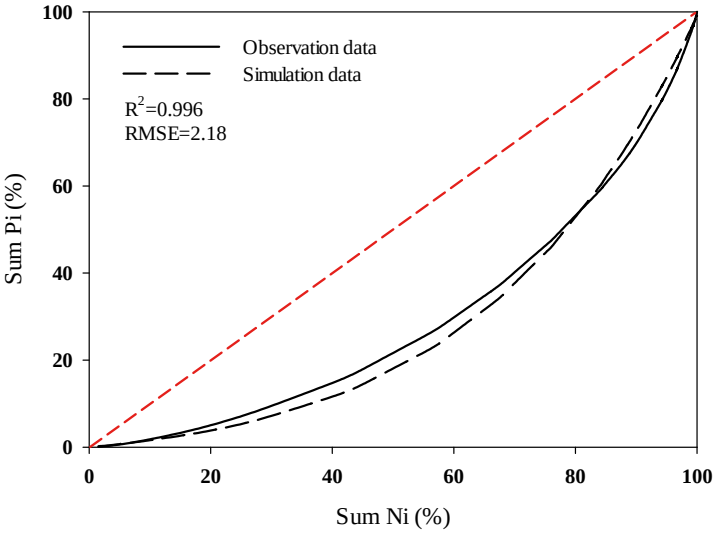

Fig. 5. Concentration, or Lorenz, curves for two observation and estimation *CI* values of Baghcheh-Misheh station (23)

The results of the studies of the concentration index showed that the average value of the index was obtained equal to 0.45 at annual and seasonal scales at all of the stations. On the annual scale, the lowest *CI* value was 0.39, and its maximum value was 0.57. A summary of the results of investigating stations in terms of daily precipitation concentration is presented in *Table 5*. According to the results, it can be concluded that the maximum value of *CI* on all the studied scales was 0.57 and 0.56.

Table 5. Summary of the results related to *CI* from 1984 to 2013

CI	**Annual**	**Autumn**	**Winter**	**Spring**	**Summer**
Max	0.57	0.56	0.57	0.56	0.56
Min	0.39	0.39	0.40	0.38	0.34
Average	0.45	0.46	0.45	0.45	0.45

According to the researches of Martin-Vide (2004), big values of *CI* (*CI* > 0.61) indicate a high concentration of daily precipitation, moreover, at stations with *CI*>0.6, the precipitation occurred on the 25 percent of rainy days. This indicates the possibility of highly aggressive and severe rainfalls at stations with *CI* > 0.61. *CI* < 0.61 values are more regularly distributed with regard to the daily rainfall, and the lower this number, the more regular station of interest is in terms of the number of rainy days and daily precipitation. In the present study, *CI* > 0.61 was observed at none of the studied stations. At annual scale, Stations 4, 3, 5, and 37 had the lowest *CI*, while the highest *CI* value was calculated for the Pole Sorkhe (34) station. To evaluate the concentration index regionally, *CI* values in the basin on different scales were zoned, and are presented as *Fig. 6*.

Based on the results of the studies of the concentration index (*CI*) in the period under review, no *CI* > 0.6 was observed in spring in any part of the study area. *CI* values were between 0.4 and 0.5 (the yellow parts) for most areas of the lake basin in this season (spring), while aggressive and severe precipitation was observed in none of the areas of the basin. In the northeast region of Lake Urmia and partly to the south of the lake, *CI* was 0.5 to 0.6, which represents irregular daily precipitation in these areas. The daily distribution of precipitation is more regular in the southern part of the basin, and a regular exponential distribution fits the rainfall data of the rainy days. As it was seen in spring, the daily precipitation in the southern basin of Lake Urmia is more regularly distributed. In autumn in the study area, like spring, *CI* > 0.6 was observed at none of the stations studied. Some areas in the eastern and southern, as well as the northeastern and southeastern parts of the basin of Lake Urmia, are more irregular than the others.

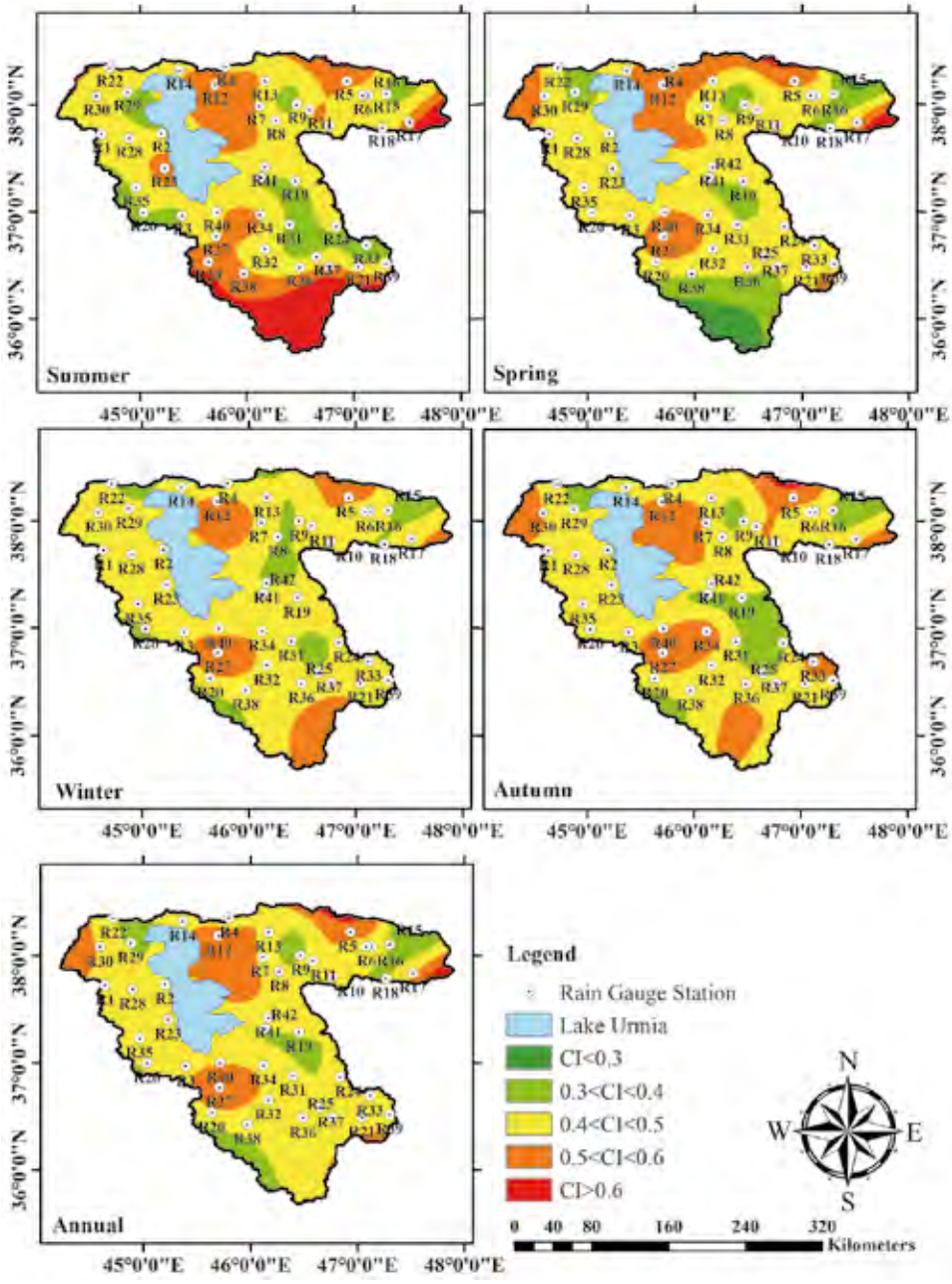

Fig. 6. Spatial distribution of *CI* index in annual and seasonal time scales in the period of 1984–2013.

The results showed that in both spring and autumn, these areas have severe and thunder-like rainfalls on days with precipitation, and the precipitation distribution in the rainy days is of less regularity than in the other regions. Areas in the eastern and northeastern parts of the basin (the areas colored green) are also relatively regular in terms of daily precipitation distribution. Other regions (colored yellow) deal with a moderate distribution of daily rainfall. Regular concentration was not observed in this season either. In winter, similarly to spring and autumn, areas to the south and northeast of Lake Urmia, as well as a region in the northeastern part of the basin in the period studied have an average *CI* value between 0.5 and 0.6, indicating strong concentration of daily precipitation and irregularity in the daily precipitation distribution in these areas. Also, it can be concluded that the amount of daily rainfall in the abovementioned areas is not divided regularly among the days with precipitation. Most areas of the basin have a *CI* between 0.4 and 0.5. In this season, neither regular distribution ($CI < 0.3$) nor irregular distribution ($CI > 0.6$) of daily rainfall was observed. Some small areas in the eastern part of the basin of Lake Urmia had *CI* values between 0.3 and 0.4, indicating a regular distribution of daily rainfall in winter days. In other words, the amount of precipitation is distributed fairly regularly in this season among the days with precipitation in the abovementioned areas. There is strongly irregular precipitation in summer in the southern parts of the lake basin, so that it can be concluded that 70 percent of the precipitation in this season has occurred only on 25 percent of the rainy days (days with precipitation).

In this season, the northeastern and southern regions of the lake, an area in the northeastern, and also a station in the southwestern region of the lake are of irregular concentration distributions of summer precipitation. In this season (summer), the regular distribution of daily rainfall was not observed in the basin. Some stations to the northwest of Lake Urmia and also to the southeast and west of the lake were of relatively regular daily precipitation. On an annual scale, most areas of the lake basin fell within the moderate concentration class (*CI* between 0.4 and 0.5). On this scale (annual), similarly to the seasonal scales, the northeastern and southern regions of Lake Urmia basin had more irregular concentration than the other areas. On an annual scale, regular daily precipitation distribution was observed at none of the stations studied throughout the basin of Lake Urmia. Moreover, the eastern part of the basin faces an increased precipitation irregularity in the time scales studied, though this change is not significant. Nonetheless, the reduction in precipitation reported by (*Asakereh* and *Razmi*, 2012; *Dinpashoh et al*., 2013; *Khalili et al.*, 2016) had a significant impact on the status of water resources of the region and can even be involved as an influencing factor on the drying up of Lake Urmia.

4. Conclusion

The results of the investigation of the annual precipitation concentration showed that in the basin of Lake Urmia, the precipitation distribution is generally irregular. The values of precipitation distribution index for the stations located to the east of Lake Urmia was 17.55 and for the stations to the west of the lake it was 16.37, indicating that precipitation is more irregular in the eastern parts of the lake than in the western parts. The irregularity of precipitation in the eastern parts of Lake Urmia basin will lead to more extreme rainfall events. The results also showed that during the period under review, the concentration index of precipitation at stations in the western and eastern parts of the lake had increased by 0.38 and 4.06 percent, respectively. Meanwhile in spring, the results indicated that precipitation distribution during the period under review became more regular. In summer, as in spring, a decrease in the concentration index of precipitation over the basin of Lake Urmia was observed, which represents a uniform distribution of rainfall in the months of summer. The concentration of autumn precipitation during the last 10 years of the study period in relation to the first 10 years has increased by about 20.54 percent. In this, the share of the western areas of Lake Urmia is about 19.91 percent, and the share of the eastern part of the lake is about 21.22. The increase in the concentration index over the basin of Lake Urmia in autumn depicts that the precipitation distribution has changed from moderate distribution to irregular distribution; this increase can increase autumn extreme precipitation events.

Based on the *PCI* index, winter precipitation at the basin studied is moderate and regular in terms of distribution, which demonstrates a uniform and moderate precipitation distribution in the months of winter. The results generally showed that the distribution of annual and autumn precipitation patterns of the basin of Lake Urmia, particularly in the eastern parts of the basin, became irregular from 1984 to 2013; this indicates the possibility of extent rainfall and flooding events in this season. The results of the studies of the concentration index throughout the basin showed that the daily rainfall of basin of Lake Urmia was within neither strongly irregular nor regular conditions at any of the stations. In the meantime, most of the stations studied were in the moderate concentration class in terms of daily precipitation distribution. In autumn, winter, spring, summer, and on the annual scale, 74, 90, 81, 74, and 84 percent of the rain gauge stations studied were respectively of moderate precipitation concentration. According to the results of the values of concentration index (*CI*), there is a possibility of severe and extreme precipitation in the southern and eastern parts of the basin of Lake Urmia; this possibility would increase over the course of time. Recent floods in the eastern part of the lake confirm these results. By analyzing and studying the concentration index and the precipitation concentration index, it is possible to investigate extreme events as well as the irregularity and inequality of daily, monthly, and annual precipitation. Hence, further researches should be considered to determine

the correlation between the precipitation concentration index and the occurrence of extreme events such as floods, soil erosion, and drought.

Also the results of comparing two 10-year-long sub-periods indicated that *PCI* index of the second sub-period increased in the spring time scale that means that the irregularity of precipitation distribution has been increased, while in the other seasons significant variations were not observed. Also in the annual time scale, *PCI* index has been increased in the second sub-period because of the increasing trend of precipitation. These results showed the importance of applying techniques of water resources management in most parts of Iran, especially in the northwestern areas of Iran, where Lake Urmia and agricultural fields are located.

The evaluated indices, as statistical indicators, can specify different weights of precipitation, including distribution, share of extreme precipitation, and spatial distribution in relation to the total precipitation. One of the benefits of studying drought indices, such as the *PCI*, is the ability to observe the precipitation distribution among the months of a season and even a year, and also to distinguish the governing distributions. Therefore, the results may be utilized when facing droughts or extreme rainfall conditions.

Acknowledgements: The authors would like to thank the West Azerbaijan Regional Water Authority for providing river flow data. Also, authors are thankful to University of Birjand, Birjand, Iran.

References

Adegun, O., Balogun, I., and A*deaga, O.*, 2012. Precipitation concentration changes in Owerri and Enugu. Special Publication of the Nigerian Association of Hydrological Sciences: 383–391.

Alijani, B., O'brien, J., and *Yarnal, B.,* 2008. Spatial analysis of precipitation intensity and concentration in Iran. *Theor. Appl. Climatol. 94*, 107–124. https://doi.org/10.1007/s00704-007-0344-y

Brooks, C.E.P. and *Carruthers, N.*, 1953. Handbook of statistical methods in meteorology. Handbook of statistical methods in meteorology. R Met. Soc, London.

Cortesi, N., González-Hidalgo, J.C., Brunetti, M., and Martin-Vide, J., 2012. Daily precipitation concentration across Europe 1971-2010. Nat. Hazard. Earth Sys. Sci. 12, 2799. https://doi.org/10.5194/nhess-12-2799-2012

De Luis, M., Gonzalez-Hidalgo, J., Brunetti, M., and Longares, L., 2011. Precipitation concentration changes in Spain 1946-2005. Nat. Hazard. Earth Sys. Sci. 11, 1259. https://doi.org/10.5194/nhess-11-1259-2011

Dinpashoh, Y., Mirabbasi, R., Jhajharia, D., Abianeh, H.Z., and *Mostafaeipour, A.*, 2013. Effect of short-term and long-term persistence on identification of temporal trends. *J. Hydrol. Engineer. 19*, 617–625. https://doi.org/10.1061/(ASCE)HE.1943-5584.0000819

Gong, D.Y. and *Ho, C.H.*, 2002. Shift in the summer rainfall over the Yangtze River valley in the late 1970s. *Geophys. Res. Lett. 29*. https://doi.org/10.1029/2001GL014523

Khalili, K., Nazeri Tahrudi, M., and *Khanmohammadi, N.*, 2014. Trend analysis of precipitation in recent two decade over Iran. *J. Appl. Environ. Biol. Sci. 4*, 5–10.

Khalili, K., Tahoudi, M.N., Mirabbasi, R., and *Ahmadi, F.*, 2016. Investigation of spatial and temporal variability of precipitation in Iran over the last half century. *Stoch. Environ. Res. Risk Assess. 30*, 1205–1221. https://doi.org/10.1007/s00477-015-1095-4.

Khozeymehnezhad, H., and Tahroudi, M.N., 2019. Annual and seasonal distribution pattern of rainfall in Iran and neighboring regions. *Arab. J. Geosci. 12*, 1-13.

Li, X., Jiang, F., Li, L., and *Wang, G.*, 2011. Spatial and temporal variability of precipitation concentration index, concentration degree and concentration period in Xinjiang, China. *Int. J. Climatol. 31*, 1679–1693. https://doi.org/10.1002/joc.2181

Martin-Vide, J., 2004. Spatial distribution of a daily precipitation concentration index in peninsular Spain. *Int. J. Climatol. 24*, 959–971. https://doi.org/10.1002/joc.1030

Olascoaga, M., 1950. Some aspects of Argentine rainfall. *Tellus 2*, 312–318. https://doi.org/10.3402/tellusa.v2i4.8601

Oliver, J.E., 1980. Monthly precipitation distribution: a comparative index. *Profess. Geogr. 32*, 300–309. https://doi.org/10.1111/j.0033-0124.1980.00300.x

Ren, G., Wu, H., and *Chen, Z.*, 2000: Spatial patterns of change trend in rainfall of China. *Quart. J. Appl. Meteorol. 11*, 322–330.

Riehl, H., 1949. Some aspects of Hawaiian rainfall. *Bull. Amer. Meteorol. Soc. 30*, 176–187. https://doi.org/10.1175/1520-0477-30.5.176

Shi, W., Yu, X., Liao, W., Wang, Y., and *Jia, B.*, 2013. Spatial and temporal variability of daily precipitation concentration in the Lancang River basin, China. *J. Hydrol. 495*, 197–207. https://doi.org/10.1016/j.jhydrol.2013.05.002

Tabari, H., Marofi, S., Aeini, A., Talaee, P.H., and *Mohammadi, K.*, 2011. Trend analysis of reference evapotranspiration in the western half of Iran. *Agric. Forest Meteorol. 151*, 128–136. https://doi.org/10.1016/j.agrformet.2010.09.009

Tahroudi, M.N., Khalili, K., Ahmadi, F., Mirabbasi, R., and Jhajharia, D. 2019. Development and application of a new index for analyzing temperature concentration for Iran's climate. *Int. J. Environ. Sci. Tech. 16*, 2693-2706.

Valli, M., Sree, K.S., and *Krishna, I.V.M.*, 2013. Analysis of precipitation concentration index and rainfall prediction in various agro-climatic zones of Andhra Pradesh, India. *Int. Res. J. Environ. Sci. 2*, 53–61.

Zamani, R., Mirabbasi, R., Nazeri, M., Meshram, S.G., and *Ahmadi, F.*, 2018. Spatio-temporal analysis of daily, seasonal and annual precipitation concentration in Jharkhand State, India. *Stoch. Environ. Res. Risk Assess*. *32*, 1085–1097. https://doi.org/10.1007/s00477-017-1447-3

Zhai, P., Zhang, X., Wan, H., and *Pan, X.*, 2005. Trends in total precipitation and frequency of daily precipitation extremes over China. *J. Climate 18*, 1096–1108. https://doi.org/10.1175/JCLI-3318.1

Zhang, Q., Xu, C.-y., Gemmer, M., Chen, Y.D., and *Liu, C.*, 2009. Changing properties of precipitation concentration in the Pearl River basin, China. *Stoch. Environ. Res. Risk Assess 23*, 377–385. https://doi.org/10.1007/s00477-008-0225-7

Zhang, Q., Xu, C. Y., Zhang, Z., Chen, Y. D., Liu, C. L., and Lin, H., 2008. Spatial and temporal variability of precipitation maxima during 1960–2005 in the Yangtze River basin and possible association with large-scale circulation. *J. Hydrol. 353*, 215–227. https://doi.org/10.1016/j.jhydrol.2007.11.023

DOI:10.28974/idojaras.2020.1.5

IDŐJÁRÁS

Quarterly Journal of the Hungarian Meteorological Service
Vol. 124, No. 1, January – March, 2020, pp. 97–111

Winter air temperature in Warsaw depending on the NAO index and the regional circulation

Robert Twardosz*[,1] and **Urszula Kossowska-Cezak**[2]

[1]*Institute of Geography and Spatial Management*
Jagiellonian University
ul. Gronostajowa 7, 30-387 Kraków, Poland

[2]*Department of Climatology*
Faculty of Geography and Regional Studies
Warsaw University
ul. Krakowskie Przedmieście 30, 00-927 Warszawa, Poland

**Corresponding Author e-mail: r.twardosz@uj.edu.pl*

(Manuscript received in final form March 8, 2019)

Abstract— The paper discusses the circulation and thermal conditions over Poland and their dependence on the sign and values of the North Atlantic Oscillation (NAO) index (hereinafter NAO+ and NAO-). The input data used in the research consisted of average monthly values of air temperature in Warsaw, NAO index values, and a calendar of atmospheric circulation types according to *Lityński* (1969). The study comprised the three winter months (December, January,February) from the period 1951–2015. The dependence between the circulatory and thermal conditions was investigated on the basis of 10 months representing each of the winter months with the highest NAO+ and NAO- values and 10 months with the greatest positive and negative temperature deviations from the long-term average (Δt+, Δt-), based on the assumption, that they should largely be the same months. In general, the analysis confirmed these assumptions, but it also showed that there are deviations from previously known regularities as regards the effect of the positive or negative phases of the NAO on the thermal conditions in Poland.

Key-words: atmospheric circulation, NAO, air temperature, Warsaw

1. Introduction

The temperate zone is characterized by the high variability of atmospheric circulation, which translates into significant variations in weather conditions. This follows from the fact that the zone is under the influence of the formation, evolution, and movement from west to east of families of dynamic cyclones separated by high-pressure ridges. This results from the global system of atmospheric circulation, which – in this zone – takes place within the Ferrel cell, i.e., between subtropical anticyclones and moderate-latitude cyclones. In the Northern Atlantic, the Icelandic Low and the Azores High are such centers of atmospheric activity. The values of atmospheric pressure between these two systems demonstrate a negative correlation (*Marsz,* 2002), which means that when pressure within the Icelandic Low drops, it increases in the Azores High and vice versa. However, as *Marsz* (2002) explains, the interrelations between these two pressure centers are not stable. It may so happen that only one of them can be strong or weak.

The relationships between the Azores High and the Icelandic Low have been known for over 100 years (*Hurrell,* 1995; *Wibig,* 2000), and in the 1920s the phenomenon was named the North Atlantic Oscillation or NAO.

The development of the NAO index as a quantitative characteristics of westerly circulation (or lack thereof) over the eastern part of the Atlantic at the latitude of Europe created new research opportunities. These include, inter alia, an opportunity for investigating the relationship between the air temperature in Poland in individual winter months and the sign and value of the index. However, since temperatures in Poland are determined directly by the circulation over its territory, studying the link between air temperature and the NAO should include an intermediate stage, i.e., an analysis of atmospheric circulation over Poland. This follows from the fact that smaller areas may observe meso-circulation processes, which are determined by regional geographic factors and differ from those occurring on the macroscale. This was clearly shown by *Niedźwiedź* (2002), who determined the statistical relationship between the zonal circulation index over Poland and the NAO index. The correlation coefficients obtained by Niedźwiedź were significant only from December to April, with the highest dependence in February ($r = 0.66$).

Thus, this study focuses on answering the question on how a specific NAO phase and its intensity influence air temperatures at a distance of nearly 2000 kilometers from the Atlantic coast. As the sea air masses travel the distance, not only do they undergo significant transformation, but they may also change their primary trajectory as a result of pressure systems forming over Europe. Therefore, in central Europe, as well as in other parts of it (*Castro-Diez et al.* 2002; *Kossowska-Cezak* and *Twardosz,* 2018), the relationship between the air temperature in winter and the positive or negative NAO phase may be, but does not need to be, strong or even unambiguous, even though numerous studies (as

well as non-scientific observations) indicate the existence of such a relationship. For example, it has been found that warm or cold winters in Europe correspond to a specific phase of the NAO (*Saunders* and *Lea*, 2006; *Hirschi* and *Sinha*, 2007; *Hirschi*, 2008; *Cattiaux et al*., 2010; *Wang et al.*, 2010; *Buchan et al.*, 2014).

2. Data and methods

This study is based on a 65-year-long series (1951–2015) of the NAO index defined as the difference the between normalized sea level pressure over Gibraltar and the normalized sea level pressure over Southwest Iceland (*Jones et al.*, 1997). The values were taken from the website of the *Climate Research Unit* (http://www.cru.uea.ac.uk/cru/data/nao.htm). The second set of data consists of average monthly values of air temperature in Warsaw and a calendar of circulation types according to *Lityński* (1969), as developed by *Pianko-Kluczyńska* (2007). The calendar includes 27 types of circulation, including nine cyclonic types, nine "0" (transitional) types, and nine anticyclonic types from 8 directions, as well as a ninth, advectionless type. The study covers the three coolest months of the year, i.e., from December to February. Based on previous research, we know that the North Atlantic Oscillation has the strongest effect on temperatures in winter, when westerly movement of air masses clearly predominates (*Hurrell*, 1995; *Marsz*, 2002). This is attributable to the greatest thermal contrasts between air masses in the extratropical areas of the Northern Hemisphere during the year.

The dependence between the air temperature in Warsaw in the 3 winter months of the 65-year period and the NAO index value demonstrates that the majority of the values of both characteristics clearly diverge from the dependence line and the 95% confidence interval (*Fig. 1*). Therefore, studying the circulatory and thermal conditions over Poland relative to the sign and value of the NAO index (hereinafter NAO+ and NAO-) is not based on the full 65-year series of average values for the 3 months (December-February), but on values from selected months. Thus, 10 months from the 65-year period with the highest positive and negative NAO values (hereinafter: high NAO+ and high NAO-) and 10 months with the highest positive and negative (Δt) deviations from the multiannual average (hereinafter: high Δt+ and high Δt-) were selected for analysis. If there was a close relationship between the monthly NAO and Δt values, then the months identified independently according to each criterion (NAO or Δt) would be the same, while in the absence of such a relationship, the months would be completely different. As is demonstrated by the summary in *Table 1*, in the months with high NAO+ or high Δt+, the sign of the other characteristics was opposite (Δt-, NAO-) in only one month, while in the months

with high NAO- or high Δt- there were more similar cases, namely 8. This confirms that, as expected, the consistency between the signs of NAO and temperature Δt is greater for positive values than for negative ones. This should be attributed to the different numbers of atmospheric pressure field types during specific phases of the NAO over the North Atlantic and Europe. According to *Styszyńska* (2002), the positive phase of the NAO involves one or two pressure field types, while during the negative phase, the number of the possible field types can be very different.

At this point it should be observed that despite their apparent similarity (+ or -), the compared values of the average monthly NAO and the deviations of the monthly average temperature from the long term average (Δt) are two completely different kinds of value. The NAO index informs us about a current pressure system distribution over the Northern Atlantic Ocean. On average, and most frequently, the two dominant pressure systems are the Azores High and the Icelandic Low, and the resulting pressure gradient runs from south to north, while the NAO is positive. Shifts in the exact location of these pressure systems and their pressure values are reflected in constant changes in the NAO value and, periodically, also in its sign. In this way, NAO provides objective information about the status of the atmospheric pressure distribution. The deviation of the air temperature in a given month from the long-term average, on the other hand, is a relative metric, where the sum of deviations over a relevant multi-year period arrives at nil.

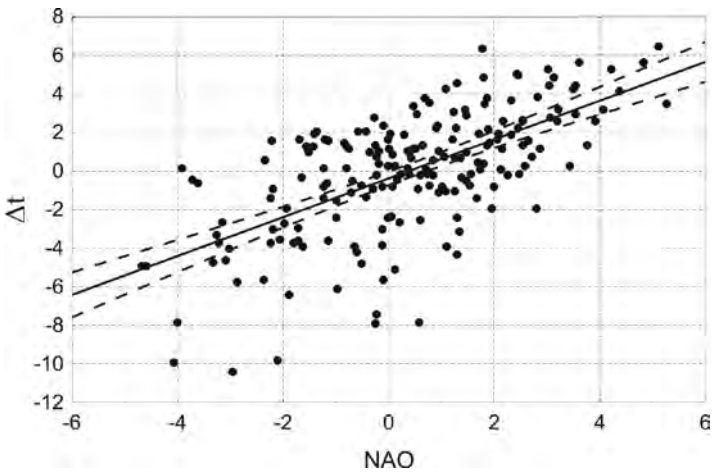

Fig. 1. Relationship between the deviation of average temperature (Δt) in the winter months in Warsaw from the NAO index and the 95% confidence interval of the regression line, (1951–2015). The correlation coefficient is r = 0.600 significant at the level of significance α=0.05.

Table 1. Number of months with high NAO +/- and/or high Δt +/- (1951–2015)

		Dec	Jan	Feb	Dec –Feb
NAO+	Δt+	6	5	5	16
	(Δt+)	4	5	4	13
	(Δt-)	–	–	1	1
Δt+	NAO+	6	5	5	16
	(NAO+)	4	5	5	14
	(NAO-)	–	–	–	–
NAO-	Δt-	7	7	4	18
	(Δt-)	2	2	4	8
	(Δt+)	1	1	2	4
Δt-	NAO-	7	7	4	18
	(NAO-)	3	2	3	8
	(NAO+)	–	1	3	4

Explanation: NAO +/- – months with a positive/negative NAO index; Δt +/- – months with a positive/negative deviation of temperatures from the multiannual average; symbol without parentheses – "high" value, i.e., one of the 10 highest values in the 65-year period; symbol in parentheses – value lower than the tenth highest in the 65-year period.

3. Atmospheric circulation over Poland in selected months with a high monthly average value of the NAO and/or Δt

The frequency of circulation types over Poland according to *Lityński* (1969) was calculated for all the months when a high value occurred (i.e., which saw one of the 10 highest positive and negative NAO and/or Δt values). Following this, the average frequency of days with circulation from individual directions and with cyclonic, "0" (transitional), and anticyclonic circulation across the categories of months distinguished according to the sign and size of NAO and Δt were calculated. When compiling the months selected on account of a high NAO and/or Δt value, the NAO index was adopted as the primary characteristic (*Table 2*). The average number of days with circulation from each direction and of different nature is given in integral values for a 31-day month.

Table 2. The average number of days in a month with circulation from the individual directions and of different nature (according to Lityński (1969)) during different categories with high NAO+/- and/or high Δt+/-. The highest values are marked with bold type, C is for cyclonic types, 0 is for types "0" (transitional types), A is for anticyclonic types

Month category	No. of months	N	NE	E	SE	S	SW	W	NW	0	C	0	A
NAO+/Δt+	16	2	–	–	1	2	**9**	**8**	**8**	1	10	9	12
NAO+/(Δt+)	13	4	2	1	1	3	**6**	**6**	**6**	3	9	7	15
(NAO+)/Δt+	14	2	1	2	2	**5**	**7**	**4**	**6**	2	14	9	8
(NAO+)/Δt-	4	4	3	**6**	**7**	3	2	2	3	2	11	8	12
NAO-/Δt-	18	3	**6**	**7**	**6**	3	1	1	1	3	10	8	13
NAO-/(Δt-)	8	4	4	4	**8**	4	2	1	2	2	13	10	8
(NAO-)/Δt-	8	3	4	**6**	**6**	5	1	1	1	4	7	8	16
NAO-/(Δt+)	4	3	1	4	**6**	**6**	3	3	2	3	16	8	7

Explanation as in *Table 1*. The single month in the NAO+/Δt- category is disregarded.

3.1. Months with a positive value of the NAO index

In all the months from December to February in which the positive phase of the NAO occurred and the mean temperature in Warsaw was higher than the long-term average, there was a clear predominance of days with circulation from the western sector and a small number of days with circulation from the eastern sector.

In the months with high NAO+ and Δt+ (16 months) values, there was an average of 25 days with circulation from the SW-NW sector, and a mere 1 day from the NE-SE sector; advectionless situations also appeared, but they were very rare. The share of cyclonic, "0" (transitional), and anticyclonic types was fairly balanced, with a slight advantage of the last type (*Table 2*). In this category of months, several months stood out. The second highest NAO+ value (5.11) and one of the two highest Δt+ values (6.5 °C, which is equivalent to 1.8 standard deviations) occurred in February 1990 (28 days), when SW-NW circulation occurred on 24 days. At the time, the greatest deviation of air temperature considered to be anomalous, i.e., exceeding 2 standard deviations ($t \geq t_{av.}+2\sigma$) covered vast areas of Europe from Scandinavia and northern western part of Russia, through southern western part of Europe to the islands of the western Mediterranean Sea (*Fig. 2*). In Kajaani and Arkhangelsk, the

temperature anomaly was Δt=10.5 ºC, and even in Bordeaux, it exceeded 5 ºC. The same group also included the previous month January 1990 (NAO = 3.5, Δt = 4.5 ºC). As a result of having two such warm months in succession (and a fairly warm December), the winter of 1989/90 was one of the mildest in Europe in the mid-20th century (*Kossowska-Cezak* and *Twardosz*, 2017). In January 1983, which saw the highest January NAO+ (4.82) and Δt+ (5.8 ºC), there were 19 days with SW-NW circulation. February 1995 (NAO=3.13, Δt = 5.0 ºC) had 27 days with circulation from this sector (out of 28). December 2015 saw both the highest December NAO+ (4.22) and Δt + (5.4 ºC); there were 23 days with SW-NW circulation and 3 days with circulation from the south.

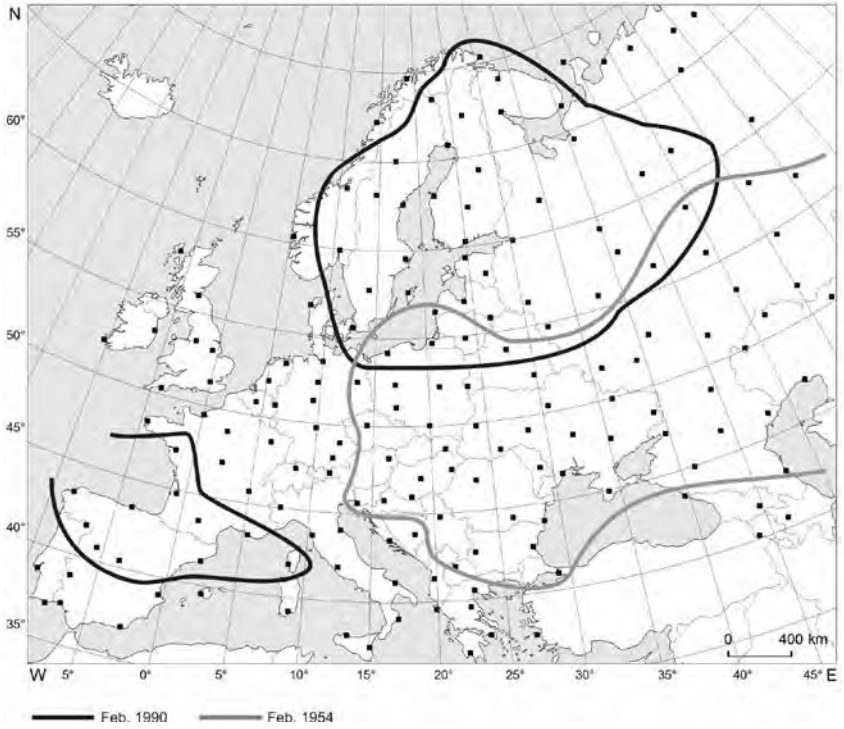

Fig. 2. Ranges of the positive (Δt+) and negative (Δt-) thermal anomalies during the positive NAO phase: February 1990 – NAO+/Δt+; February 1954 – (NAO+)/Δt- (explanations as for *Table 1*, the ranges are based on the publication by *Kossowska-Cezak* and *Twardosz*, 2017)

Months with high NAO+ do not always see high Δt+. In months with lower temperature deviation from the multiannual mean [NAO+/(Δt+), 13 months, *Table 1*], the average number of days with SW-NW circulation was 18 (*Table 2*), and from the opposite sector it was 4, i.e., NE-SE with a slightly higher share of days with northerly (N – 4 days) and/or southerly circulation (S – 3 days). For example, January 1974 (NAO=3.75, Δt=1.4 ºC) had 12 days with SW-NW circulation, 11 days with S and 5 days with SE circulation, while in February 1961 (NAO=4.06, Δt=3.3 ºC), SW-NW circulation occurred on 14 days, while N circulation on 6 days. This category of months also included February 1997, with the highest value of NAO+=5.26 (Δt = 3.5 ºC) in the 65-year period. There were 23 days with SW-NW circulation, 4 days with circulation from the northeastern sector, and 15 days with anticyclonic circulation.

However, a high positive temperature deviation from the long-term average may occur in months with a relatively low NAO+ value [(NAO+)/Δt+, 14 months, *Table 1*]. This group included months with a wide range of NAO+ values from the "high" categories to the near-zero ones, and thus to the variation in the share of circulation directions in individual months. However, on average, days with SW-NW circulation predominated (17 days, *Table 2*), with 5 days on average with circulation from the opposite sector. This group included January 2007, with one of the two highest winter Δt+ = 6.5 ºC, (1.9 standard deviations; NAO = 1.76). That month saw 27 days with SW-NW circulation and only one day with circulation from the NE-S sector; at the same time, it was the only month with a complete absence of anticyclonic circulation. At the time, a positive temperature anomaly extended to the southern and central parts of Europe and the southeastern part of European Russia (*Kossowska-Cezak* and *Twardosz*, 2017). Also, February 1998 was a month in the (NAO+)/Δt+ category (NAO = 2.44, Δt = 5.0 ºC) recording 19 days with SW-NW circulation and no days with circulation from the NE-SE sector, but there were 3 days each with N and S circulation and anticyclonic circulation prevailed (15 days). This group also included January 1965 (NAO = 0.01, Δt = 3.5 ºC) and February 1974 (NAO = 0.68, Δt = 3.9 ºC), in which the number of days with SW-NW was 10 and 12, respectively, and the number of days with NE-SE circulation was 11 and 10, respectively; cyclonic circulation prevailed in both months – 15 and 13 days, respectively.

During spells with the positive NAO phase, there were occasional months when the average temperature in Warsaw was lower than the long-term average (4 months during the 65 years, *Table 1*). These months included February 2011, which represents the category (NAO = 2.79, Δt = -2.0 ºC). The low temperature in that month was determined by the prevailing share of SE circulation (11 days), which was mostly anticyclonic in nature (14 days).

Months with a greater negative deviation of mean temperature from the multiannual average, but with a low positive value of the NAO index, i.e., the (NAO+)/Δt- category months were more frequent (4 months). In those months, the NAO value ranged from 0.01 to 1.28. Circulation from the NE-SE sector was predominant (16 days on average – *Table 2*), and that from the SW-NW sector was the least frequent (7 days). The months of this category included the anomalously cold February 1954 (NAO = 0.57, Δt = -7.8ºC). That month saw circulation from the E-S sector for 27 days, and anticyclonic circulation for 26 days. At the time, the negative temperature anomaly was present across vast areas of Europe from the southern Baltic countries to the shores of the Caspian Sea (*Fig. 2*); in Astrakhan, the temperature anomaly (Δt-) was -14.0 ºC (*Kossowska-Cezak* and *Twardosz,* 2017).

3.2. Months with a negative value of the NAO index

During negative NAO phases from December to February, Warsaw usually saw a monthly average temperature below the long-term mean. In those months, the prevailing circulation in Poland was that from the NE-SE direction, but its predominance was not as strong as for the SW-NW circulation in the NAO+ months, with advectionless situations being more frequent.

On average, in the months with a high NAO- and, at the same time, high Δt- (18 months, *Table 2*), there were on average 19 days with circulation from the NE-SE and only 3 days with circulation from the opposite sector (*Table 2*). Two examples of such months were December 1996, which experienced the greatest December NAO- in the 65-year period (-4.70, Δt = -4.7 ºC), and December 2010 with the second highest NAO- (NAO = -4.61, Δt = -4.7 ºC). During the latter month, the negative temperature anomaly stretched across the entire northwestern part of Europe (*Fig. 3*). In those months, NE-SE circulation was recorded on 13 and 15 days, respectively, with SW-NW circulation occurring only 5 and 7 times; furthermore, in December 1996, there were 6 days with advectionless situations. January 1963, which had the highest NAO- (-4.09), observed both the highest January Δt- and the second highest negative winter temperature anomaly (Δt = -9.8 ºC). That month stood out for the dominance of circulation from the N-E sector (27 days, including 13 days with NE) and the complete absence of circulation from the SW-NW sector; anticyclonic circulation prevailed (21 days). In that month, the negative temperature anomaly extended in Europe from the British Isles and France to western Russia and Ukraine (*Fig. 3*). At the eastern ends of the anomaly, Δt exceeded -10 ºC. The month that followed – February 1963 – was of the same category (NAO = -1.90, Δt = -6.3 ºC), with a prevalence of the NE-SE circulation (25 days) and, likewise, an absence of the SW-NW circulation. At the time, the negative thermal anomaly covered western Europe and the

Greenland Sea and Barents Sea islands, where Δt exceeded -10 °C (*Kossowska-Cezak* and *Twardosz*, 2017). The entire winter of 1962/63 was anomalously cold. The greatest negative thermal anomaly in Warsaw in the 65-year period (Δt = -10.4°C) was also recorded during a month in this category, namely in February 1956 (NAO = -2.96). In that month, NE-SE circulation was recorded on 26 days, and that from W and NW on 2 days; there were 15 days with anticyclonic circulation. February 1956 was highly exceptional, because it was the only month in the 65-year period when the negative temperature anomaly covered more than half of the continent, from the Pyrenean Peninsula to the Urals (except Scandinavia and northern Russia, *Fig. 3*). The greatest anomaly occurred in central Europe (Δt = -11 – -12 °C) (*Kossowska-Cezak* and *Twardosz*, 2017). It should be noted that at least half of the months in this category were classified as anomalously cold ($t \leq t_{av.} - 2\sigma$).

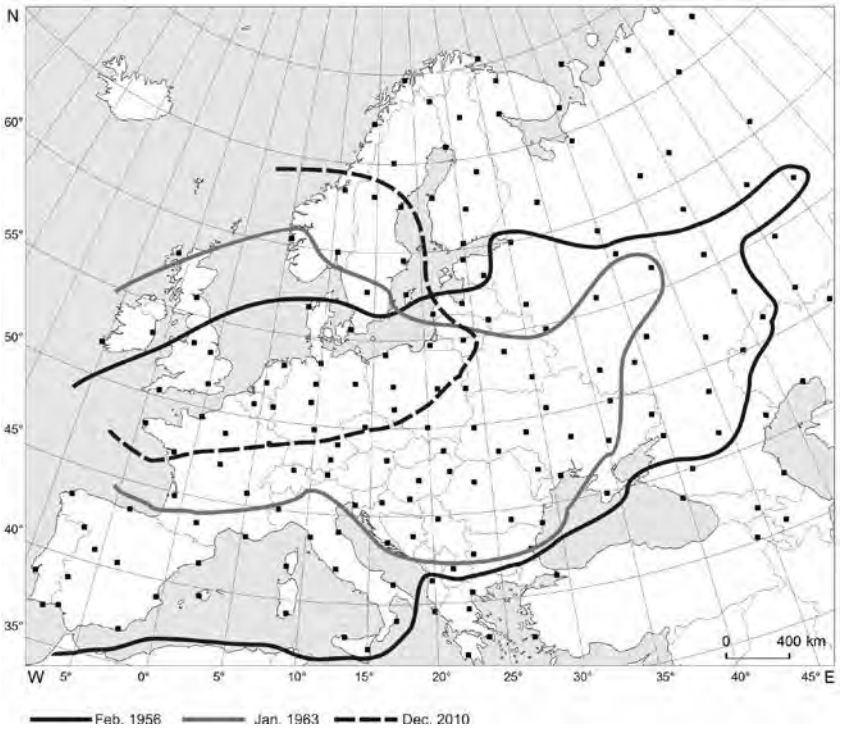

Fig. 3. Ranges of the negative thermal anomaly during the negative NAO phase – NAO-/Δt- (explanations as for *Table 1*, the ranges are based on the publication by *Kossowska-Cezak* and *Twardosz*, 2017)

Not every month with high NAO- see high negative deviations of temperature from the long-term average. In the months of the NAO-/(Δt-) category (8 days, *Table 1*), the disproportion between the number of days with the NE-SE and SW-NW circulations is lower; an average of 16 and 5 days respectively (*Table 2*). Such months included, inter alia, February 1969 (NAO = -3.16, Δt = -2.6 ºC), which saw 23 days with E-S circulation, including 18 days with SE, and only 2 days altogether with SW and W, as well as December 1976 (NAO = -3.63, Δt = -0.5 ºC), in which there were only 12 days with NE-SE circulation and 12 days with circulation from the S-SW section.

By contrast, significant deviation of monthly average temperatures from the long-term average can occur in months with a low NAO- value [category (NAO-)/Δt-; 8 months, *Table 1*]. In those months, there were on average 16 days with NE-SE circulation and 3 days with SW-NW circulation; advectionless and anticyclonic situations were relatively frequent (*Table 2*). This category includes inter alia January 1972 (NAO = -0.52, Δt = -4.8 ºC), January 2006 (NAO = -0.10, Δt = -4.8 ºC), and February 1985 (NAO = -0.24, Δt = -7.4 ºC). All those months were dominated by days with circulation from the ES or NE-SE sectors (at least 20 days), and saw very few days or no days at all with SW-NW circulation (January 1972). One noteworthy fact is the characteristic, vast area of the negative temperature anomaly ($t \leq t_{av.}-2\sigma$) in February 1985, from Scandinavia to the Balkans and the Black Sea (*Fig. 4*).

In periods with negative NAO phase, there are also single months with an average temperature above the long-term mean (4 in total), but in none of those months did both these characteristics in question reach “high” levels. The 4 months saw high NAO- accompanied by slight Δt+ (0.2 – 1.9 ºC). The months saw a slight advantage of the number of days with NE-SE circulation (11 days) over SW-NW (8 days), but with a significant share of days with S circulation (6 days, *Table 2*). Thus, this group of months should rather be described as marked with a prevalence of circulation from the southern sector (SE-SW – an average of 15 days) over northerly circulation (NW-NE – 6 days – *Table 2*), even though in individual months, atmospheric circulation over Poland varied. For example, in January 1977 (NAO = -2.36, Δt = 0.7 ºC), circulation from the SE-SW sector occurred on 25 days (including 14 days with southern circulation) and NW-NE circulation on only 3 days, while in December 1989 (NAO = -2.23, Δt = 1.8 ºC), such circulation occurred on 11 and 10 days, respectively. A compact area with a positive temperature anomaly in the latter month was seen in the southwestern part of Europe (*Fig. 4*).

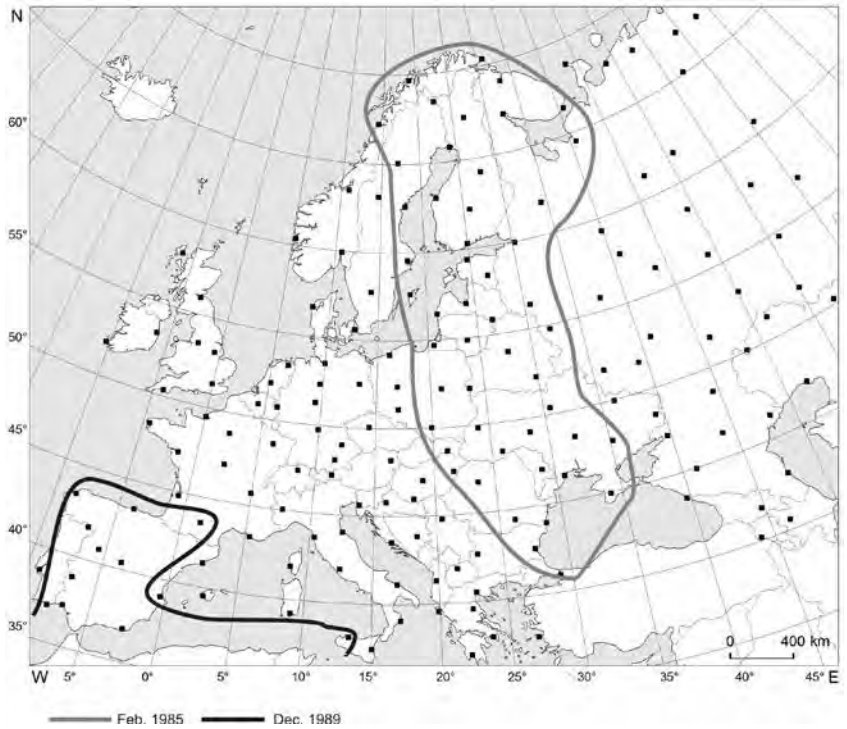

Fig. 4. Ranges of the positive and negative thermal anomalies during the negative NAO phase: December 1989 – NAO-/Δt+; February 1985 – (NAO-) /Δt- (explanations as for *Table 1*, the ranges are based on the publication by *Kossowska-Cezak* and *Twardosz* 2017).

4. Conclusions

Research into the relationship between the monthly thermal conditions in Warsaw and the monthly value of the NAO index in the winter months of 1951–2015 has led to several observations.

With a high positive value of the NAO index (at least 2.5), which is indicative of a strong westerly flow, central Europe is dominated by circulation from the western sector (SW-NW), with a negligible share or absence of circulation from the opposite sector. As a result of the advection of sea air masses in winter, temperatures over Poland are several degrees higher than the multiannual average (even by 5–6 ºC and more). In general, the greater the number of days with westerly circulation, the higher the temperature.

An equally high positive temperature deviation can also occur with a low NAO+ index values if the prevalence of western circulation over Poland is similar to that in months with high NAO+ (e.g., January 2007). Based on this, it can be concluded that values of the NAO index calculated on the basis of atmospheric pressure measured at specific points (which is necessary for comparison purposes) does not always reflect the actual intensity of westerly air mass transport controlled by the actual difference in pressure between the Azores High and the Icelandic Low.

When regional pressure systems form over Europe, thereby modifying the direction of advection of air masses reaching the central part of Europe, circulation from easterly directions and consequently temperatures below the long-term average may predominate in Poland despite the positive NAO phase (February 1954). This follows from the fact that average monthly temperatures clearly higher or lower than the long-term average show a better correspondence to the directions of advection over Poland than to the intensity of westerly air mass transport as expressed by the NAO index, even though the thermal characteristics of air masses are not only determined by the direction of their inflow.

As might be expected, months in the negative NAO phase see a more diverse circulation than those in the positive phase. Circulation from the western sector rarely occurs over Poland (on individual days) or does not occur at all, with easterly circulation gaining the advantage, which is, however, not so strong as that of circulation from the western sector in the positive phase. Cases of strong concentration of advection directions into a single sector for the whole month are rare and mainly observed in February (e.g., in February 1929, the coldest one in the 20th century ($t \leq t_{av.}-2\sigma$), when NE-SE circulation occurred on 24 days, NAO index = 0.27; *Kossowska-Cezak*, 1997).

The advection of air from the east and/or the north in those months translated into a negative temperature anomaly in central Europe at the time. In months with a lower predominance of circulation from the N-E-SE sector, the deviation of temperature below the long-term average tends to be lower, while in months with a lower NAO- index, the predominance of N-E-SE circulation may be significant, as a result of which air temperatures may be well below the long-term average (e.g., January 1972: NAO = -0.52, Δt = -4.8 ^{o}C; SE –15 days, S – 10 days, anticyclonic circulation – 20 days).

It should be noted here that, as a rule, months in the negative phase of the NAO distinguished by particularly low temperatures have a high share of circulation within an anticyclone, which is an indirect indication of the effect of cloudiness on thermal conditions in winter (night cooling through radiation during long cloudless nights).

In the negative NAO phase, temperatures above the long-term average may occur in Poland, which occurs when there is increased circulation from the

southern sector. However, the temperature deviation does not reach such values as in warm months during the positive phase of the NAO with westerly advection.

The analysis conducted in the present study confirms well-known regularities related to the impact of a strongly marked positive or negative NAO phases on the thermal conditions during Polish winters. However, it also reveals certain deviations from these regularities, which should be attributed to regional pressure systems over Europe, which control the advection within the territory of Poland and directly affect the thermal conditions here. At the same time, it must borne in mind that the direction of advection is not the sole determinant of the thermal characteristics of an incoming air mass.

References

Buchan, J., Hirschi, J.J.-M., Blaker, A.T., and *Sinha B.,* 2014: North Atlantic SST Anomalies and the Cold North European Weather Events of Winter 2009/10 and December 2010. *Mon. Weather Rev. 142*,922–932. https://doi.org/10.1175/MWR-D-13-00104.1

Castro-Díez, Y., Pozo-Vázquez, D., Rodrigo, F.S., and *Esteban-Parra, M.J.,* 2002: NAO and winter temperature variability in southern Europe.*Geophys. Res. Lett. 29*:1-1–1-4. https://doi.org/10.1029/2001GL014042

Cattiaux, J., Vautard, R., Cassou, C., Yiou, P., Masson-Delmotte, V., and *Codron, F.*, 2010: Winter 2010 in Europe: A cold extreme in a warming climate. *Geophys. Res. Lett. 37*, L20704. https://doi.org/10.1029/2010GL044613

Hirschi, J.J.-M., 2008: Unusual North Atlantic temperature dipole during the winter of 2006/2007. *Weather 63*,4–11. https://doi.org/10.1002/wea.120

Hirschi, J.J.-M. and *Sinha B.*, 2007: Negative NAO and cold Eurasian winters: How exceptional was the winter of 1962/1963? *Weather 62*, 43–48. https://doi.org/10.1002/wea.34

Hurrell, J.M., 1995: Decadal trends in North Atlantic Oscillation and relationship to regional temperature and precipitation. *Science 269*, 676–679. https://doi.org/10.1126/science.269.5224.676

Jones, P.D., Jonsson, T., and *Wheeler, D.,* 1997: Extension to the North Atlantic Oscillation using early instrumental pressure observations from Gibraltar and South-West Iceland. *Int. J. Climatol. 17*, 1433–1450. https://doi.org/10.1002/(SICI)1097-0088(19971115)17:13<1433::AID-JOC203>3.0.CO;2-P

Kossowska-Cezak, U., 1997: Miesięczne warunki termiczno-opadowe i ich zależność od cyrkulacji atmosferycznej. *Prace i Studia Geogr 20*,125 – 144. (in Polish)

Kossowska-Cezak, U. and *Twardosz, R.*, 2017: Anomalie termiczne w Europie (1951–2010). IGiGP UJ, Kraków. (in Polish) https://denali.geo.uj.edu.pl/publikacje,000225

Kossowska-Cezak, U. and *Twardosz, R.*, 2018: Uwarunkowania cyrkulacyjne temperatury powietrza w Warszawie w miesiącach o skrajnych wartościach wskaźnika NAO (1951-2015) *Prace Geograficzne 153*, 69–87. (in Polish). DOI 10.4467/20833113PG.18.004.8479

Lityński, J., 1969: Liczbowa klasyfikacja typów cyrkulacji i typów pogody dla Polski. *Prace PIHM 97*, 3–15. (in Polish)

Marsz, A.A., 2002: Wprowadzenie (istota NAO, historia, wskaźniki). In (eds. Marsz A.A and Styszyńska A.) Oscylacja Północnego Atlantyku i jej rola w kształtowaniu zmienności warunków klimatycznych i hydrologicznych Polski a temperatura powietrza nad Polską. Akademia Morska, Gdynia, 11–29. (in Polish)

Niedźwiedź, T., 2002: Relacje między NAO a wskaźnikami cyrkulacji nad Polską. In (eds Marsz A.A and Styszyńska A.) Oscylacja Północnego Atlantyku i jej rola w kształtowaniu zmienności

warunków klimatycznych i hydrologicznych Polski a temperatura powietrza nad Polską. Akademia Morska, *Gdynia*, 87–97. (in Polish)

Pianko-Kluczyńska, K., 2007: Nowy kalendarz typów cyrkulacji atmosfery według J. Lityńskiego, *Wiad Meteor Hydr Gosp Wodnej 4*:65–85. (in Polish)

Saunders, M.A. and *Lea, A.S.R.*, 2006: The 2005/06 UK and European winter: the UCL forecast and its assessment against observations. *Weather 61*,347–352. https://doi.org/10.1256/wea.183.06

Styszyńska, A., 2002: Wskaźniki NAO a typy cyrkulacji atmosferycznej Osuchowskiej-Klein. In (eds. *Marsz A.A* and *Styszyńska A.*) Oscylacja Północnego Atlantyku i jej rola w kształtowaniu zmienności warunków klimatycznych i hydrologicznych Polski a temperatura powietrza nad Polską. Akademia Morska, Gdynia, 99–109. (in Polish)

Wang, C., Liu, H., and *Lee, S-K.*, 2010: The record-breaking cold temperatures during the winter of 2009/2010 in the Northern Hemisphere. *Atmos. Sci. Lett. 11*,161–168. https://doi.org/10.1002/asl.278

Wibig, J., 2000: Oscylacja Północnoatlantycka i jej wpływ na kształtowanie pogody i klimatu. *Prze Geof 2*,121–137. (in Polish)

DOI:10.28974/idojaras.2020.1.6

IDŐJÁRÁS

Quarterly Journal of the Hungarian Meteorological Service
Vol. 124, No. 1, January – March, 2020, pp. 113–127

Characteristics of pollutants and their correlation to meteorological conditions in Hungary applying regression analysis

Georgina Nagy*, **Renáta Kovács**, **Szandra Szőke**, **Katalin Antalné Bökfi**, **Tekle Gurgenidze**, and **Ghada Sahbeni**

Institute of Environmental Engineering
Faculty of Engineering, University of Pannonia
10 Egyetem St., Veszprem, Hungary H-8200

**Corresponding Author e-mail: nagy.georgina@almos.uni-pannon.hu*

(Manuscript received in final form March 7, 2019)

Abstract— Air pollution occurs when harmful or excessive quantities of substances including gases, solid particulates, and biological molecules are introduced into the atmosphere. The analysis of the relationship between air pollutants and meteorological factors can provide important information about air pollution. The aim of this study is to examine and explore the relationship between the different monitored air pollutant concentrations such as carbon-monoxide (CO), nitrogen-oxides (NO_x), ozone (O_3), particulate matter (PM_{10}), and sulphur-dioxide (SO_2) and the selected meteorological factors such as wind speed, temperature, precipitation, and atmospheric pressure. The investigation is based on data observed during a 10-year-long measurement period (2004–2014) in the city of Veszprem located in the western part of Hungary, in the Transdanubia region. In the present research, regression analysis was the chosen statistical tool for the investigation. The analysis found that there is a moderate or a weak relation between the air pollutant concentrations and the meteorological factors.

Key-words: air quality, meteorological parameters, regression analysis, air pollutants, urban air

1. Introduction

As a consequence of anthropogenic activities of the last 50 years – such as public heating, transportation, and industrial activities – a diversity of waste compounds has been and is being released into ambient air. Thus, air quality has become a major and pressing issue to be considered in order to provide a livable environment. The spatial distribution (*Hiep et al.*, 2000; *Casado et al.*, 1994; *Harinath* and *Murthy*, 2010) and the temporal trends (*Mauro et al*., 2017; *Aynul et al*., 2016) of air pollutants allow the assessment of the air quality in cities. There is a special focus on metropolises such as Paris, Beijing (*Gros et al*., 2007), or New York (*Masiol et al*., 2017). Numerous previous studies (*Cuhadaroglu* and *Demirci*, 1997; *Chelani* and *Rao*, 2013; *Plaisance et al.*, 2004; *Luvsan et al.*, 2012; *Minarro et al.*, 2013; *Li et al.*, 2014; *Mahapatra et al*.,. 2014; *Rodrigez et al.*, 2013; *Wapler*, 2013) also pointed out the impact of various air pollutants on the urban environment and provided information on their association with weather conditions.

For example, in the research of *Chiu et al.*, (2005), it was presented that local meteorological parameters (such as solar radiation, wind speed, and wind direction) have an influence on O_3 and NO_2 concentrations. According to their research results, the concentration of O_3 were higher during the day – compared to night values – thanks to that there is a correlation between the ground level ozone concentration and the photochemical reactions. As stated in the findings of *Hargreaves et al.* (2000) there is a weak negative connection between the ambient NO_2 concentration and wind speed. *Xu* and *Zhu* (1994) found out, that in case of ozone, high concentrations are related to high pressure weather systems, low relative humidity, low cloudiness, light wind speed, and fog formation.

Several analytic methods are being used to find statistical relationship between meteorological parameters and air pollutants. Regression analysis, especially linear regression analysis is by far the most popular and well-known analytical method in the field of behavior-, social-, public health, and natural sciences, such as physics, chemistry, other engineering areas and countless other fields. This widely used analysis yields a mathematical equation – a linear model – that estimates a dependent variable Y from a set of predictor variables or regressors X. The analysis is extensively and broadly used and confirmed by many experiments in the works of several authors (e.g., *Xin*, 2009; *Darlington*, 2016; *Montgomery et al*., 2012). In this study, the regression analysis was conducted with the computer program IBM SPSS Statistics (SPSS), which offered advanced statistical capabilities and analytics to help to gain deep, accurate insights and understanding of the data providing better decision making.

In the presented study the authors studied the relationship between air pollutants concentration in the ambient air and the selected meteorological parameters based on regression analysis. Furthermore, the strength of the relationships was also determined.

2. Methodology

2.1. Study area

Veszprem is situated in the middle-western part of Hungary at 47°05’34” N and 17°54’49” E with the population of approximately 60,000 inhabitants. Hungary lies about halfway between the Equator and the North Pole, in the temperate zone, therefore, the weather is very changeable, mainly because it is influenced by the oceanic, continental, and the mediterranean climates. Thus, the annual average temperature in the city is approximately 10–12 °C (Central Transdanubia, 2017). Another important factors are the relief and the impact of the Carpathians, which is significant. The main contributors to air pollution in the city are public transport, private vehicles, public and domestic heating, and industrial activities (*Fig. 1*). Also, the impacts of the relief and the meteorological parameters are noticeable. Based on the air pollution index, the air quality in Veszprem is good (Air Quality Report, 2017).

Based on the data of the Hungarian Central Statistical Office (2017), there has been a visible increase of the number of registered vehicles in the studied period (*Fig. 2*). All these vehicles moving on the streets result traffic congestion problems in Veszprem, especially during the morning (06:00 – 08:00) and evening (16:00 –18:00) rush hours.

Fig. 1. Measurement area of the research project and its geographical location: (left) aerial view of the city (OpenStreetMap), (right) public transportation lines in the city (OpenStreetMap).

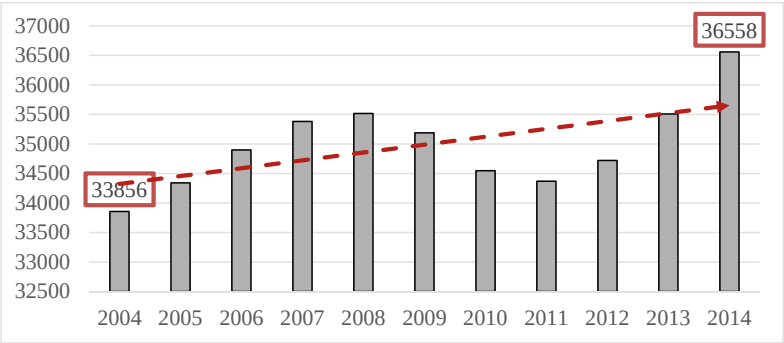

Fig. 2. Number or registered vehicles in the city of Veszprem between 2004 and 2014.

2.2. Meteorological data

For analyzing air quality, it is important to know the parameters that influence the ambient concentration of air pollutants. The selected relevant meteorological factors are the following: temperature (K); atmospheric pressure (hPa); wind speed (m/s), and precipitation (mm). The necessary meteorological data were supplied by the Institute of Radiochemistry and Radioecology of the University of Pannonia. The data were collected between 2004 and 2014. Their statistically processed version is shown in *Fig. 3*.

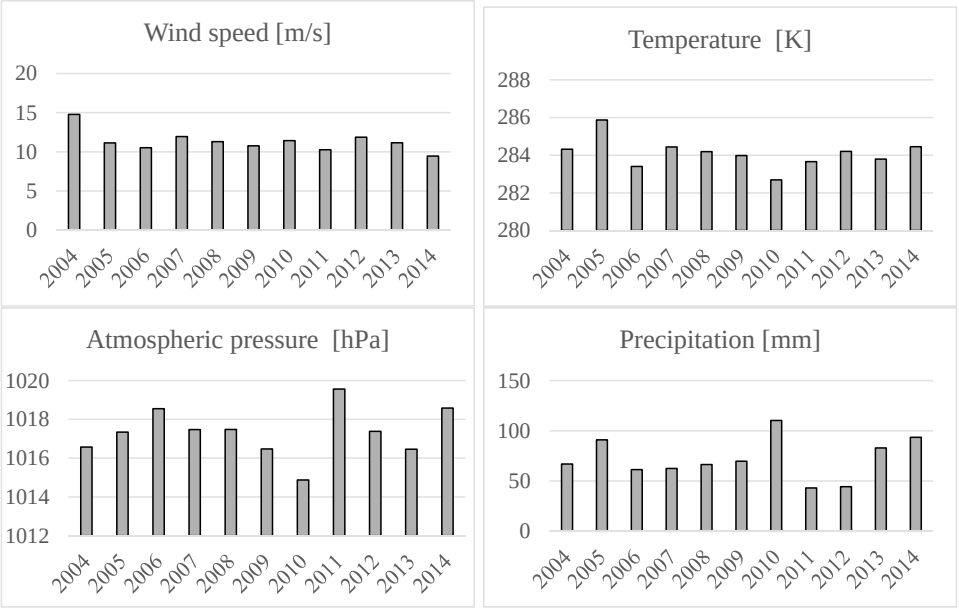

Fig. 3. Annual average values of meteorological parameters: (a) wind speed, (b) temperature, (c) atmospheric pressure, (d) precipitation.

2.3. *Collection of ambient air quality data*

The different air pollutants concentrations (CO, NO_x, O_3, PM_{10}, and SO_2) were obtained from the automatic monitoring network system of the Hungarian Air Quality Network (OLM). Data observed between 2004 and 2014 were used in this study. Statistically processed data are shown in the following figures (*Fig. 4*).

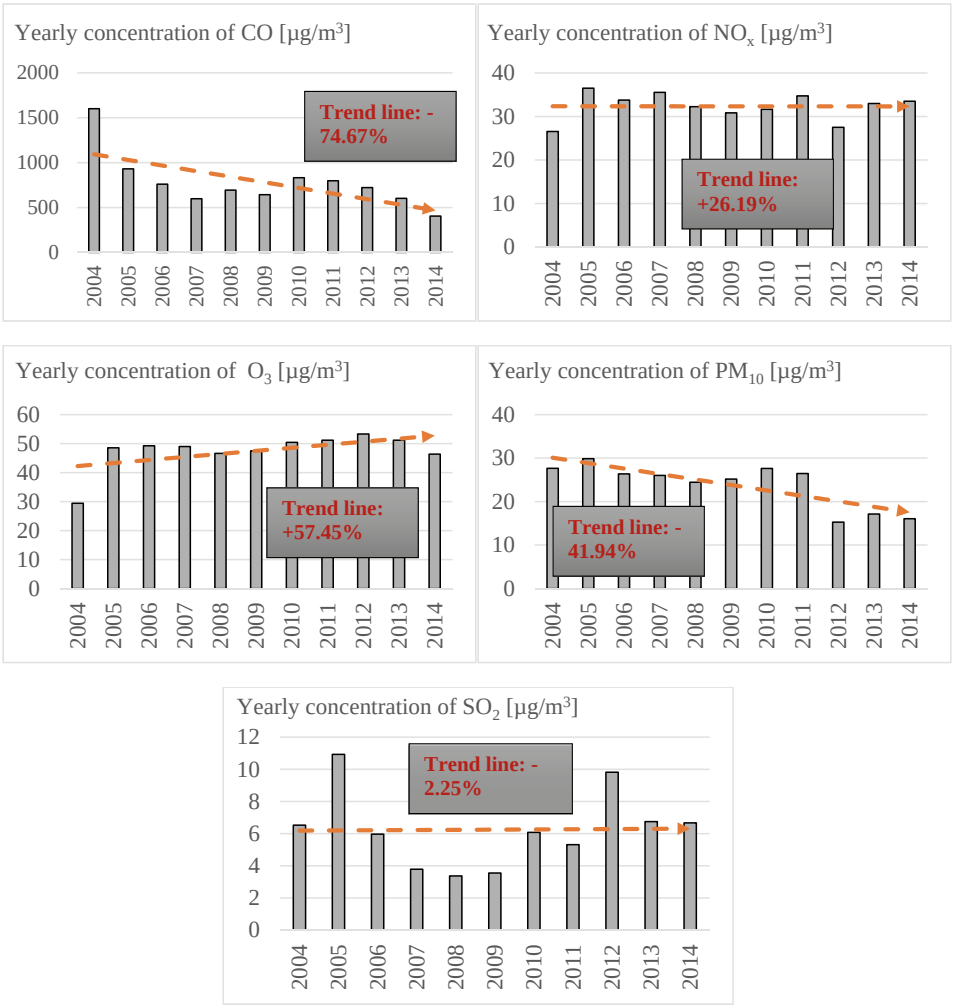

Fig. 4. Yearly average concentration of the measured air pollutants: (a) carbon-monoxide, (b) nitrogen-oxides, (c) ozone, (d) particulate matter, (e) sulphur-dioxide.

2.4. Regression analysis

To study the relationship between the variables, regression analysis was used according to *Douglas et al.* (2012), *Darlington* (2016), and *Xin (*2009). Statistical calculations have been used to analyze the extent to which the individual parameters such as temperature, solar radiation, wind direction, velocity, or relative humidity may be influenced by the concentration of different pollutants. The statistical method used is the regression calculation, also known as the correlation test. The essence is that we are looking for a relationship with a mathematical function between a dependent variable (result variable) and one or more explanatory variables. IBM SPSS Statistics has been used for the regression analysis. The following software outputs were used: summary tables, variance analysis tables, regression coefficients, and statistical test tables containing the results of the hypothesis test (F-test, sum of square deviations, degrees of freedom, T-test). According to the calculations, in each case *p* value was less than 0.0001, which means that the results are very significant.

3. Results

The interconnection between the meteorological parameters, such as wind speed, temperature, air pressure, and precipitation and the concentration of certain major air pollutants (CO, NO_x, O_3, PM_{10}, and SO_2) was examined by using linear regression analysis. By determining the linear correlation coefficient (R) – also called Pearson product moment correlation coefficient –, the strength and direction of a linear relationship between two variables were determined. The range of R was between –1 to +1, as shown in *Table 1*. The coefficient is symmetric. The closer the value to the endpoint the stronger the linear correlation, like in the case of CO concentration and wind speed (0.841). A perfect positive fit is achieved at R=+1, and a perfect negative fit is achieved at R=–1. On the contrary, if the value of R is close to 0, no or weak linear correlation can be determined meaning that there is a random, nonlinear relationship between the two variables, like in the case of SO_2 concentration and atmospheric pressure (0.011).

Table 1. Linear correlation coefficients of the selected parameters

R	**CO**	**NO_X**	**O_3**	**PM_{10}**	**SO_2**
Wind speed	**0.841**	0.635	0.723	0.277	0.074
Temperature	0.102	0.243	0.192	0.058	0.462
Atmospheric pressure	0.250	0.394	0.154	0.128	0.011
Precipitation	**0.870**	0.213	0.042	0.100	0.145
All meteorological parameters	0.884	0.740	0.862	0.344	0.490

Another tool of assessing relationships between variables is the coefficient of determinations (R^2) that gives the proportion of the variance of one variable being predictable from the other (*Table 2*). It is the ratio of the explained variation to the total variation. The coefficient of determination ranges from 0 to 1 and denotes the strength of the linear association between the selected variables. The value shows the ratio of the data that is the closest to the line of best fit. If R^2=1, the regression line goes through every single element of the scatter plot meaning that it approximates all of the data points. The farther a point is away from the regression line, the less variable can be explained.

Table 2. The coefficient of determinations of the selected parameters

R^2	**CO**	**NO_X**	**O_3**	**PM_{10}**	**SO_2**
Wind speed	0.7070	0.4027	0.5222	0.0766	0.0053
Temperature	0.0104	0.0589	0.0370	0.0034	0.2142
Atmospheric pressure	0.0623	0.1549	0.0238	0.0165	0.0000
Precipitation	0.0076	0.0452	0.0017	0.0099	0.0212
All meteorological parameters	0.7820	0.5470	0.7430	0.1180	0.2400

The analysis shows (*Fig. 5*) that in the examined period, the CO concentration is strongly affected by the wind speed. The determination coefficient is 0.707, which means that there is a strong relationship between those variables. Contrast with that, in case of other meteorological parameters, CO shows low values of R^2. Considering the relation between all meteorological parameters and the CO level, there is a high value (R^2=0.7820), therefore, the positive relation were demonstrated.

Furthermore, a moderate relation was observed in the case of the O_3 concentration (*Fig. 6*). The coefficient of determinations was a bit lower (R^2=0.5222), and the graph shows that between those two variables there is a negative linear correlation.

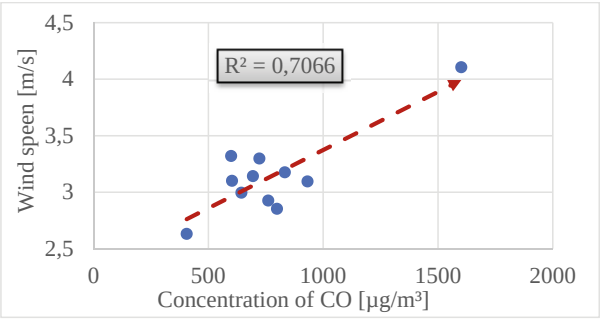

Fig. 5. Regression connection between the CO concentration and the wind speed.

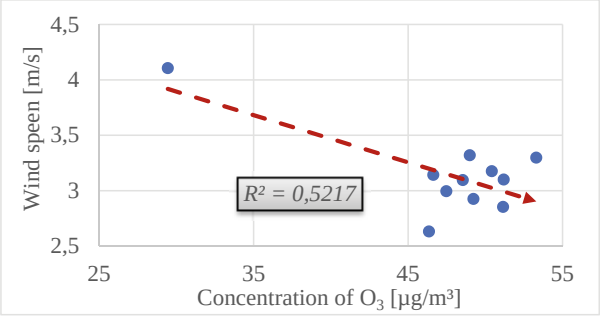

Fig. 6. Regression connection between the O_3 concentration and the wind speed.

Similar tendency was observed between the concentration of NO_x and the selected meteorological parameters (*Fig. 7*). The analysis confirmed a moderate relationship between the NO_x concentration and the wind speed (R^2=0.403). The relation of the NO_x and all meteorological parameters could be stated also as moderate (R^2=0.547).

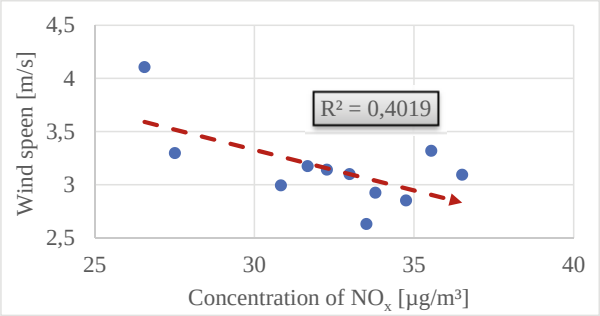

Fig. 7. Regression connection between the NO_x concentration and the wind speed.

Relations between the PM_{10} concentration and the meteorological parameters were week. The highest values of R^2 (*Fig. 8*) were noticed in the case of wind speed (R^2= 0.0766). The analysis demonstrated a positive connection, however, the coefficient of determination with all meteorological parameters were low (R^2= 0.1180).

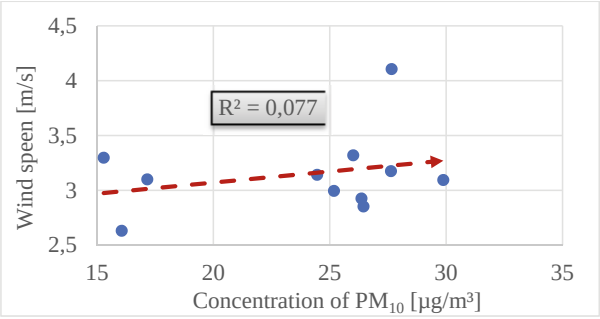

Fig. 8. Regression connection between the PM_{10} concentration and the wind speed.

Similarly, to PM_{10} low connection was observed in the case of SO_2 (*Fig. 9*). The highest determination coefficient value (R^2=0.2142) was between SO_2 and temperature. The strength of the relation between SO_2 and all meteorological parameters was low also (R^2=0.2400).

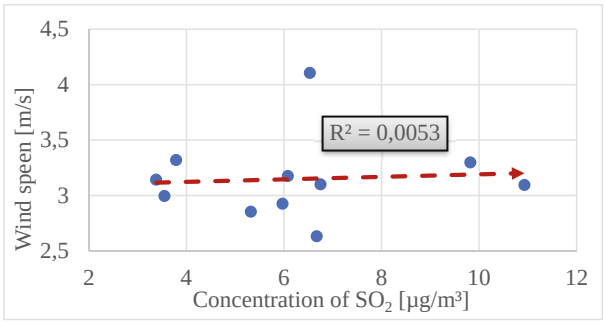

Fig. 9. Regression connection between the SO_2 concentration and the wind speed.

4. Discussion

In order to study the relationship between the CO, NO_x, O_3, PM_{10}, and SO_2 pollutants concentrations and the selected meteorological parameters, a linear regression analysis was carried out. The coefficient of the determinations (R^2) between the CO, NO_x, O_3, PM_{10}, and SO_2 pollutants concentrations and the meteorological parameters comparing with other scientific researches are shown in *Table 3*.

Table 3. The coefficient of determinations of the selected parameters in this study and in other studies

R^2	CO	NO_X	O_3	PM_{10}	SO_2
In this study	0.78	0.54	0.74	0.11	0.24
Sevda (2008)	0.48	0.28	0.75	*	*
Barrero et al. (2006)	*	*	0.67	*	*
Gupta et al. (2008)	*	0.05–0.49	*	0.16–0.64	0.23–0.75

*not measured components

In accordance with the previous scientific works it can be stated, that the number of meteorological parameters included in regression equations were variable, and the analyses of the meteorological parameters affecting concentrations of air pollutants were diverse also. A strong dependence was obtained by *Ocak* (2008), who determined a 75% coefficient that means the 75% of the O_3 concentration depends on the wind speed, temperature, and relative humidity, which is close to the research results of *Barrero et al.*, (2006) and also

to the results found in this study. Contrary to the research results of *Ocak* (2008), CO dependence was characterized by a strong relationship instead of a moderate one. In case of NO_x, the results were ranged on a wide spectrum (0.05 – 0.54), but not any case was detected stronger than moderate. *Gupta et al.* (2008) found the regression coefficients between PM_{10} and SO_2 levels and meteorological factors as 0.16 – 0.75, which differs greatly from our findings, which may be due to the fact, that their measurements were carried out in three different areas (one residential site, one commercial site, and one industrial site).

Besides the local emissions and meteorological conditions, the atmospheric long-range transport of pollutants influences the concentration field, too. For example, volcanic eruptions could have a significant effect on the SO_2 and SO_2^{-4} concentrations in air, as well as on the sulfur deposition. In 2014, a volcanic eruption started at the Barðarbunga fissure system in Iceland. There was little ash released in the eruption, but large amounts of SO_2 were emitted into the atmosphere. For better understanding the pollution level in Veszprém county, the data sets were compiled from existing results of the atmospheric chemistry transport model ran by the European Monitoring and Evaluation Programme under the Convention on Long-range Transboundary Air Pollution (CEIP, 2016). The emissions and the estimated deposition of SO_x and NO_x in Hungary are shown in *Table 4.*

Table 4. Emission and estimated deposition of SO_x and NO_x in Hungary [unit: Gg(S); Gg(N)]

	2005	**2006**	**2007**	**2008**	**2009**	**2010**	**2011**	**2012**	**2013**	**2014**
SO_x (emission)	41	39	35	35	30	31	34	31	29	27
NO_x (emission)	169	172	167	164	157	154	140	124	121	120
SO_x (deposition)	78	70	71	61	65	72	53	52	62	55
NO_x (deposition)	55	56	55	48	51	52	43	42	45	42

The spatial distribution and deposition from transboundary sources of SO_x and NO_x are visible in *Figs.10* and *11* (EMEP/MSC-W, 2014; *Gauss et al.*, 2016). The amount of emitted contaminants has changed in proportion to the level of emissions. It can also be stated that the county was less exposed to SO_x depletion, while it was exposed to NO_x pollution significantly.

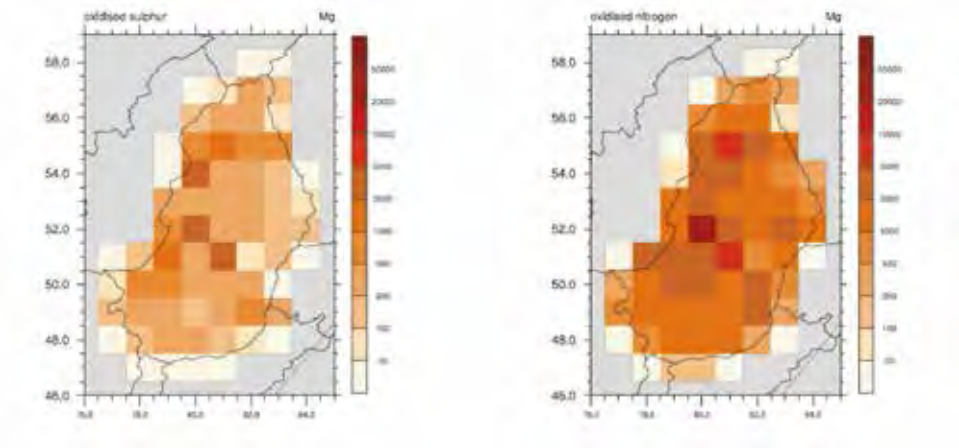

Fig. 10. The spatial distribution of SO_x and NO_x (emissions).

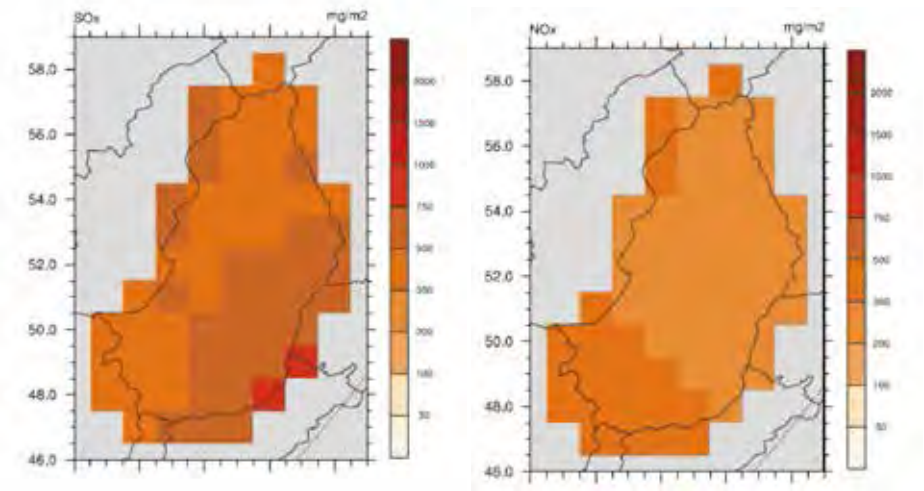

Fig. 11. Deposition from transboundary sources of SO_x and NO_x (unit: mg(S)/m^2, mg(N)/m^2).

5. Conclusion

The aim of the present study was to determine the relationship between the CO, NO_x, O_3, PM_{10} and SO_2 pollutants concentrations and selected meteorological parameters (wind speed, temperature, air pressure, and precipitation). It was not observed a significant change in the terms of the selected meteorological

parameters in Veszprem between 2004 and 2014. Variability of the values of wind speed, air pressure, and wind direction were not significant considering either the averages or the maximums or minimums. More extreme values were observed in the evolution of precipitation and temperature. In 2005, 2010, and 2014, the precipitation extremes were more significant than in the other years. It was noticeable, that among those years there were greatly drier years than the others, especially in 2011 and 2012. The temperature values were concerned too, and it has been found that there were a few outliers among the minimum and maximum values. The variability of averages was low. In the examined period, the highest and lowest values occured in the year of 2006. The concentration of air pollutants decreased between 2004 and 2014, except for concentration of nitrogen-dioxide and ozone. The main source of those air pollutants were transportation, which is determinative in Veszprem. The connection between the air pollutants and the meteorological parameters were demonstrated by regression analysis. The level of the relationship depends on the type of air pollutant and the meteorological parameter. The concentration of air pollutants were highly affected by the wind speed, since this parameter promotes the mixing and dilution of the pollutants. Among the analyzed parameters, CO and O_3 indicate high determination values (>70%). In the case of the other pollutants, the low determination coefficient values could be explained by the low average annual emissions.

Acknowledgment: This study was supported by the Institute of Environmental Engineering and by the Institute of Radiochemistry and Radioecology of the University of Pannonia.

References

Air Quality Report, 2017: Air Quality Reports of the settlements based on the Hungarian Air Quality Monitoring Network. Hungarian Air Quality Monitoring Network – Reports Available: http://www.levegominoseg.hu/reports (Accessed 13.01.2017)

Aynul, B., Warren, B. Kindzierski 2016: Evaluation of air quality indicators in Alberta, Canada – An international perspective. *Environ. Int. . 92*, 119–129 https://doi.org/10.1016/j.envint.2016.03.021

Barrero, M.A., Grimalt, J.O., and *Canto, L.,* 2006: Prediction of daily ozone concentration maxima in the urban atmosphere. *Chemometr. Intell. Lab. Sys. 80*, 67–76 https://doi.org/10.1016/j.chemolab.2005.07.003

Casado LS, Shahrokh Rouhani, Carlos A. Cardelino, Adrian J. Ferrier, 1994: Geostatistical analysis and visualization of hourly ozone data, *Atmos. Environ. . 28*, . 2105–2118 https://doi.org/10.1016/1352-2310(94)90477-4

CEIP, 2016: Officially reported emission data

Országos Területfejlesztési és Területrendezési Információs Rendszer (TeIR) Available: http://www.terport.hu/regiok/magyarorszag-regioi/kozep-dunantuli-regio (Accessed 13.01.2017)

Casado, L.S., Rouhani, S., Cardelino, C.A., and *Ferrier A.J.* 1994: Geostatistical analysis and visualization of hourly ozone data. *Atmos. Environ. 28*, 2105–2118. https://doi.org/10.1016/1352-2310(94)90477-4

Chelani, A.B. and *Rao, P.S.* 2013: Temporal variations in surface air temperature anomaly in urban cities of India. *Meteorol Atmos Phys 121*, 215. https://doi.org/10.1007/s00703-013-0262-8

Chiu, K.H., Sree, U., Tseng, S.H., Wu, C-H., Lo, J-G., 2005: Differential optical absorption spectrometer measurement of NO2, SO2, O3, HCHO and aromatic volatile organics in ambient air of Kaohsiung Petroleum Refinery in Taiwan. *Atmos. Environ. 39,* 941–955. https://doi.org/10.1016/j.atmosenv.2004.09.069

Cuhadaroglu, B. and *Demirci, E.* 1997: Influence of some meteorological factors on air pollution in Trabzon city. *Energ. Build.25,* 179–184. https://doi.org/10.1016/S0378-7788(96)00992-9

Darlington, R.D., 2016: Regression Analysis and Linear Models (Methodology in the Social Sciences). 1 Edition. The Guilford Press.

EMEP/MSC-W, 2014: EMEP MSC-W modelled air concentrations and depositions. Available: http://www.emep.int/mscw/index.html (Accessed: 25.02.2019)

Gauss, M., Nyíri, A., Benedichtow, A., and *Klein, H.* 2016: Transboundary air pollution by main pollutants (S, N, O3) and PM – Hungary. MSC-W, ISSN:1890 - 0003

Gros, V., Sciare, J. and *Yu, T.,* 2007: Air-quality measurements in megacities: Focus on gaseous organic and particulate pollutants and comparison between two contrasted cities, Paris and Beijing. *Comp. Rendus Geosci. 339,* 764-774. https://doi.org/10.1016/j.crte.2007.08.007

Gupta, A.K., Karar, K., Ayoob, S., and *Kuruvilla, J.,* 2008: Spatio-temporal characteristics of gaseous and particulate pollutants in an urban region of Kolkata, India. *Atmos. Res. 87,* 103–115. https://doi.org/10.1016/j.atmosres.2007.07.008

Hargreaves, P.R., Leidi, A., Grubb, H.J., Howe, M.T., and *Mugglestone, M.A.,* 2000: Local and seasonal variations in atmospheric nitrogen dioxide levels at Rothamsted, UK, and relationships with meteorological conditions. *Atmos. Environ. 34, 843–853.* https://doi.org/10.1016/S1352-2310(99)00360-X

Harinath, S. and *Murthy, U.N.,* 2010: Spatial distribution mapping for air pollution in industrial areas – a case study, *J. Industr. Poll. Cont. 26,* 217–220.

Hiep, Duc, Shannon, I., Azzi, M., 2000: Spatial distribution characteristics of some air pollutants in Sydney. *Math. Comput. Simulat. 54,* 1–21. https://doi.org/10.1016/S0378-4754(00)00165-8

Hungarian Central Statistic Office, 2017: Stock of Road transport. Available: http://www.ksh.hu/transportt (Accessed 14.01.2017)

Li, L., Qian, J., Ou, C., Zhou, Y., Guo, C., and *Guo, Y.,* 2014: Spatial and temporal analysis of Air Pollution Index and its timescale-dependent relationship with meteorological factors in Guangzhou. China. 2001–2011. *Environ. Pollut. 190,* 75–81. https://doi.org/10.1016/j.envpol.2014.03.020

Luvsan, M.E., Shie, R.H., Purevdorj, T., Badach, L., Baldorj, B., and *Chan, C.C.* 2012: The influence of emission sources and meteorological conditions on SO2 pollution in Mongolia. *Atmos. Environ. 61,* 542–549. https://doi.org/10.1016/j.atmosenv.2012.07.044

Mahapatra, P.S., Panda, S., Walvekar, P.P., Kumar, R., Das, T., and *Gurjar, B.R.,* 2014: Seasonal trends. meteorological impacts. and associated health risks with atmospheric concentrations of gaseous pollutants at an Indian coastal city. *Environ. Sci. Pollut. Res. 21,* 11418–11432. https://doi.org/10.1007/s11356-014-3078-2

Masiol, M., Hopke, P.K., Felton, H.D., Frank, B.P., Rattigan, O.V., Wurth, M.J., and *LaDuke, G.H.,* 2017: Analysis of major air pollutants and submicron particles in New York City and Long Island. *Atmos. Environ. 148,* 203–214. https://doi.org/10.1016/j.atmosenv.2016.10.043

Minarro, M.D., Ferradas, E.G., Martinez, F.J.M., 2013: Influence of temperature changes on ambient air NO(x) chemiluminescence measurements. *Environ. Monit. assess. 184,* 5669–5678. https://doi.org/10.1007/s10661-011-2372-4

Montgomery, D.C., Peck, E.A., and *Vining, G.,* 2012: Introduction to Linear Regression Analysis. John Wiley & Sons.

Ocak, S. and *Turailoglu, F.S.* 2008: Effect of Meteorology on the Atmospheric Concentrations of Traffic-Related Pollutants in Erzurum, Turkey. *J. Int. Environ. Appl. Sci. 3,* 325–335.

Plaisance, H., Piechocki-Minguy, A., Garcia-Fougue, S., and *Gallo, J.C.,* 2004: Influence of meteorological factors on the NO_2 measurements by passive diffusion tube. *Atmos. Environ. 38.,* 573–580. https://doi.org/10.1016/j.atmosenv.2003.09.073

Rodríguez, R., Casas, M.C., and *Redaño, A.*, 2013: Multifractal analysis of the rainfall time distribution on the metropolitan area of Barcelona (Spain). *Meteorol. Atmos. Phys. 121*, 181. https://doi.org/10.1007/s00703-013-0256-6

Wapler, K., 2013: High-resolution climatology of lightning characteristics within Central Europe. *Meteorol. Atmos. Phys. 122*, 175. https://doi.org/10.1007/s00703-013-0285-1

Xin, Y., 2009: Linear Regression Analysis: Theory and Computing. 1 Edition. World Scientific Publishing Company.

Xu, J. and *Zhu, Y.*, 1994: Some characteristics of ozone concentrations and their relations with meteorological factors in Shangai. *Atmos. Environ. 28*, 3387–3392. https://doi.org/10.1016/1352-2310(94)00154-D

DOI:10.28974/idojaras.2020.1.7

IDŐJÁRÁS

Quarterly Journal of the Hungarian Meteorological Service
Vol. 124, No. 1, January – March, 2020, pp. 129–141

Statistical and geostatistical analysis of spatial variation of precipitation periodicity in the growing season

Elżbieta Radzka* and **Katarzyna Rymuza**

Faculty of Agrobioengineering and Animal Husbandry
Siedlce University of Natural Sciences and Humanities
ul. Prusa 14, 08-110 Siedlce, Poland

**Corresponding Author e-mail: elzbieta.radzka@uph.edu.pl*

(Manuscript received in final form April 25, 2019)

Abstract— This work presents the variation in the spatial distribution of atmospheric precipitation determined by means of multidimensional analyses. Precipitation data observed at nine stations of the Institute of Meteorology and Water Management (IMGW) located in central-eastern Poland in the period 1971–2005 are analyzed. Precipitation periodicity index was calculated for each station (measurement point). The index was subjected to descriptive analysis by calculating the average value for the long-term period and the average rate of change. Multidimensional analyses were used to examine the spatial differentiation of precipitation variation. Periodicity indexes in months associated with the first and second principal component were found to account for over 70% variation between the measurement points. The months were as follows: April, May, July, and October. Cluster analysis was performed based on principal components, and it yielded three groups of measurement points with different distribution of precipitation periodicity indexes. The first group consisted of localities characterized by a low precipitation periodicity index in July and October. The second cluster included measurement points which had the lowest precipitation periodicity in May, June, August, and September. The third cluster was formed by only one locality (Białowieża), whose precipitation periodicity index was the highest in every month of the growing season. Both principal component analysis and cluster analysis may be used for an assessment of spatial variation of precipitation periodicity. Their results agree with findings based on the method of isoline interpolation.

Key-words: precipitation periodicity index, multidimensional analysis, variation, spatial distribution

1. Introduction

Atmospheric precipitation is a basic element of climate, which is characterized by substantial temporal and spatial variations. The literature on the subject contains many parameters which describe this phenomenon, and suggests numerous methods of determining their variation (*Friederichs,* 2010*; Huang et al.,* 2018; *Łupikasza,* 2001; *Miler,* 2018; *Nikulin,* 2011).The annual distribution of atmospheric precipitation in the zone of temperate latitudes is commonly believed to be their most important characteristic. Poland has a temperate climate which is changeable, uneven and characterised by, among others, spatial and temporal precipitation variation *(Paul* and *David,* 2006; *Twardosz et al.,* 2011; *Żarski* and *Dudek,* 2000).

Precipitation distribution varies throughout the growing season, and the same season of the year may see many days without rain or longer periods of excessive rainfall (*Dzieżyc et al.,* 2012). Spatial and temporal changes in precipitation distribution negatively affect agriculture, afforestation, and water reserves. As the frequency of extreme phenomena has been on the increase in recent years, much more attention is paid to precipitation at present. Scientists all over the world have raised the subject of precipitation variation for many years, particularly in the context of climate change and increased frequency of weather anomalies (*Banaszkiewicz et al.,* 2004; *Olechowicz – Bobrowska et al.,* 2005, *Paul* and *David,* 2006).

Progressing warming is an empirically confirmed symptom of climate change. The warming, which is most evident in spring, is not accompanied by statistically significant changes in the amount of precipitation (*Ziernicka-Wojtaszek et al.,* 2015; *Żmudzka,* 2009). Modern climatic forecasts, including research by IPCC experts (2007), indicate that central Europe will see an increase in the winter precipitation and a decline in the summer rainfall. Precipitation conditions in Poland have changed in the last 50 years as well. A decline in the proportion of summer (June-August) precipitation sum in the annual sum has been observed. According to *Degirmendžić et al.* (2004) and *Zawora* and *Ziernicka* (2003), the main features of the continental climate are becoming less and less pronounced. Variation in precipitation is to a great extent the result of the effect of atmospheric circulation, which favours continental or oceanic influences and thus impacts the climate at a global and local scale (*Twardosz et al.,* 2011).

In meteorology and climatology, spatial analysis is almost exclusively based on measurements taken at certain points − mainly various types of meteorological stations. As a result, the analysis requires that the data collected at these points are transformed into surfaces of certain meteorological elements. The spatial distribution of precipitation types in Europe, particularly in the Mediterranean area, is well known. However, little attention has been paid in literature to the long-term variation of this precipitation characteristics.

The objective of this work was to analyze the variation in one of the indicators of annual precipitation variation (irregularity index) in the central-eastern part of Poland by means of multidimensional analyses.

2. Materials and methods

2.1. Study area

The present work draws on data on daily atmospheric precipitation sums for the period 1971–2005 obtained from nine IMGW stations located in the central-eastern part of Poland (*Table 1* and *Fig. 1*).

According to *Woś* (1993), the study area belongs to the 19th Polish climatic region − the Podlasie-Polesie region. Compared with other climatic regions in Poland, the number of days with moderately warm and cloudy weather in the area is low − around 70 days per year. The number of moderately warm days with precipitation is about 55 per year, and the number of moderately warm, cloudy days with precipitation is only 26 per year. The days when the weather is rather frosty and sunny without precipitation are more frequent than in other regions.

*Table 1.*Geographic coordinates of synoptic and climatic IMGW stations in central-eastern Poland

Station	**Geographic coordinates**		**H_s m a.s.l.**
	φ	**λ**	
Ostrołęka	53 º 05’	21 º 34’	95
Białowieża	52 º 42’	23 º 51’	164
Włodawa	51 º 33’	23 º 32’	163
Szepietowo	52 º 51’	22 º 33’	150
Legionowo	52 º 24’	20 º 58’	93
Biała Podlaska	52 º 02’	23 º 05’	133
Sobieszyn	51 º 37’	22 º 09’	135
Pułtusk	52 º 44’	21 º 06’	95
Siedlce	52 º 11’	22 º 16’	146

Explanations: φ – latitude, λ – longitude, H_s – elevation above sea level.

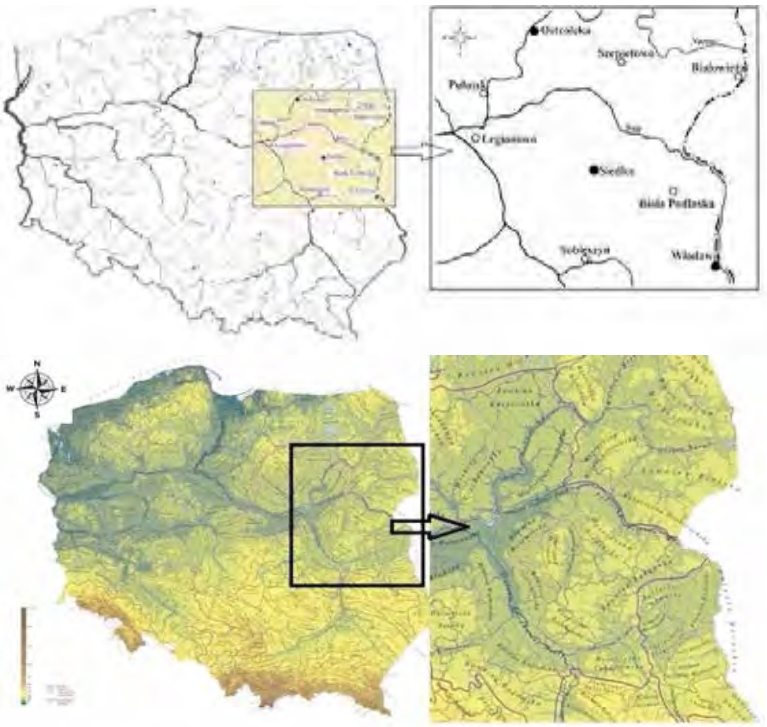

Fig. 1. Location of the meteorological stations included in the study.

2.2. Meteorological analysis

The following parameters were calculated for each station:

- the average atmospheric precipitation sum for the growing season (April-October) through the long-term period,
- the monthly atmospheric precipitation sum for the growing season (April-October), and
- the monthly index of precipitation periodicity in the growing season (April-October).

The precipitation periodicity index is a general characteristics of the precipitation continentality which suitably reflects the degree of the development of land-related precipitation characteristics in areas of temperate latitudes (*Woś*, 1993).

The precipitation periodicity index is calculated according to the following formula:

$$W = (\Sigma \left| mi - Rs \right| * 100)/R, \quad (1)$$

where *mi* is the average precipitation in the *i*th month, *R*s is the average precipitation sum for the studied period, and *R* is the precipitation sum for the studied period.

The index of precipitation periodicity may range from 0 to about 183%. Based on the value of the *W* index, *Wilgat* (1948) distinguished the following precipitation types:

- fairly even precipitation, when *W* is less than 25%,
- slightlyperiodic precipitation, when *W* is between 25–50%,
- clearly periodic precipitation, when *W* is between 50–75%,
- distinctly periodic precipitation, when *W* is between 75–100%, and
- extremely periodic precipitation, when *W* is more than 100%.

Schulze (1956) termed the above indicator the annual distribution index, whereas *Chromow* (1977), who used the unitless parameter (not percentages), called it the periodicity index. According to *Kożuchowski* and *Wibig* (1988), such a formula should be termed the non-proportionality index. *Walsh* and *Lawler* (1981) used this parameter to develop maps of seasonal precipitation variation in the tropical Africa, the British Isles, Brazil, and India.

2.3. Geostatistical analysis

The spatial interpolation of precipitation periodicity was based on the kriging method. A few types of kriging can be distinguished based on the detailed calculation used by the algorithm, from which the ordinary kriging is the most popular. Many traditional climatological approaches accept it as the only spatial interpolation method. The description of kriging can be found in many works, including textbooks on individual geostatistical programs. In generally, kriging assumes that there is internal stationarity in the whole spatial process. Explaining values (variables) are based on linear equations calculated from observed data accompanied by corresponding weights. The weights depend on the spatial correlation which exists between these points. Linear coefficients are determined so that the estimated variance error is the lowest (the so-called kriging variance). Due to this, kriging is believed to be the most universal method of spatial analysis.

2.4. Statistical analysis

Multi-dimensional principal component analysis (PCA) and cluster analysis were carried out to compare the measurement points in terms of precipitation periodicity. The principal component analysis is a dimension reduction technique, which transforms the original correlated variables into new, non-correlated

variables called principal components. They maximally explain the total variance of a group of p primary variables $x_1, \ldots, x_p$, that is

$$\sum_{j-1}^{p} S_j^2 = tr\ (S), \tag{2}$$

where S is the covariance matrix for a sample, tr is the trace of the matrix, and s_j^2 is the variance of the variable x_j, $j = 1, \ldots, p$ (*Krzyśko,* 2010).

The number of components considered was selected based on the Kaiser's criterion, according to which only the variables with the value of more than 1 are analyzed. Such components carry only the most significant information which reflects the variation of the objects, thus they were used in the second part of the analysis, in the cluster analysis. Euclidean distance was used as a measure of distance between objects and Ward's procedure as an agglomeration method. The intersection point was determined applying the Mojena's rule:

$$d_{i+1} > \bar{d} + ks_d, \tag{3}$$

where $\bar{d}$ is the mean value, s_{d} is the standard deviation d_i, and k is a constant value = 1.25 (*Milligan* and *Cooper*,1985).

Statistical analysis was performed using Statistica 12.0 PL for Windows.

3. Results and discussion

The highest atmospheric precipitation sum for the growing season in central-eastern Poland was recorded in 1974 (630 mm), while the lowest in 1982 (248 mm) (*Fig. 2*). In Białowieża, the precipitation sum spanning from April to October declined by as much as 48 mm per 10 years, on average. The precipitation for the April-October period dropped by less than 10 mm per 10 years only in Pułtusk. Many authors confirmed that precipitation patterns have been changing both in Poland and Europe (*Boryczka* and *Stopa –Boryczka*, 2004; *Mousavi et al.,* 2018; *Pauling et al.,* 2005).

The yearly atmospheric precipitation sum in the study area was primarily affected by the location of the measurement point. It was the highest (610 mm) in the north (Białowieża) and the lowest (518 mm) in the south (Włodawa). A similar relationship was found for the growing season. The sum for April-October was the highest in the north and amounted to 414 mm in Białowieża and 410 mm in Ostrołęka. At the remaining points, the precipitation sum did not exceed 400 mm throughout the growing season. In Poland, substantial differences between precipitation amounts are recorded even in relatively small areas (*Banaszkiewicz et al.,* 2004, 2008). Precipitation unevenness, analyzed on the basis of periodicity indexes, was also confirmed by *Paul* and *David* (2006).

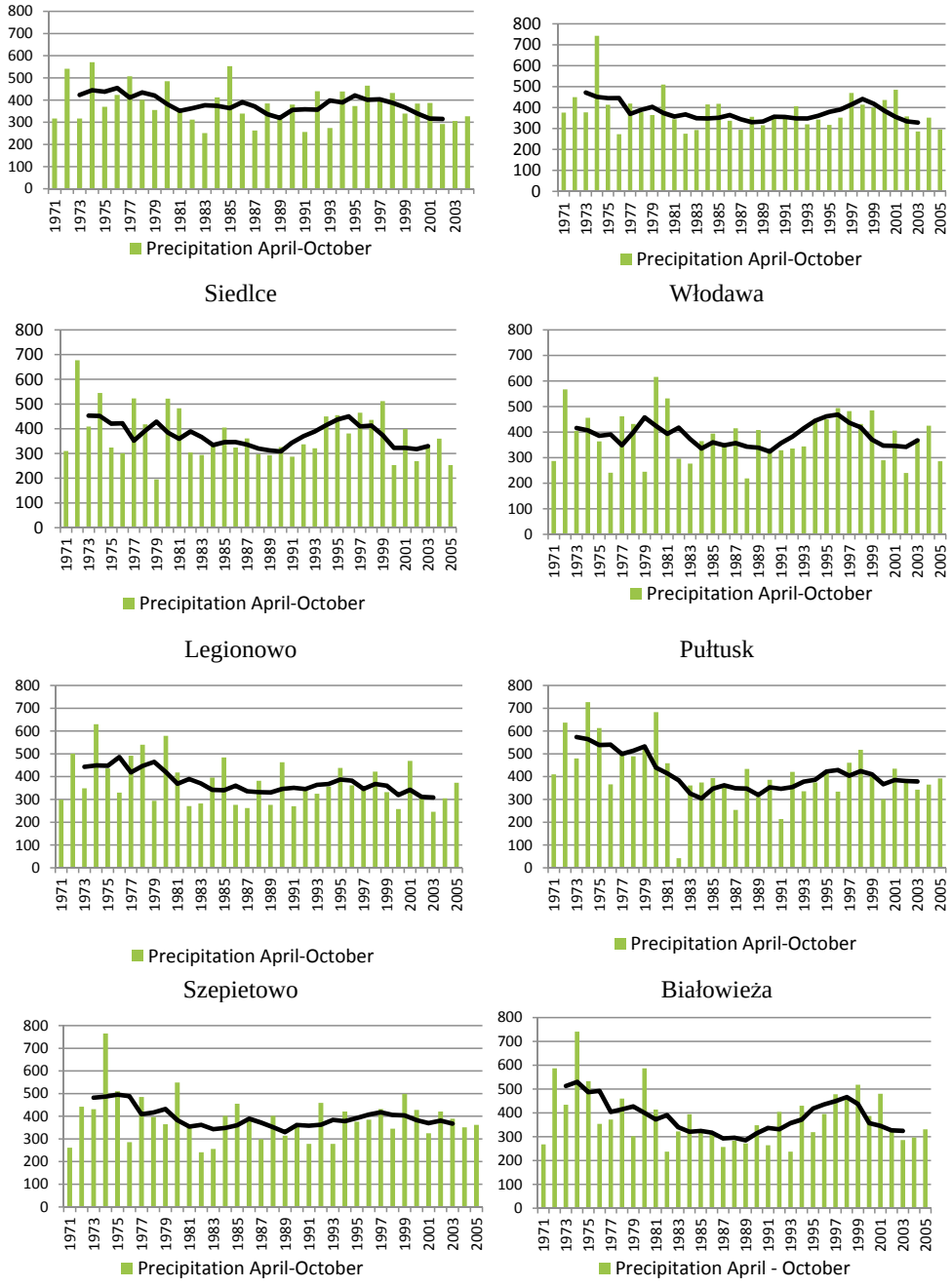

Fig. 2. Atmospheric precipitation sums for the growing season (April-October) and the 5-year moving average in central-eastern Poland from 1971 to 2005.

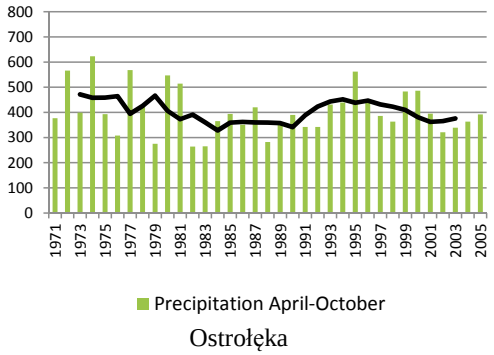

Fig. 2. Continued

In the study area, average values of precipitation variation index ranged from 42% in Włodawa to 48% in Szepietowo. The average area values of this parameter in individual months of the growing season ranged from 35% in May to 61% in October. According to *Czarnecka* and *Nidzgorska-Lencewicz* (2012), the greatest spatial and temporal variations in precipitation occur in autumn. *Marosz et al.*, (2013) claim that spatial variation of the average value (from 1971 to 1990) of the 90th percentile of daily precipitation sums shows relatively low variation, while seasonal and monthly values are cyclic. The sum of the monthly precipitation tended to change significantly in August in Koszalin, and a seasonal trend of precipitation change was observed only in the cool season of the year in Poznań (*Skowera et al.*, 2014).

In central-eastern Poland, only two types of precipitation periodicity (slightly and clearly periodic) were found in the growing season of the long-term period studied (*Fig. 3*).

Analysis of the periodicity index revealed that at each measurement point, precipitation was slightly periodic in April, May, September (excluding Włodawa), and October, and clearly periodic in June and July. Precipitation periodicity in August depended on the measurement point and was clearly periodic for five points, and poorly periodic for four locations. According to *Wilgat* (1948), precipitation in Europe is quite even compared with other areas in the world resulting from a strong impact on the Atlantic. The yearly precipitation pattern becomes surprisingly smooth in eastern and south-eastern Europe, although continental properties of precipitation should strengthen eastwards − precipitation should be higher in the summer season. Probably, precipitation concentration declines in eastern Europe due to a general shortage of and seasonal fluctuations in water vapor transportation (*Łupikasza*, 2001). Variation in precipitation results from the effect of atmospheric circulation, which is behind the domination of continental or oceanic influences (*Tylkowski* and *Hojan*, 2018).

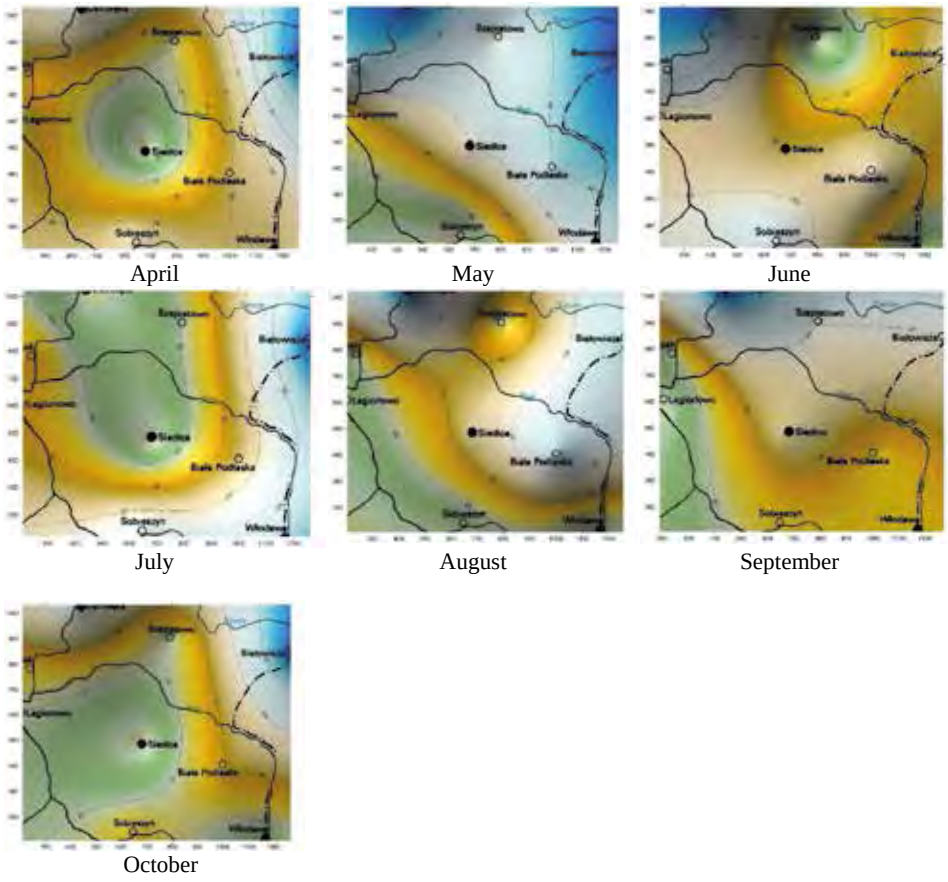

Fig. 3. Distribution of atmospheric precipitation periodicity types in the growing season in central-eastern Poland.

Łupikasza (2001) observed that the precipitation periodicity index was constantly on the increase mainly in western Europe (the British Isles, Denmark, western France), Romania, and some stations located in the east of Europe, whereas in central Germany, south-eastern France and southern Norway the opposite trend was observed (the index *W* was constantly on the decline).

Principal component analysis demonstrated that the first two principal components accounted for over 70% of variation in the types of precipitation periodicity between measurement points (*Table 2*). The precipitation periodicity index for April, May, and October had the greatest influence on spatial variation, as indicated by correlation coefficients between the first principal component and the indicators analyzed. The second principal component was the most strongly correlated with precipitation periodicity in July, and accounted for over 20% of variation between measurement points.

Table 2. Factor loads, eigenvalues, and proportion of the total variance of precipitation periodicity index, as explained by the first two principal components

Characteristics	PC1	PC2
X1 – periodicity index in April	-0.827	-0.441
X2 – periodicity index in May	-0.837	0.186
X3 – periodicity index in June	-0.734	0.194
X4 – periodicity index in July	-0.420	-0.874
X5 – periodicity index in August	-0.683	0.272
X6 – periodicity index in September	-0.726	0.340
X7 – periodicity index in October	-0.827	-0.441
Eigenvalue of principal components	3.09	1.22
Explainded proportion of the total variance (%)	51.53	20.33
Comulative proportion of the total variance (%)	51.53	71.87

Measurement points were divided into three groups based on cluster analysis (*Fig. 4*).

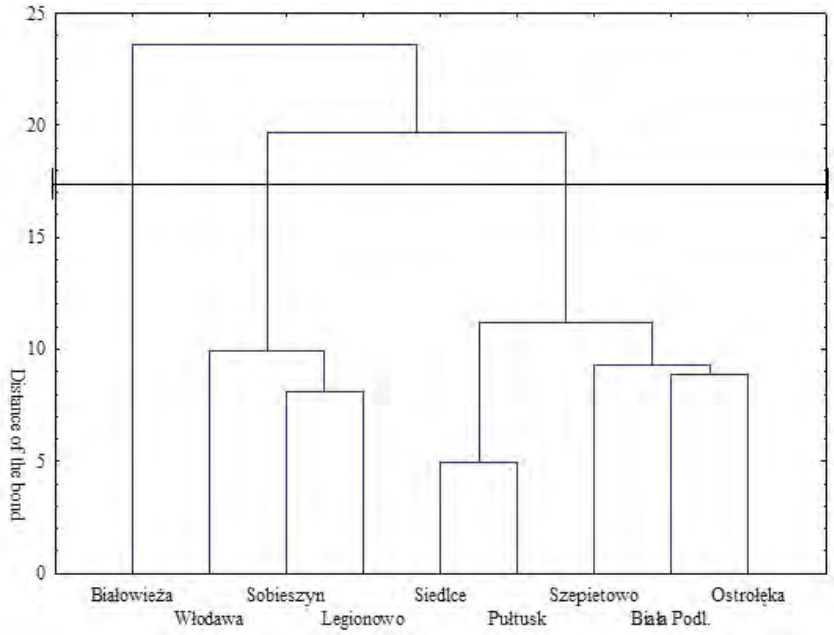

Fig. 4. Dendrogram for nine measurement points obtained for the first two principal components.

The first group included stations located in Siedlce, Pułtusk, Szepietowo, Biała Podlaska, and Ostrołęka. The second group included stations situated in Włodawa, Sobieszyn, and Legionowo, while the Białowieża station is the only object in the third group.

The region represented by stations in cluster 1 had a low periodicity index in July and October. The region formed by points from cluster 2 was characterized by the lowest periodicity index in May, June, August, and September. Cluster 3 with only Białowieża in it had the highest precipitation periodicity index in every month of the growing season (*Table 3*).

Table 3. Average values of precipitation periodicity index in the three clusters

Characteristic	Cluster 1	Cluster 2	Cluster3
April	36.358	36.910	44.260
May	54.290	49.710	59.480
June	70.628	67.530	77.200
July	70.226	74.790	80.680
August	63.452	58.083	65.870
September	55.840	54.070	58.500
October	36.358	36.910	44.260

Principal component analysis and cluster analysis may be used for an assessment of spatial variation of precipitation periodicity, because their results agree with the results of the isoline interpolation method.

4. Conclusions

1. Average values of precipitation periodicity index ranged from 42 to 61%, and in the period 1971–2005, only two types of it were observed: the slightly and the clearly periodic precipitation.

2. The index of precipitation periodicity in April, May, and October had the greatest influence on the differences between the analyzed locations.

3. Based on cluster analysis, the study area was divided into three groups. The first cluster comprised stations in Siedlce, Pułtusk, Szepietowo, Biała Podlaska, and Ostrołęka, which had low precipitation periodicity indexes in July and October. The second cluster, formed by stations located in

Włodawa, Sobieszyn, and Legionowo, was characterized by the lowest precipitation periodicity in May, June, August, and September. Białowieża, which was the sole object in the third cluster, had the greatest precipitation periodicity in almost all of the months.

4. Principal component analysis and cluster analysis may be used for an assessment of spatial variation of precipitation periodicity, because their findings agree with the results of the spatial interpolation method.

References

Czarnecka, M. and *Nidzgorska-Lencewicz J.,* 2012*:* Wieloletnia zmienność opadów sezonowych w Polsce. (in Polish). *Woda Środ. Obsz. Wiej. 2012 (IV–VI), t. 12 z. 2 (38)*.45–60.(in Polish)

Banaszkiewicz B., Grabowska, K., and *Szwejkowski Z.,* 2004: Niedobory i nadmiary opadów na terenie województwa warmińsko-mazurskiego w latach 2000-2002.. *Acta Agrophysica, 3,* 5–11. (in Polish)

Banaszkiewicz B., Grabowska,K., and *Szwejkowski, Z.,* 2008: Characterisation of variability of atmospheric precipitation at selected stations of the Mazury Lake district in the years 1951-2000. *Acta Agrophysica, 12,* 19–27.

Boryczka, J. and *Stopa-Boryczka, M.,* 2004.Cykliczne wahania temperatury i opadów w Polsce w XIX-XXI wieku. (in Polish). *Acta Agrophysica, 3,* 21–33,

Chromow, S.P., 1977: Meteorologia i klimatologia. (in Polish). *PWN, Warszawa*.

Degirmendžić, J., Kożuchowski, K., and *Żmudzka, E.,* 2004*:* Changes of air temperature and precipitation in Poland in the period 1951–2000 and their relationship to atmospheric circulation. *Int. J. Climatol. 24,* 291–310. https://doi.org/10.1002/joc.1010

Dzieżyc, H., Chmura, K., and *Dmowski, Z. 2012:* Określenie wpływu warunków opadowych na plonowanie ziemniaka bardzo wczesnego i wczesnego w południowej Polsce. (in Polish). *Woda Środ. Obsz. Wiej. 2012 (IV–VI), t. 12 z. 2 (38),* 133–141.(in Polish)

Friederichs, P., 2010: Statistical downscaling of extreme precipitation events using extreme value theory. *Extremes 13,* 109–132. https://doi.org/10.1007/s10687-010-0107-5

Huang, D., Liu, Z., and *Wang, W.,* 2018*:* Evaluating the Impaction of Coal Mining on Ordovician Karst Water through Statistical Methods. *Water 10,* 1409. https://doi.org/10.3390/w10101409

Kożuchowski, K. and *Wibig J.,* 1988*:* Kontynentalizm pluwialny w Polsce: zróżniciwanie geograficzne i zmiany wieloletnie. (in Polish). *Acta Geographica Lodziensia 55,* 102–104.(in Polish)

Krzyśko, M., 2010:. Podstawy wielowymiarowego wnioskowania statystycznego. (in Polish). *Wyd. Nauk. UAM Poznań*.(in Polish)

Łupikasza, E., 2001: Zmienność wskaźnika nierównomierności opadów w Europie w XX wieku oraz jego związki ze zmiennością wskaźnika NAO. (in Polish). *Prace i Studia Geograficzne 29,* 243–251. (in Polish)

Marosz, M, Wójcik, R., Pilarski, M., and *Mietus,M.,* 2013*:* Extreme daily precipitation totals in Poland during summer: The role of regional atmospheric circulation. *Climate Res. 56,* 245–259. https://doi.org/10.3354/cr01155

Miler, A.T., 2018: Climate of vegetation season in Zielonka Forest and in Wielkopolski National Park in period 1848-2016. *Infr.Ecol.f Rural Area. 2,* 361–375.

Milligan, G.W. and *Cooper, M.,* 1985*:* An examination of procedures for determining the number of clusters in a data set. *Psychometrica 50,* 159–179, https://doi.org/10.1007/BF02294245

Mousavi, R.S., Ahmadizadeh, M., and *Marofi, S.A.,* 2018: Multi-GCM assessment of the climate change impact on the hydrology and hydropower potential of a semi-arid basin (A case study of the Dez Dam Basin, Iran).*Water 10,* 1458. https://doi.org/10.3390/w10101458

Nikulin, G., Kjellström, E., Hansson, U., Jones, C., Strandberg, G., and *Ullerstig, A.,* 2011*:* Evaluation and future projections of temperature, precipitation and wind extremes over Europe in an ensemble of regional climate simulations. *Tellus 63A*, 41–55. https://doi.org/10.1111/j.1600-0870.2010.00466.x

Olechowicz-Bobrowska, B., Skowera, B., Wojkowski, J., and *Ziernicka-Wojtaszek, A.,* 2005: Warunki opadowe na stacji agrometeorologicznej w Garlicy Murowanej. (in Polish). *Acta Agrophysica 6*, 455–463.(in Polish)

Paul, P. and *David, B.S.,* 2006*:* Analysis of the historical precipitation sums of Sulina Station by means of power spectra in relation to Sibiu Station and NAO and SOI indexes. *Geographia Technica 2*, 99−104.

Pauling, A., Steiner, D., Luterbacher, J., Casty, C., and *Wanner, H.,* 2005: Five hundred years of gridded high-resolution precipitation reconstructions over Europe and the connection to large-scale circulation. *Climate Dynamics 26*, 387−405. https://doi.org/10.1007/s00382-005-0090-8

Schulze, A., 1956: Eine Methode zur Efrassuung von jahresgangen mit praktischer Anwendung auf Lufttemperatur und Niedeschlagsmenge in Europa. *Petermanns Geographiche Mitteilungen 100*,1. (In German)

Skowera, B., Kopcińska, J., and *Kopeć, B.,* 2014: Changes in thermal and precipitation conditions in Poland in 1971–2010. *Annals of Warsaw University of Life Sciences – SGGW Land Reclamation 46*, 153–162. https://doi.org/10.2478/sggw-2014-0013

Twardosz, R., Niedźwiedź, T., and *Łupikasza, E.,* 2011: The influence of atmospheric circulation on the type of precipitation (Krakow, southern Poland). *Theor. Appl. Climatol. 104*, 233–250. https://doi.org/10.1007/s00704-010-0340-5

Tylkowski, J. and *Hojan, M.,* 2018*:*Threshold values of extreme hydrometeorological events on the Polish Baltic Coast. *Wather10*, 1337. https://doi.org/10.3390/w10101337

Walsh, R.P.D. and *Lawler, D.M.,* 1981*:* Rainfall seasonality: description, spatial patterns and change through time. *Weather 36*, 201–208. https://doi.org/10.1002/j.1477-8696.1981.tb05400.x

Wilgat, T., 1948: Okresowość opadów na kuli ziemskiej.. *Annales Universitatis Mariae Curie-Skłodowska, B, III, 9*, 333–386.(in Polish)

Woś, A., 1993*:*Klimat Polski. (in Polish). *PWN.Warszawa*.

Zawora, T. and *Ziernicka, A.,* 2003*:* Precipitation variability in time in Poland in the light of multi-annual mean values (1891–2000). *Acta Universitatis Wratislaviensis. Studia geograficzne., 75(2542)*, 123–128.

Ziernicka-Wojtaszek, A., Krużel, J., Borek, Ł., and *Ostrowski, K.,* 2015: Zmiany czasu trwania meteorologicznego okresu wegetacyjnego w Polsce w latach 1971–2000 oraz 1981–2010. (in Polish). *Inżynieria Ekologiczna 44*, 47–52. (in Polish) https://doi.org/10.12912/23920629/60024

Żarski, J. and *Dudek, S.,* 2000: Charakterystyka warunków termicznych i opadowych województwa kujawsko-pomorskiego w aspekcie potrzeb ochrony środowiska. (in Polish). *Zeszyty Naukowe WSHE we Włocławku, VI*, 85–98.(in Polish)

Żmudzka, E., 2009*:*Współczesne zmiany klimatu Polski. (in Polish). *Acta Agrophysica, 13*, 555–568. (in Polish)

INSTRUCTIONS TO AUTHORS OF *IDŐJÁRÁS*

The purpose of the journal is to publish papers in any field of meteorology and atmosphere related scientific areas. These may be

- research papers on new results of scientific investigations,
- critical review articles summarizing the current state of art of a certain topic,
- short contributions dealing with a particular question.

Some issues contain "News" and "Book review", therefore, such contributions are also welcome. The papers must be in American English and should be checked by a native speaker if necessary.

Authors are requested to send their manuscripts to

Editor-in Chief of IDŐJÁRÁS
P.O. Box 38, H-1525 Budapest, Hungary
E-mail: journal.idojaras@met.hu

including all illustrations. MS Word format is preferred in electronic submission. Papers will then be reviewed normally by two independent referees, who remain unidentified for the author(s). The Editor-in-Chief will inform the author(s) whether or not the paper is acceptable for publication, and what modifications, if any, are necessary.

Please, follow the order given below when typing manuscripts.

Title page should consist of the title, the name(s) of the author(s), their affiliation(s) including full postal and e-mail address(es). In case of more than one author, the corresponding author must be identified.

Abstract: should contain the purpose, the applied data and methods as well as the basic conclusion(s) of the paper.

Key-words: must be included (from 5 to 10) to help to classify the topic.

Text: has to be typed in single spacing on an A4 size paper using 14 pt Times New Roman font if possible. Use of S.I. units are expected, and the use of negative exponent is preferred to fractional sign. Mathematical formulae are expected to be as simple as possible and numbered in parentheses at the right margin.

All publications cited in the text should be presented in the *list of references*, arranged in alphabetical order. For an article: name(s) of author(s) in Italics, year, title of article, name of journal, volume, number (the latter two in Italics) and pages. E.g., *Nathan, K.K.,* 1986: A note on the relationship between photosynthetically active radiation and cloud amount. *Időjárás 90,* 10–13. For a book: name(s) of author(s), year, title of the book (all in Italics except the year), publisher and place of publication. E.g., *Junge, C.E.,* 1963: *Air Chemistry and Radioactivity.* Academic Press, New York and London. Reference in the text should contain the name(s) of the author(s) in Italics and year of publication. E.g., in the case of one author: *Miller* (1989); in the case of two authors: *Gamov* and *Cleveland* (1973); and if there are more than two authors: *Smith et al.* (1990). If the name of the author cannot be fitted into the text: *(Miller,* 1989); etc. When referring papers published in the same year by the same author, letters a, b, c, etc. should follow the year of publication. DOI numbers of references should be provided if applicable.

Tables should be marked by Arabic numbers and printed in separate sheets with their numbers and legends given below them. Avoid too lengthy or complicated tables, or tables duplicating results given in other form in the manuscript (e.g., graphs). *Figures* should also be marked with Arabic numbers and printed in black and white or color (under special arrangement) in separate sheets with their numbers and captions given below them. JPG, TIF, GIF, BMP or PNG formats should be used for electronic artwork submission.

More information for authors is available: journal.idojaras@met.hu

Published by the Hungarian Meteorological Service

Budapest, Hungary

INDEX 26 361

HU ISSN 0324-6329